Politecnico di Milano

Thesis submitted for the degree

Master of Science in Space Engineering

Multi-functional SElf-reconfigurable Robotic Arm (RAMSEs) and adjoined solar panel preliminary design for Lunar Entry Approach Platform For Research On Ground

---

Candidate:

Aloisia Russo

Supervisor: **Pierluigi Di Lizia**
Co-Supervisor: **David Barnhart**

2nd October 2020

Abstract

As space technologies are advancing the next challenging mission is to bring humans to Mars, paving the way for other deep-space destinations. Work on the Moon is a good test-bed for Mars as it can provide an opportunity to demonstrate new technologies that could help build self-sustaining outposts: the key success lies in international collaboration to achieve sustainability through the use of reusable architectures, and the capability to utilize Moon resources to create a permanent Lunar base. In this context, a reusable and completely autonomous lander capable of performing multiple tasks on the Moon's surface can help to accomplish the aforementioned objective. One of the projects exploring this new construct is from USC's Space Engineering Research Center (SERC) in its Lunar Entry and Approach Platform for Research on Ground (LEAPFROG) testbed. This is a hands-on project for students to simulate flight and ground activities for the lunar environment through tech generations as a repeatable flight system that uses a jet engine to simulate flight in lunar gravity on Earth. LEAPFROG Generation-II goal is to re-think the function of a lander so that it can perform multiple activities with the same mass after landing. A Master of Science research thesis in exploiting the capability of changing a single monolithic functioning lunar lander into a multi-functional platform is presented. This thesis will focus on the design of Multi-functional SElf-reconfigurable Robotic Arm (RAMSEs) with 7 degrees of freedom (DOF) as well as a unique adjoined solar panel design. RAMSEs will be capable of performing different soil activities after landing (i.e. to take samples, to drill, to dig, etc.), and before landing acting as a secondary structure on fuel tanks during the flight mode. A kirigami inspired solar panel design is also presented that is manipulated by the arm, which also serves two functions. The research aim is to find the most suitable configuration of RAMSEs as well as the most compact and functional design for the on-board solar panel. MATLAB Simulink® simulations will prove the RAMSEs capability to follow a prescribed trajectory which links tools allocated on-board points and their final point to perform the pre-selected activity. To deploy the dual function solar panel, an origami-based structure is used to extends six times its folded configuration to save space on-board while its usage is not required. This high-utility low-cost concept will be proven through a 3D-printed testbed described in the thesis.

Acknowledgment

I would express my thanks first of all to my advisor Prof. **Pierluigi Di Lizia** and my Co-Advisor **David Barnhart**. Prof. Di Lizia thanks so much for having supported me for all this months and for your belief in me. I've highly appreciated every single call and the support words you had for me, even if sometimes everything seemed too much difficult and stressful. Thanks for transitively showing me what does mean working with passion and spreading it to everyone. My best acknowledgment is for you. Prof. Barnhart I would thank you for giving me the best opportunity of my life: I've learned so much in these months and I had the chance to work in a totally different university environment, applying my knowledge on hands-on projects. I am so grateful you welcomed me in an amazing way and for making me feel part of a family; I am so grateful you trust me, my knowledge, my skills and you gave me so many responsibilities. I would like to say thanks to the SERC people: **David** (the Italian),**Arthur**, **Becca**, **Michael**, **Kirby**, **Lizvette**, **Everett**, **Eugene**, the **French guys** and so on. I would also thank who made me feeling like being at home and gave all the support even when everything was difficult: in particular to **Alejandro**. Thanks to **Basel**, **Hala**, **Stefan**, **Catherine**, **Lina**, **Sami** and **Fabian**. I had the best moment with you all in LA.

Ora inizio i ringraziamenti in italiano, per la gioia dei miei cari amici. Vorrei iniziare questa parte ringraziando chi c'è sempre stato in questi anni universitari e anche oltre. Vorrei iniziare dalle mie stelle: **Hannah** e **Nina**, grazie per esserci sempre state. Un ringraziamento speciale va ai miei amici e colleghi **Francesco** e **Jyoti**. Vorrei anche ringraziare i miei *amici di giù*: **Ylenia**, **Chiara**,**Donato**, **Giulio**, **Giusj**,**Marta**,**Lorenzo** e **Federico**. Questa avventura è stata bella soprattutto ai miei compagni di viaggio **Edoardo**, **Renato**, **Giulio**, **Giulia**, **Marzia**, **Federico**, **Antonio**, **Gabriele**, **Ruggero**, **Francesca**, **Fox** e **Marco**. A Milano mi sono sempre sentita a casa e supportata da **Giulia**, **Luna**, **Erika** mie compagne di tante avventure. Un altro ringraziamento alle donne dell'associazione Women In Aerospace, modello di lavoro e di vita: **Alice**, **Federica**, **Annamaria**, **Alessia**. Non per ultimo ringrazio la mia famiglia sebbene siano stati anni difficili per noi. Grazie mamma e grazie papà! Grazie anche a **Derbilia** e spero che tutto ciò possa essere per te una fonte di coraggio ed ispirazione. Vorrei dedicare questa tesi a **Nonna**, mio esempio di vita, che anche se non è qui a sentirmi parlare di questa esperienza, so che sarebbe stata orgogliosa e felice.

Acronyms

ABS Acrylonitrile Butadiene Styrene. 22, 23, 31

ACAT Advanced Concept Architecture Test. xiv, 3, 4, 9

ACS Attitude Control System. xiv, xv, 8, 10–12, 16, 17, 20, 23, 24, 27–29, 35

CNSA Chinese National Space Agency. 4

COTS Commercial Off-the-Shelf. 8, 9, 28, 29, 40, 57

CSM Command and Service Module. 2, 3

DDC Developable Double Corrugation. xvi, 53

DOFs Degrees Of Freedom. xv, 6, 17, 27, 29, 39, 40, 47, 48, 57

ECU Engine Control Unit. xiv, 9, 10, 18, 32, 36

EGT Exhaust Gas Temperature. 18

EPDP Electric Propulsion Diagnostic Package. 4

EPU Electric Power Unit. 59, 63

ESA European Space Agency. 4, 5

GNC Guidance Navigation and Control System. 12, 20

IMU Inertial Measurement Unit. 12, 20, 36

ISRO Indian Space Research Organization. 4, 5

KKV Kinetic Kill Vehicles. 8, 9

LEAPFROG Lunar Entry Approach Platform For Research On Ground. 5, 6, 8, 9, 14, 16, 27, 32, 36, 45, 72

LEO Low Earth Orbit. 2

LLRV Lunar Landing Training Vehicle. 8–10

LLV Lunar Lander Vehicle. 4, 5

LM Lunar Module. xiv, 2, 3

MIP Moon Impactor Probe. xiv, 4, 5

NASA National Aeronautics and Space Administration. xiv, 1–3, 5

NPT National Pipe Thread. 19

OBAN On-Board Autonomous Navigation. 4

OSP Origami Solar Panel. xv–xviii, 27, 32, 39, 47–50, 56–60, 62–70, 72, 81

PID Proportional, Integral and Derivate. 12

PVC Polyvinyl Chloride. 14, 31

R-CFR Configuration Requirements. 38

R-DSR Design Requirements. 10, 14, 17, 28, 29, 33, 38, 57

R-ENR Environmental Requirements. 38

R-FNR Functional Requirements. 10, 17, 29, 57

R-HLR High-Level Requirements. 9, 28, 37, 57

R-INR Interface Requirements. 23, 24, 37, 38

R-OPR Operational Requirements. 17, 29

R-PAR Product Assurance Requirements. 39

R-PHR Physical Requirements. 38, 42

RAMSEs Multi-functional SElf-reconfigurable Robotic Arm. xv–xvii, 6, 27, 31, 32, 37–40, 42–51, 57, 59, 72, 82

RF Radio Frequency. 6

SERC Space Engineering Research Center. iii, 5, 6, 8, 29, 31, 33, 56, 57, 72

SINGO Single-End-Operative and Gender-less Connector. 42

SMART Small Missions for Advanced Research in Technology. 4

TTC Telemetry and Telecommand. 4

TVC Thrust Vector Control. xv, 27, 32–34

USC University of Southern California. 5, 28, 38, 72

Glossary

Tassel	Single element that composes the Origami Solar Panel
Pitch circle	This is a right section of an imaginary cylinder (pitch cylinder), that the toothed gear may be considered for replacement
Pitch Diameter	Diameter of the gear
Pitch Point	The point of tangency of the pitch circles of a pair of mating gear wheels
Common tangent	Tangent to the pitch circles at the pitch point
Addendum Circle	Circle that passes through all the tooth ends
Addendum	Radial distance between pitch circle and addendum circles
Dedendum [Root] Circle	Bounds the space between the teeth
Dedendum	Radial distance between the pitch circle and Dedendum circle
Circular Pitch	Sum of tooth thickness and tooth space, measured along a pitch circle
Diametral Pitch	Number of teeth of a gear per unit pitch diameter
Module	Inverse of diametral pitch
Pressure Line	Path of contact being normal to the involute profiles is the pressure line
Pressure Angle	Angle made by the pressure line with the horizontal

Main Hinge	Third hinge-gear which connects the driven tassel to the slave one

Nomenclature

α	First folding angle	$[deg]$
β	Second folding angle	$[deg]$
γ	Tassel geometric angle	$[deg]$
λ	Gear slenderness	[mm]
σ_{amm}	Material maximum admissible flexural strenght	[MPa]
τ	Transmission ratio	[]
θ	Pressure angle	[°]
a	Resistant torque arm	[mm]
b	Tooth width	[mm]
C_1	Stepper motor provided torque	[Nmm]
C_r	Slave tassels resultant weight torque	[Nmm]
d_{a1}	First gear addendum diameter	[mm]
d_{a2}	Second gear addendum diameter	[mm]
d_{a3}	Third gear addendum diameter	[mm]
d_{b1}	First gear clearance diameter	[mm]
d_{b2}	Second gear clearance diameter	[mm]
d_{b3}	Third gear clearance diameter	[mm]
d_{f1}	First gear dendum diameter	[mm]
d_{f2}	Second gear dendum diameter	[mm]
d_{f3}	Third gear dendum diameter	[mm]
d_{p1}	First gear primitive diameter	[mm]

d_{p2}	Second gear primitive diameter	[mm]
d_{p3}	Third gear primitive diameter	[mm]
F	Force acting among the gear pressure line	[N]
h_2	Littler tassel height	[mm]
m_n	Normal Modulus	[]
r_{tree}	Stepper motor tree radius	[mm]
T	Stepper motor torque	[Nmm]
y_{lewis}	Tabulated value	[]
z_1	First gear number of teeth	[]
z_2	Second gear number of teeth	[]
z_3	Third gear number of teeth	[]

"The more I want to get something done, the less I call it work".

Contents

List of Figures

List of Tables

Chapter 1

Introduction

From ancient times, the Moon has always attracted humans' attention and they wondered what it was or if it were possible to go there. From the early 17^{th}century, Moon geology has been studied, and for the first time, space travels have been researched objective for scientists like Galileo and Isaac Newton. During the following centuries, maths and new technologies made space travel achievable thanks to rocket science: for the first time in the 1950s, a Moon lander has been envisioned by Von Braun. In 1959 the Luna 2 was the first one spacecraft to land on the Moon surface: it was a spherical spacecraft with different linear antennae, scintillation and Geiger counters, a magnetometer and micrometeorite detectors without any propulsion system. This mission confirmed the absence of an appreciable magnetic field and did not find an evidence o about the radiation belts [1].

In the late 1960s, humankind has done a leap landing on the Moon for the first time with NASA's Apollo program enabling past centuries' expectations. From 1966 to 1968 the Surveyor Program planned the launch of seven different unmanned landers on the Moon with the objectives of accomplishing the technology to perform a soft-landing, likewise the characterization of the landing site for the future Apollo Program, of demonstrating the telecommunications capabilities and Deep Space Network to maintain spacecraft communications during its flight and after the soft-landing ,and to carry out different operations on the lunar surface [9]. The Surveyor 1 structure included a thin-walled aluminum tripod with interconnecting braces that provided mounting surfaces for the power, communications, propulsion, flight control and payload systems. The central mast was extended above the apex of the tripod; below the structure three hinged landing legs were fixed, which held crushable, honeycomb aluminum blocks, shock absorbers and the the deployment locking mechanism and ended in footpads with crushable bottoms [10].

In 1966 the mission Luna 13 successfully landed in Oceanus Procellarum: the main structure was identical to the Luna 9 mission. It was composed by a spherical hermetically sealed container, which held the radio system and scientific apparatus: four antennas were mounted on the outside of the compartment, as well as the airbag amortization system for the landing phase. The compartment was above a flight stage which held the retrorocket, four outrigger vernier rockets, a toroidal aluminum alloy fuel tank,

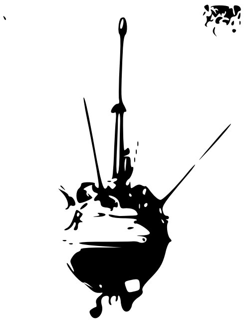

Figure 1.1: Luna 2 lander. Credits: NASA [1]

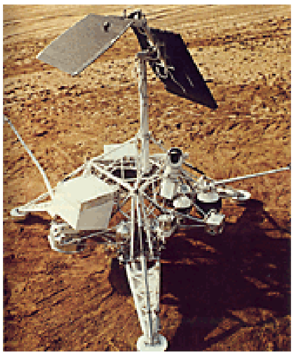

Figure 1.2: Surveyor 1 lander [2]

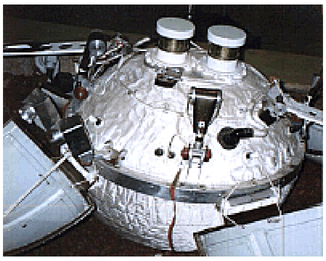

Figure 1.3: Luna 13 lander [3]

a spherical oxidizer tank, fuel pumping system, the nitrogen tank for airbag inflation, and guidance and landing sensor equipment. This included gyroscopes, electro-optical apparatus, the soft-landing radar system, and small orientation engines, a guidance radar and the three nitrogen jets and gas bottles of the attitude control system for the cruise stage, designed to be jettisoned once the descent was underway [11].

Apollo Program started in 1961, with the first man on the Moon achievement thanks to the Apollo 11 mission in 1969: it ended in 1975 with Apollo 17. This Program was essential due to the big list of technological milestones in the science, avionics, computer science and telecommunications [12]. Before this program, human space flight was limited on the Low Earth Orbit (LEO) only. The Apollo Lunar Module (LM) was the first one crewed vehicle to land on the Moon. The ascent and descent stages of the LM operated as one until staging, when the ascent stage functioned as a single spacecraft for rendezvous and docking with the Command and Service Module (CSM) [13]. The descent stage comprised the lower part of the spacecraft and was an octagonal prism. Four landing legs with round footpads were mounted on the sides and held the bottom of the stage: one of them had a small astronaut egress platform and ladder [14]. A conical descent engine skirt protruded from the bottom of the stage. The descent stage contained the landing rocket, two tanks of fuel, two tanks of oxidizer, water, oxygen and helium tanks and storage space for the lunar equipment and experiments, and in the case of Apollo 15, 16, and 17, the lunar rover. The descent engine was a deep-throttling ablative rocket mounted on a gimbal ring in the center of the descent stage, while the ascent engine was a fixed, constant-thrust rocket. [15]. The descent stage served as a platform for launching the ascent stage and was left behind on the Moon [16]. The ascent stage was an irregularly shaped unit mounted on top of the descent stage: it housed the astronauts in a pressurized crew compartment which functioned as the base of operations. None seats were in the LM. There was an ingress-egress hatch in one side and a docking hatch for connecting to the CSM on top. Here a parabolic rendezvous radar antenna was mounted, likewise a steerable parabolic S-band antenna, and 2 in-flight VHF antennas [17]. Two triangular windows were above and to either side of the egress hatch and four thrust chamber assemblies

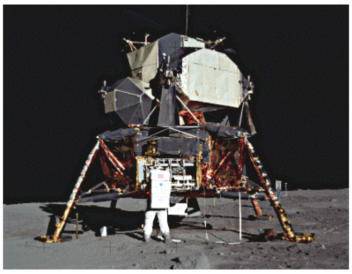

Figure 1.4: Apollo LM. Credits: NASA

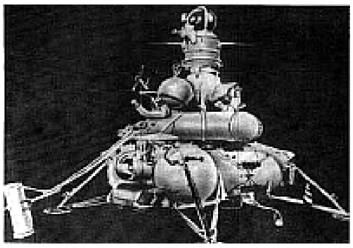

Figure 1.5: Luna 16 lander

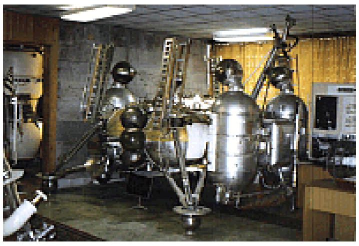

Figure 1.6: Luna 17 lander

were mounted around the sides [18]. At the base of the assembly there was the ascent engine. A control console was mounted in the front of the crew compartment and two more on the side walls. The ascent stage was launched from the Moon at the end of lunar surface operations and returned the astronauts to the CSM. Maneuvering was achieved via the reaction control system, which consisted of the four thrust modules. Telemetry, TV, voice, and range communications with Earth were all via the S-band antenna. VHF was used for communications between the astronauts and the LM. An environmental control system recycled oxygen and maintained temperature in the electronics and cabin. The power was provided by silver-zinc batteries [16].

In 1970 the first fully robotic sample return was accomplished by the Luna 16 unmanned craft which drilled out a sample core and returned it to the Earth [19]: it consisted of two stages attached together; an ascent one mounted on the top of the descent stage. It was a cylindrical body with four legs, fuel tanks, a radar altimeter and a dual descent engine complex: it contained also a television camera, radiation and temperature monitors, telecommunications equipment and an extensible arm with a drill at its end for collecting samples. The ascent stage was a cylinder with a spherical top and carried an hermetically sealed soil sample container inside a re-entry capsule [20]. Indeed, Luna 17 craft contained the first fully autonomous rover, the Lunokhod 1, landed on the Moon: it was deployed by two ramps and it was composed by a tub-like compartment with a convex lid on eight powered wheels; it was also equipped with a cone-shaped antenna, a high directional helical antenna, four television cameras and extendable devices to impact the lunar soil. The rover was powered by a solar cell array. It operated for eleven days continuously [21].

In the 1990s, the spacecraft miniaturization came forward. An example is the Clementine spacecraft (an octagonal prism 1.88 m high and 1.14 m across with two solar panels protruding on opposite sides parallel to its axis) which did multi-spectral images of the Moon surface thanks to its seven payloads: a UV/Visible Camera, a Near Infrared Camera, a Long Wavelength Infrared Camera, a High Resolution Camera, two Star Tracker Cameras, a Laser Altimeter, and a Charged Particle Telescope [22].

In those years the downsizing and reducing mission both costs and the design time became a trend and several new proposals were putted forward. An example is the Advanced Concept Architecture Test (ACAT): a micro-lander which carries a rover as a payload with the main objectives of demonstrating lunar terminal gate manoeuvres

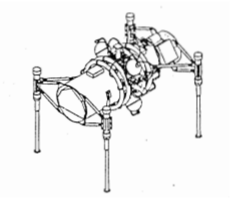

Figure 1.7: ACAT Vehicle [4]

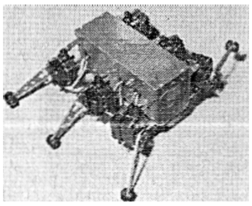

Figure 1.8: ACAT rover [4]

with a micro-spacecraft, of deploying a payload, of showing micro-miniature robotics technology combined with a military derived spacecraft hardware. The overall mass with the payload was less than $20kg$ [4].

In the early 21^{th} Century other nations started pursuing Moon missions such the orbiter Small Missions for Advanced Research in Technology (SMART-1) from ESA, designed to test spacecraft technologies for future missions like the solar-powered ion drive as well as the deep-space telecommunications system and the instrument payload. The science instruments include a pan-chromatic camera (AMIE) for lunar imaging, Langmuir probes mounted on booms (SPEDE) to measure the plasma environment, radio science experiments (RSIS), a miniaturized visible/near-infrared spectrometer (SIR) for lunar crustal studies, a miniature X-ray spectrometer for astronomy and lunar chemistry (D-CIXS), and an X-ray spectrometer to calibrate D-CIXS and to study the Sun (XSM). The Electric Propulsion Diagnostic package (EPDP) is a multi-sensor suite designed specifically to monitor the ion propulsion system. Finally an experimental telecommunication and tracking system, the Ka/X-band Telemetry and Telecommand (TTC) Experiment (KaTE) is included in the payload for technology assessment. The AMIE camera will also be used to support a test of an image-based On-Board Autonomous Navigation (OBAN) system. OBAN is designed to minimize the amount of ground intervention required for the mission [23].

In 2008 the ISRO launched the Moon Impactor Probe (MIP), its first lunar probe released by Chandrayaan-1 spacecraft. Thanks this mission, India was the fourth nation to reach the lunar surface, with the main objectives of proving the technologies for reaching a specified location on the Moon, qualifying technologies required for any future soft landing missions, and of exploring from close range just prior to the impact. MIP payloads were a radar altimeter, a video imaging system and a mass spectrometer. The probe used aluminium sandwich structure onto which the payloads were mounted. A solid propellant de-orbit mortar nudged the craft into lunar orbit, while spin thrusters stabilized the orientation enabling imaging system to capture the descent profile [24].

In 2013 Chang'e 3 mission from CNSA a Lunar Lander Vehicle (LLV) was landed on the Moon Surface after the Luna 14 mission from 1976. It consisted of a soft lander, which carried a four instruments payload and a rover (Yutu). It was a six-wheeled vehicle powered by solar cells. Mounted on top of the LLV, it was lowered on a ramp onto the lunar surface after landing: its instruments include a stereo camera, ground penetrating radar, visible/near-infrared imaging spectrometer, and alpha particle x-ray spectrometer. It also had navigation and hazard avoidance cameras and may have a

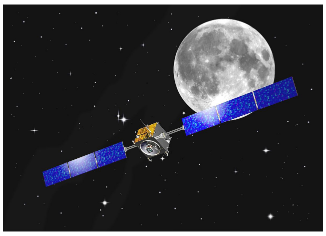

Figure 1.9: SMART-1 Credits: ASI [5]

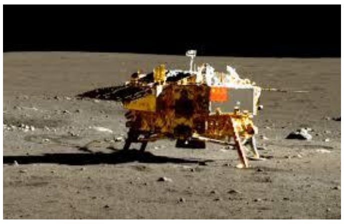

Figure 1.10: Chang'e 3 lander

Figure 1.11: MIP lander

lunar soil probe. Data were transmitted back to Earth in real time. Moreover, the LLV was equipped with three panoramic cameras, a topography camera, an extreme ultraviolet camera, and an ultraviolet telescope [25].

In 2019 Chandrayaan 2 mission from ISRO had as main objective to demonstrate the ability to soft-land on the Moon surface and operate a robotic rover, but contacts were lost during the descent phase. The lander (Vikram) was a truncated pyramid build around a cylindrical propellant tank and it can communicate directly to the Indian Deep Space Network and it carried a camera and four different payloads. The rover (Pragyan) is a six-wheeled vehicle with a rocker bogie design based on the NASA Sojourner Rover and it communicated directly to Vikram [26].

The next challenging mission is bringing man to Mars and other deep-space destinations: NASA's Artemis [27] lunar exploration program will send the first woman and the next men to the Moon surface, while ESA's PROSPECT project [28] is focusing attention in potential resources extraction to support future exploration missions.

Work on the Moon can be considered a test-bed for Mars as it can provide an opportunity to demonstrate new technologies that could help build self-sustaining outposts off Earth: the key of the success to this challenge lies in international collaboration to explore faster, achievable sustainability through use of reusable architectures, and the capability to manage Moon resources to create a permanent Lunar base.

In this context a reusable and completely autonomous lander capable of performing multiple tasks on the Moon's surface can help to accomplish the aforementioned objectives. One of the projects in which the Space Engineering Re-search Center (SERC) of University of Southern California (USC) is involved is the Lunar Entry and Approach Platform for Research on Ground (LEAPFROG). This is a hands-on project for student to simulate flight and ground activities which will occur in the lunar environment with further generations, and is a repeatable flight system that uses a jet air breathing engine to simulate flight in lunar gravity. LEAPFROG consists into a three prototypes project: they were developed in more than a decade starting from the Generation-0 in 2006 and ending with the Generation-II in 2020.

Although LEAPFROG Generation-1 has been developed with many improvements with respect to the previous generation, it followed a monolithic or single function task of flight, albeit with additional payload carrying capacity to test out new components.

Since the goal of going to the Moon is getting more and more attention, many companies are trying to build their own lander with different focused tasks (e.g Blue

Origin [29], Boeing [30],Indian Space Research Organisation [31], Orbit Beyond and Astrobotic [32]). The projects proposed from mentioned companies are capable to land in selected zones on the Moon surface, and execute different types of exploration or research functions (such as releasing littler rovers): none is designed to perform multiple operations with the same lander. The lander is "monolithic" in function, the mass sent up only executes one task.

LEAPFROG Generation-II has the aim to re-think the function of a lander so that it can perform multiple activities with the same structure: as an example it could be capable to transform into a rover to save propellant and enable a much larger area of exploration from the landing zone, or be able to unfold or transform into a very large reflector for RF communications.

Thesis research objectives

The main research aim is specifically to look at changing a single monolithic functioning lunar lander into a multi-functional platform that uses various techniques and new technologies to extend the use of the mass embedded in the makeup of the landing platform. As an example, envisioning that a lander will be permanent it must be capable to self-charge its on-board batteries: a suitable solar panel deployed during the non-flight condition of the lander could be useful. To save space and re-use some of its mass the its possible to design the platform to "hide" the solar panel until its required. That being said, the use of origami structures that have the capability to be extendable up to ten times the folded configuration [33] could achieve this aim. NASA has been working on origami structures for space application during last years [34, 35, 36], exploring this type of concept also for solar panels [37].

One thesis objective is to evaluate the creation of a single element of an origami structure to prove this type of methodology can extend mass from one function to another. This thesis will show how its design and a test-bed realization has been performed at SERC.

A second research objective is to design a multi-functional robotic arm which is capable to implement different functions from flight to ground (i.e. to collect samples, to drill, to dig). As an example, a robotic arm is typically held down with launch and flight locks, and its sole purpose is maneuverability upon release. In this case, it has been investigated on how a robotic arm during flight serves as the "secondary structure" that holds one element of a fuel tank on a lander, and then upon landing, the arm "de-attaches" from the fuel tank, through jointed at its based becomes a maneuverable element. To prove its utility a preliminary design of a 7 degrees-of-freedom (DOFs) Multi-functional SElf-reconfigurable Robotic Arm (RAMSEs) arm extendable up to 14 DOFs on the LEAPFROG platform would be performed. Therefore, the robotic arm would be capable to choose a suitable tool for any activity programmed a priori and it will also serve as the motive force to unfold the origami based solar panel, further extending the multi-functionality of our new lander design.

This thesis is divided into three chapters which will explain the LEAPFROG project concept in Chapter 2. The RAMSEs preliminary design is explained in Chapter 3, while the origami solar panel design and its 3D-printed mechanical test-bed will be described in Chapter 4. Then a conclusive chapter will summarize the research done and will propose future developments.

Chapter 2

LEAPFROG Project

The LEAPFROG project from SERC is conceived as a solution to the challenges of the development and testing of lunar landing technologies. Its main requirement was of being a reusable landing vehicle able to simulate lunar gravity on Earth kerosene engine. This crew-less vehicle was inspired by the Apollo-era Lunar Landing Research Vehicle and the Kinetic Kill Vehicles (KKV) to provide a low cost test-bed for technology developments. LEAPFROG in 2006 was envisioned as a semester paper-to-flight and hands-on project to create a Generation-0 proof of concept vehicle using Commercial Off-the-Shelf (COTS) components, take off and land safely and to maintain the lowest possible project costs [38].

During the flight test of this prototype, many problems occurred and the configuration wasn't adequately optimized (i.e. it wasn't able to hover stably after its take off). The project was dormant from 2008, after obtaining encouraging results, until 2018 with the establishment of the Generation-1. Its mean high-level requirement was to have a cheaper and private way to send sensors or instrumentation from civilians or governmental companies concerning this decade's technologies mentioned in the Introduction [1]. The configuration was lighter compared to the previous generation and more reliable landing gears were added to resist at a more substantial impact. Besides, a more stable Attitude Control System (ACS) was designed to hover more than 180 seconds [39].

Although Generation-1 performed all tests successfully, its configuration was intended only for compact, tiny payloads, and it had the only capabilities of taking off, hovering and landing with a monolithic structure. In the framework of extending the activities, which a lander could do on the Moon surface, from September 2019 to nowadays, the Generation-II has been designed and built by the SERC LEAPFROG team.

2.1 Generation-0

The Generation-0 is inspired by the Lunar Landing Research Vehicle LLRV, which was created to study and analyze the piloting techniques for the descent and landing of

ID	Project Requirements
R-HLR-01	The project shall be completed in one semester
R-HLR-02	The project shall be completely built by students by using COTS

Table 2.1: Generation-0 Project Requirements

the Apollo Lunar Module (Figure 2.1). The LLRV used a vertically gimbaled General Electric CF-700-2V turbofan engine for vertical thrust, two hydrogen peroxide lift rockets to handle the rate of descent and horizontal movement, and sixteen smaller hydrogen peroxide rockets for attitude control [40].

Figure 2.1: The NASA LLRV during a 1964 test flight (NASA photo ECN 506).

Another inspiration is the KKV a small, lightweight, autonomous vehicle designed to track a ballistic missile in flight. Equipped with an inertial guidance and navigation system, onboard propulsion and a sensing systems. The Advanced Concept Architecture Test (ACAT) was a modified version of the KKV and it served as test-bed for novel landing instrumentation [41].

2.1.1 Requirements

Project and System Requirements are listed in Tables 2.1 and 2.2. The R-HLR-01 is justified by the fact that LEAPFROG has to be a hands-on project designed and built by students, who have to face all its phases. Indeed, the R-HLR-02 states the absence of any contractors during the project development.

2.1.2 Subsystems

Jet Propulsion System

The propulsion system to take-off, hover, and controlled descent is ensured by a kerosene powered jet engine, the JetCat P-200 [42], which is fixed vertically at the center of mass of the vehicle. It is used only to provide an opposing force to the gravity one with any induced pitch and roll. Moreover, using a jet engine instead of a propeller, there is a considerable reduction of the unwanted yaw caused by the rotation of blades. JetCat engines are characterized by an already configured Engine Control Unit (ECU), which helps in reducing the project development time. JetCat P-200 runs

ID	Systems Requirements
R-DSR-01	The vehicle shall hover, translate laterally and maintain rotational stability
R-DSR-02	The minimum flight time shall be three minutes
R-DSR-03	The vehicle shall fly autonomously
R-DSR-04	The vehicle shall receive startup and flight termination commands from the ground station
R-FNR-01	The onboard power system shall support six minutes of operation

Table 2.2: Generation-0 Systems Requirements

with a propane and butane mixture and comes with the propane tank, which has to be integrated on the vehicle. The ECU controls the main engine thanks to an RPM feedback and the exhaust gas temperature, as shown in the Figure 2.2 . The ECU receives a command in the form of an RPM value, converts it into a voltage signal and sends a proportional command to the fuel pump. The JetCat P-200 provides a maximum thrust of 200N at the sea level and is composed of a compressor stage, a combustion chamber and a turbine. The thrust provided by the engine was the limiting factor for the Generation-0 maximum weight. Therefore, this vehicle only had a thrust to weight ratio of 1.03. Figure 2.3 shows the jet propulsion system configuration.

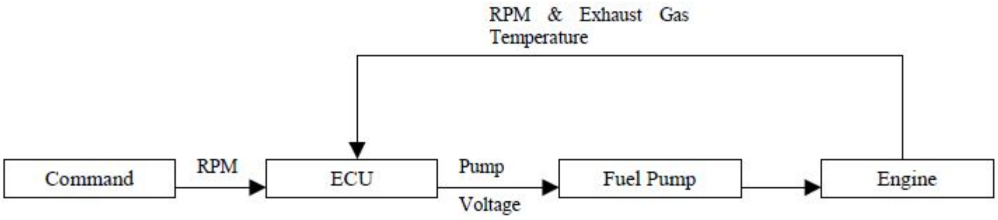

Figure 2.2: The internal control loop of the JetCat P200 ECU

Attitude Control System

The LLRV one directly inspired the ACS. Although the nitrogen is the lighter cold gas for this application, the chosen one is air thanks to its university laboratories' readiness and for air tanks costs. Two paintball tanks were selected because they can hold a pressure up to 4500PSI and are the most commonly available carbon fiber tanks, with a volume of 1,88 L each considering the R-DSR-02. There is a regulator integrated, which lowers down the pressure until 900PSI and two high-pressure aluminum tubes, including On/Off valves, which permit the tanks filling. Moreover, the two lines are

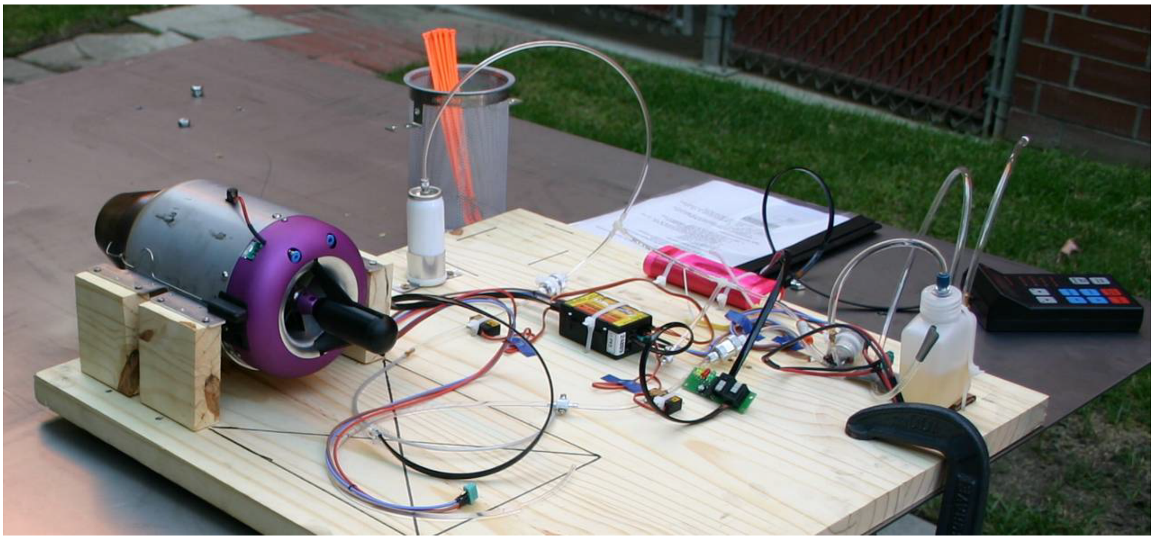

Figure 2.3: The JetCat P200 jet engine and support equipment: 1) Gas Inlet, 2) Fuel Inlet, 3) Glow Plug, 4) Thermocouple, 5) Data Port, 6) Power Port, 7) Starter Motor, 8) Propane/Butane Starter Tank, 9) BVM Ultimate Air Trap, 10) Ground Support Unit, 11) Fuel Pump, 12) NiCad Jet Battery, and 13) Engine Control Unit.

merged into a single one where a filter to avoid impurities is provided. A pressure transducer permits to monitor the lines pressure, and a bleed valve, set in parallel, is used to low down the pressure. After these components, the line splits until the thrusters, which works in a fully opened or fully closed position thanks to 12 solenoid valves. The schematic of the ACS system is shown in Figure 2.4.

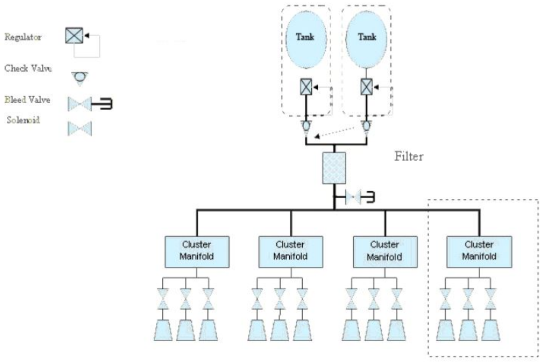

Figure 2.4: ACS system architecture.

The thrust of each thruster is $5.12N$ ($1.15lb$). The Generation-0 ACS has some drawbacks: first, with only four solenoid valves pointing vertically to the ground, the ACS acts on the vehicle pitch and roll but not on the yaw, causing an instability. Besides, all the valves are connected to the only one source, causing pressure drops when two thrusters are fired simultaneously, resulting in less efficient feedback of the position and a more complex flight code. As shown in Figure 2.5, the final configuration gives trouble in fitting exactly the center of gravity in the platform's center. Moreover, a delay appears on each thrust because of the drawbacks mentioned above.

Avionics

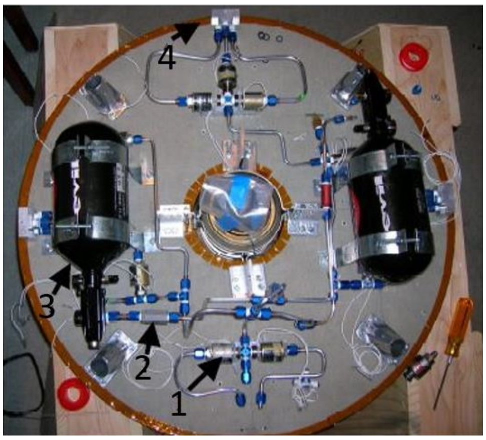

Figure 2.5: ACS components on underside of vehicle: 1) solenoid valve, 2) check valve, 3) nitrogen tank, and 4) thruster pod.

The avionics system gathers all the onboard sensors data, computes the current attitude and executes the pre-set flight profile by activating the appropriate thrusters during the set time. The system is composed of an Inertial Measurement Unit (IMU), a three-axis accelerometer with a dynamic range of $\pm\ 3g$, with an output of 300 mV/g. A small acceleration range increases the sensor resolution. The accelerometer is mounted with the positive vertical axis facing upwards, resulting in a default value of -1 g at the sea level. Finally, three single-axis gyroscopes are used to measure angular velocity, with a maximum capability of ± 150 $\deg/s$.

Guidance Navigation and Control System

The Guidance Navigation and Control (GNC) system makes the vehicle able to obey instructions from the flight code and to follow the appropriate maneuvers. The lander shall ensure angular stability within one degree and transitional accuracy within 0,25 meters. Even if the equations of motion are non-linear and time-dependent, thanks to the changing fuel mass in time and atmosphere's presence. However, it has been decided to linearize the system of equations and it has been modeled first on Simulink©, then on MATLAB to simulate the lander's behavior during a flight. A Proportional, Integral and Derivate (PID) controller is implemented to ensure precision, readiness and resilience (i.e., to regulate random perturbations due to atmospheric phenomena such as wind or pressure disturbances). Moreover, thrusters are only acting fully opened or fully closed; therefore, a threshold is set to trigger the thrusters in order to fire only when the correction is needed, minimizing the quantity of gas used.

Power Control System

The power budget considers a longer period than the required flight time to avoid a loss of the vehicle performances caused by a lack of electrical power. The ACS is the subsystem that requires the most powerful electrical supply for the solenoid valves. The engine also requires an electrical battery, and finally, the avionics have the smallest electrical power requirement. All the power is supplied through rechargeable batteries: a 24V Lithium Polymer battery for the ACS and a non-rechargeable 9V battery except for the camera. The Generation-0 power budget is showed in Figure 2.6

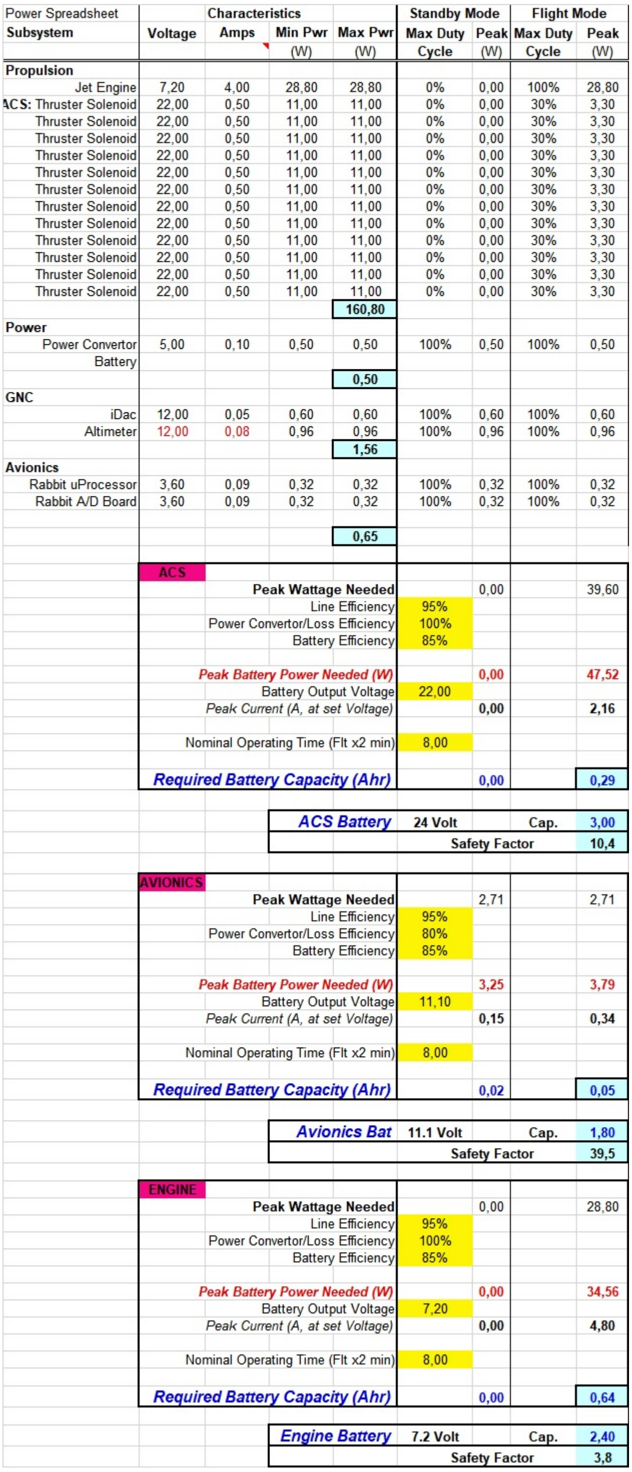

Power Spreadsheet		Characteristics			Standby Mode		Flight Mode	
Subsystem	**Voltage**	**Amps**	**Min Pwr (W)**	**Max Pwr (W)**	**Max Duty Cycle**	**Peak (W)**	**Max Duty Cycle**	**Peak (W)**
Propulsion								
Jet Engine	7,20	4,00	28,80	28,80	0%	0,00	100%	28,80
ACS: Thruster Solenoid	22,00	0,50	11,00	11,00	0%	0,00	30%	3,30
Thruster Solenoid	22,00	0,50	11,00	11,00	0%	0,00	30%	3,30
Thruster Solenoid	22,00	0,50	11,00	11,00	0%	0,00	30%	3,30
Thruster Solenoid	22,00	0,50	11,00	11,00	0%	0,00	30%	3,30
Thruster Solenoid	22,00	0,50	11,00	11,00	0%	0,00	30%	3,30
Thruster Solenoid	22,00	0,50	11,00	11,00	0%	0,00	30%	3,30
Thruster Solenoid	22,00	0,50	11,00	11,00	0%	0,00	30%	3,30
Thruster Solenoid	22,00	0,50	11,00	11,00	0%	0,00	30%	3,30
Thruster Solenoid	22,00	0,50	11,00	11,00	0%	0,00	30%	3,30
Thruster Solenoid	22,00	0,50	11,00	11,00	0%	0,00	30%	3,30
Thruster Solenoid	22,00	0,50	11,00	11,00	0%	0,00	30%	3,30
Thruster Solenoid	22,00	0,50	11,00	11,00	0%	0,00	30%	3,30
				160,80				
Power								
Power Convertor	5,00	0,10	0,50	0,50	100%	0,50	100%	0,50
Battery								
				0,50				
GNC								
iDac	12,00	0,05	0,60	0,60	100%	0,60	100%	0,60
Altimeter	12,00	0,08	0,96	0,96	100%	0,96	100%	0,96
				1,56				
Avionics								
Rabbit uProcessor	3,60	0,09	0,32	0,32	100%	0,32	100%	0,32
Rabbit A/D Board	3,60	0,09	0,32	0,32	100%	0,32	100%	0,32
				0,65				
	ACS							
				Peak Wattage Needed		0,00		39,60
				Line Efficiency	95%			
				Power Convertor/Loss Efficiency	100%			
				Battery Efficiency	85%			
				Peak Battery Power Needed (W)		**0,00**		**47,52**
				Battery Output Voltage	22,00			
				Peak Current (A, at set Voltage)		**0,00**		**2,16**
				Nominal Operating Time (Flt x2 min)	8,00			
				Required Battery Capacity (Ahr)		**0,00**		**0,29**
				ACS Battery	**24 Volt**		**Cap.**	**3,00**
						Safety Factor		**10,4**
	AVIONICS							
				Peak Wattage Needed		2,71		2,71
				Line Efficiency	95%			
				Power Convertor/Loss Efficiency	80%			
				Battery Efficiency	85%			
				Peak Battery Power Needed (W)		**3,25**		**3,79**
				Battery Output Voltage	11,10			
				Peak Current (A, at set Voltage)		**0,15**		**0,34**
				Nominal Operating Time (Flt x2 min)	8,00			
				Required Battery Capacity (Ahr)		**0,02**		**0,05**
				Avionics Bat	**11.1 Volt**		**Cap.**	**1,80**
						Safety Factor		**39,5**
	ENGINE							
				Peak Wattage Needed		0,00		28,80
				Line Efficiency	95%			
				Power Convertor/Loss Efficiency	100%			
				Battery Efficiency	85%			
				Peak Battery Power Needed (W)		**0,00**		**34,56**
				Battery Output Voltage	7,20			
				Peak Current (A, at set Voltage)		**0,00**		**4,80**
				Nominal Operating Time (Flt x2 min)	8,00			
				Required Battery Capacity (Ahr)		**0,00**		**0,64**
				Engine Battery	**7.2 Volt**		**Cap.**	**2,40**
						Safety Factor		**3,8**

Figure 2.6: Generation-0 Power Budget

Structure

The Generation-0 vehicle structure is composed of a foam core platform hardened with epoxy and fiberglass, on which four carbon fiber tubes are attached. The platform foam is made of Divinycell H-100 polyvinyl chloride (PVC) with one inch (2.54 cm) of width. Subsequently, it is laminated with fiberglass and epoxy to augment the strength and to make it more shock-resistant to both sides. This composite material is chosen for its high strength to weight ratio, compared to other raw materials such as wood or aluminum or even compared to other core materials such as balsa wood. To have the most durable and resistant material possible, the fiberglass is added to the foam core under a vacuum. A sit permits to get rid of all the air trapped inside the epoxy and hold the fiberglass tight against the board during the resin drying process. Then, the circular shape is obtained with a bandsaw.

The legs are made of 30,5cm (1ft) carbon fiber tubes, characterized by a high strength to weight ratio. They are attached to the foam core and the landing pads on the other side with fifty-five-degree. The landing pads include a shock-absorbing part to make the vehicle capable of resisting a one-meter free-fall: this is made of a crushable paper bowl zip-tied to an aluminum plate bolted at the end of the bottom flange. This is a not reusable solution but is cheap and the four landing pads can be replaced in a small amount of time. Fifty-five-degree flanges are attached to the carbon leg with a bolt and the epoxy. The test results show the vehicle could withstand at a fall up to 0.71 meters (28 inches) for a structure of around 3.75kg (7.88lbs). There are some drawbacks to this solution. First, the landing pads are not reusable: even if they are easy and cheap to replace, human manipulation is needed after each landing and this means the vehicle could only land where there is someone to make the replacement. Therefore the R-DSR-03 is not fully satisfied. Moreover, the aluminum flanges could be replaced with a lighter material and the epoxy used to fix them, add mass to the whole vehicle.

Communications and Payload

For sending commands to the vehicle from the ground station, a low-gain omni-directional collinear antenna is installed. The antenna operated at the standard S-band frequency of 2.4 GHz with a right-handed circular polarization. A low-gain omni-directional WiFi whip antenna is also present, which operates at 2.4 GHz and is vertically polarized. In addition, a wireless micro-camera is attached to the vehicle and operated at 2.4 GHz, powered by a 9 V battery. The LEAPFROG goal is to embark on 5kg payload on the platform.

2.1.3 Integration

The final configuration is set to have a center of gravity as centered, with the symmetry axis, and low as possible; additionally a small inertia matrix is required to avoid large momentum when the vehicle is spinning. Therefore, the jet engine is placed vertically

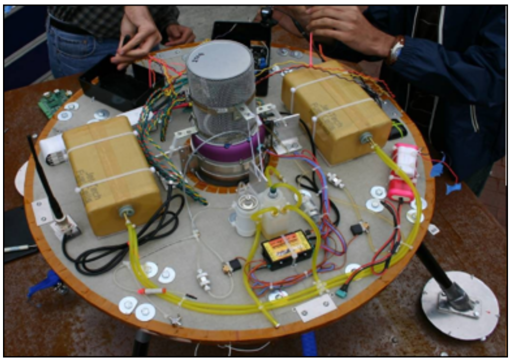

Figure 2.7: Generation-0 integration: top view

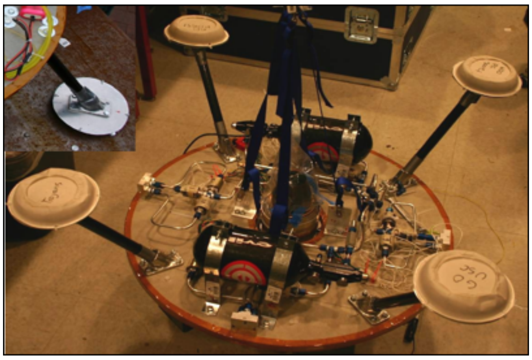

Figure 2.8: Generation-0 integration: bottom view

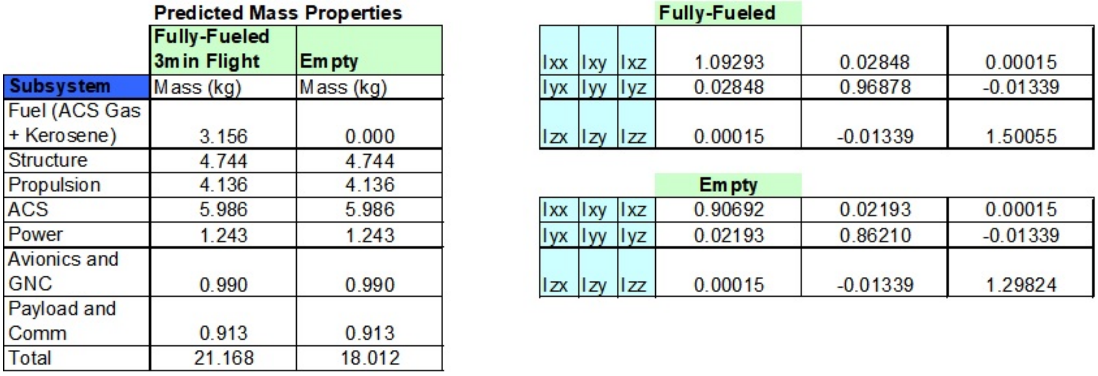

	Predicted Mass Properties	
	Fully-Fueled 3min Flight	Empty
Subsystem	Mass (kg)	Mass (kg)
Fuel (ACS Gas + Kerosene)	3.156	0.000
Structure	4.744	4.744
Propulsion	4.136	4.136
ACS	5.986	5.986
Power	1.243	1.243
Avionics and GNC	0.990	0.990
Payload and Comm	0.913	0.913
Total	21.168	18.012

Fully-Fueled

Ixx	Ixy	Ixz	1.09293	0.02848	0.00015
Iyx	Iyy	Iyz	0.02848	0.96878	-0.01339
Izx	Izy	Izz	0.00015	-0.01339	1.50055

Empty

Ixx	Ixy	Ixz	0.90692	0.02193	0.00015
Iyx	Iyy	Iyz	0.02193	0.86210	-0.01339
Izx	Izy	Izz	0.00015	-0.01339	1.29824

Figure 2.9: Generation-0 Mass Budget

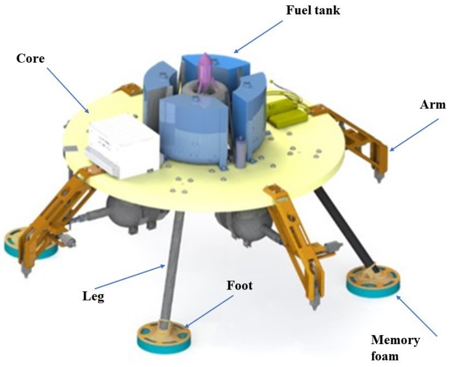

Figure 2.10: CAD Generation-1

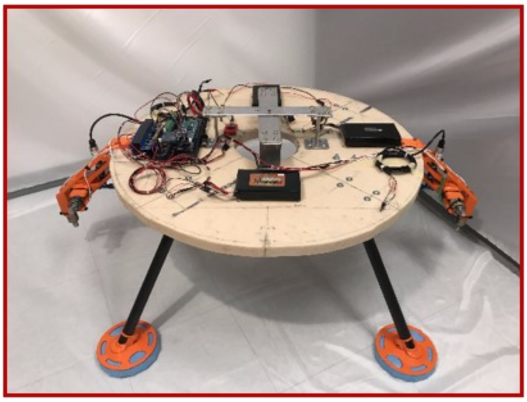

Figure 2.11: Generation-1 vehicle

along the platform symmetry axis, where a hole is cut to fit it in. The ACS, including the tanks, the valves, the pressure gauges and the tubing are placed on the structure's underbelly to lower the center of mass. All the high-pressure circuit is organized to be balanced around the center of the platform. The kerosene fuel tanks were placed on the platform top symmetrically. The power control system is split into two parts and placed in the same way as the fuel tanks, perpendicularly to them. The top and bottom views of LEAPFROG Generation-0 are in Figure 2.7 and Figure 2.8, while the mass budget is shown in Figure 2.9.

Moreover, this configuration has different drawbacks: the fuel tanks are not well placed on the platform and are not well-shaped. Therefore they add inertia to the vehicle. The spread electronics on the top is wasting space for the payload.

2.2 Generation-1

Subsystem improvements regarding the previous one mainly characterize Generation-1: this vehicle is more efficient and robust for the LEAPFROG tests and needs. Therefore subsystems optimization is the milestone of this generation.Figures 2.10 and 2.11 explain the Generation-1 components and show its realized prototype. Indeed, the Figure 2.12 shows the global system block diagram.

2.2.1 Requirements

While project requirements remain the same as those of the Generation-0 (Table 2.1), the updated system requirements are listed in Table 2.3

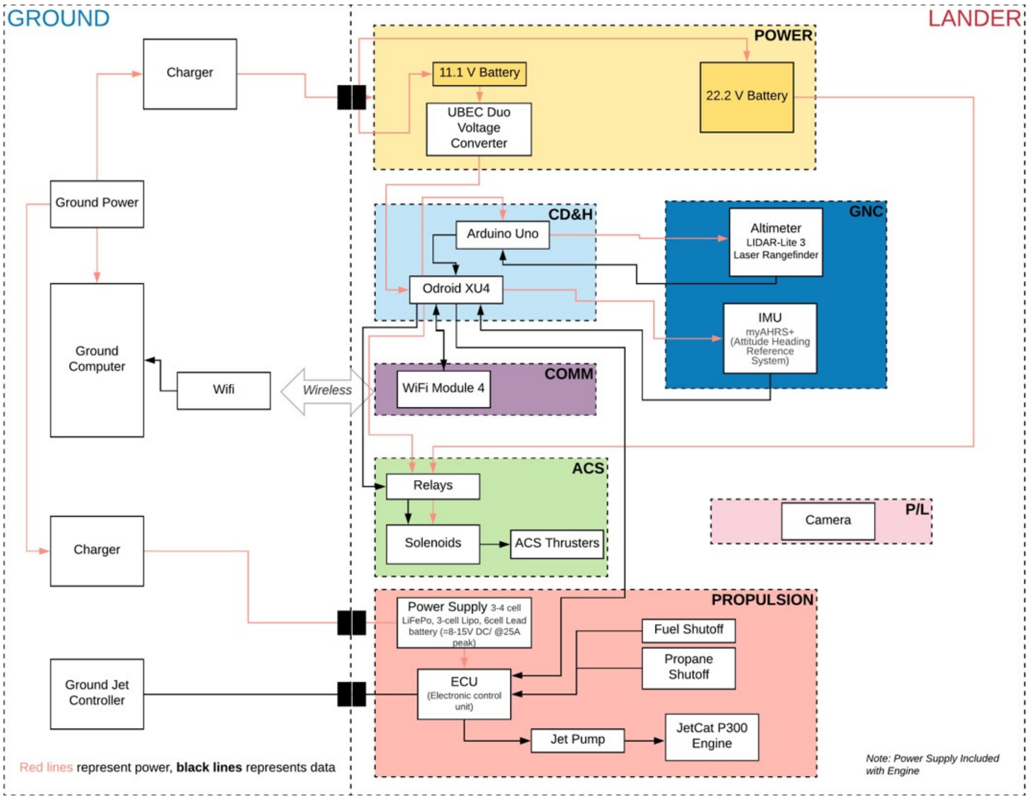

Figure 2.12: Generation-1 Block Diagram

ID	Systems Requirements
R-DSR-01	The thrust to weight ratio shall be grater than 1.2
R-DSR-02	The payload mass shall be less than $10lb$ without hindering vehicle operations or affecting flight dynamics
R-DSR-03	The minimum flight time shall be three minutes
R-DSR-04	The vehicle structure shall withstand a $3ft$ drop test without any components deformation or failure
R-FNR-01	The ACS shall ensure a 6 DOFs vehicle motion
R-OPR-01	The vehicle shall maintains in-line safety and abort commands for all failure modes.

Table 2.3: Generation-1 System Requirements

2.2.2 Subsystems

Jet Propulsion System

A replacement of the JetCat P-200 ($50lbs$ thrust, $5.53lbs$ weight) with the JetCat P-300 ($67lbs$ thrust, $6.02lbs$ weight) is proposed. Consequently, the thrust surplus permits to have a $15lbs$ payload and simulate the Moon gravity and the $0g$. It is intended to use a similar aluminum bracket and basket mounting for the engine, which will be tailored to the engine's diameter and weight to ensure both a secure and tidy engine integration. The following hardware is provided for the whole Jet Propulsion system and its architecture is shown in Figure 2.13.

- A watertight Electronic Control Unit ECU
- A brush-less fuel pump completely sealed, saltwater resistant, high efficient
- An internal routed Exhaust Gas Temperature (EGT) probe
- An electric starter
- A direct kerosene startup
- Shut-off valves for the fuel lines
- Threaded fuel supply connections via $8mm$ tubing with an internal fuel filter
- A 4-pin Power-Bus expansion connector (e.g. for direct connection of a smoker pump, or additional fuel transfer pump)
- A power supply: 3-4 cell LiFePo, 3-cell Lipo, 6cell Lead battery (8-$15V$ DC at $25A$ peak)
- Control interface options: Analog (e.g. 0-$5V$), 1 or 2x Servo PWM, RS232, RS485, CAN-Bus for the control and data reporting
- Electrical connections via 2x pigtail cables/connectors
- A control cable connector: Autosport (9-pin) on 35 cm pigtail

Instead of using rectangular-shaped tanks placed in the middle of the platform upper side, a new type is designed; thus, they can be closer to the platform symmetry axis and more space is available for the payload. The chosen shape is the annuls, divided into four equal parts because of the aluminum engine's presence in between. For maximizing the fuel availability, the tank's bottom shape is toroidal. Three vertical baffles were added inside each tank to avoid vehicle misbehavior during the flight due to the fuel inertia, letting the fuel flow through a small space at the tank's base. In the design phase, integration mounting with the platform is also considered. The Generation-0 tanks are ordered from a local company, the Jet-Tech Fuel Cells. Since the new shape is more complex and expensive in terms of construction, it has been

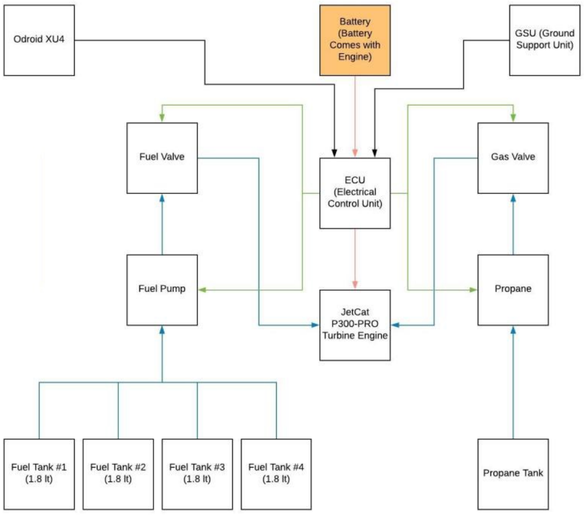

Red lines represent power, **black lines** represents data, green lines represents both data and power, and blue lines represents fuel.

Figure 2.13: Block Diagram of the Jet Propulsion System

decided to 3D-print them and to make them kerosene-proof by coating all the surfaces with epoxy. This is a commonly used method to make the print waterproof; moreover, the epoxy resin is chemically resistant to kerosene. To coat the tank's inner part, the top part of them is printed separately and glued after the coating process with acetone. Moreover, tests to study the sloshing have to be considered for the future; they should be avoided in the perpendicular direction, adding horizontal surfaces.

Attitude Control System

In the previous generation, the vehicle had no yaw control and tubing pressure drops. Therefore, four thrusters are added to the previous configuration, resulting in four vertical for the pitch and roll control, and the remaining are horizontally disposed for the yaw control. Moreover, four tanks are now used and each one provides air to two solenoid valves. Lines attached to the tanks are as compact as possible. In each line, the first component is a pressure regulator to lower the pressure from the tank. Then, there is an adapter to connect the ASA regulator output to the standard $\frac{1}{4}\,inch$ NPT threads. A double-use valve follows, which acts as an On/Off valve and a bleed valve. A pressure transducer is mounted in parallel to the line. At the end, there is a yaw thruster pointing horizontally, perpendicular to the line and a pitch/roll thruster pointing to the ground. This full line includes almost no tubing and is reduced to the strictly necessary. For the regulator, the one used on Generation-0 was provided directly by the paintball tank company, which was not adjustable. The On/Off valve is attached to the 90-degree inclination line just after the regulator's exit but does not fit the new generation arrangement for the line. Because of the bleed valve's weight, a new valve has been found, acting both as a bleed and On/Off valve, with any inclination. The pressure transducers and the solenoid valves are the same as used in Generation-0.

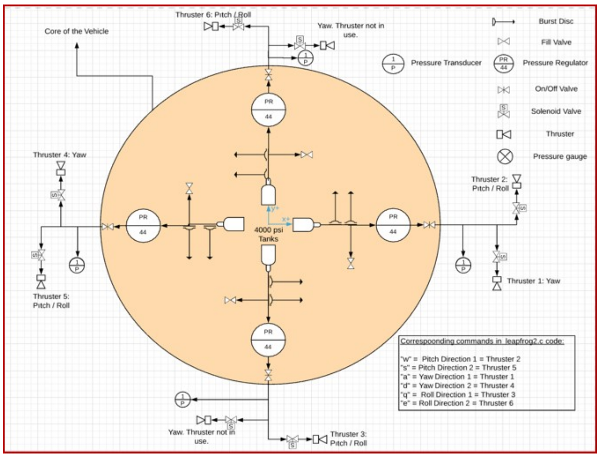

Figure 2.14: Generation-1 ACS Architecture

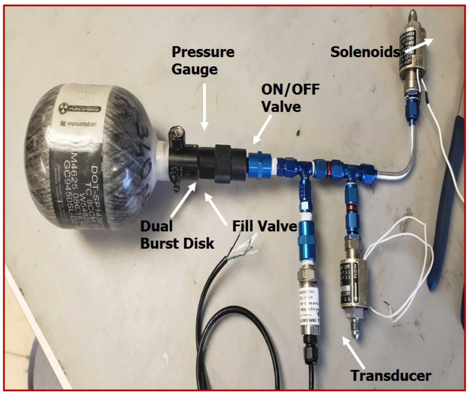

Figure 2.15: Generation-1 ACS hardware

The system architecture and the hardware are shown in Figure 2.14 2.15

Power Control and GNC Systems

The Odroid XU4 micro-controller is used on-board with an Arduino Uno microprocessor. An additional Arduino Uno is preferred due to get altimeter data as straightforward as possible. The Odroid 5A WiFi module is wireless, communicating with the ground station. The altimeter data's selected sensor is TFMini - Micro LiDAR Module, which has a $12m$ threshold. However, the LIDAR-Lite 3 Laser Range could be used with a $40m$ for reaching higher altitude entry. An AmeriDroid myAHRS+ IMU is integrated to provide accelerometer values during the flight-mode. The myAHRS+ is composed by a gyroscope, an accelerometer and a geomagnetic sensor. Data are collected from the USB port when the vehicle is not in the balance point: for its registration, the average from 60 s measurement is done. Therefore, the selected thruster is switched on to change the configuration. The Power Control System diagram is shown in Figure2.16.

Since the same Generation-0 solenoid valves are used, the Power Budget is almost the same. Regarding the avionics, the Odroid XU4 needs to be powered up with 5V and 4A, and no known better option gives directly that output. Therefore, an $11.1V$ battery with 5V and 4A converter was selected. The Arduino Uno is powered up from Odroid XU4's USB port that gives 5V and 1A power output. Moreover, solenoid valves need $22.2V$ and 1A of power supply; Finally, Jet engine starter and power supply are provided with purchase. The Generation-1 power budget is shown in Figure 2.17

Structure

The Generation-0 structure was heavy and not well optimized in terms of free space for a payload. In this framework, many components have been redesigned: starting from

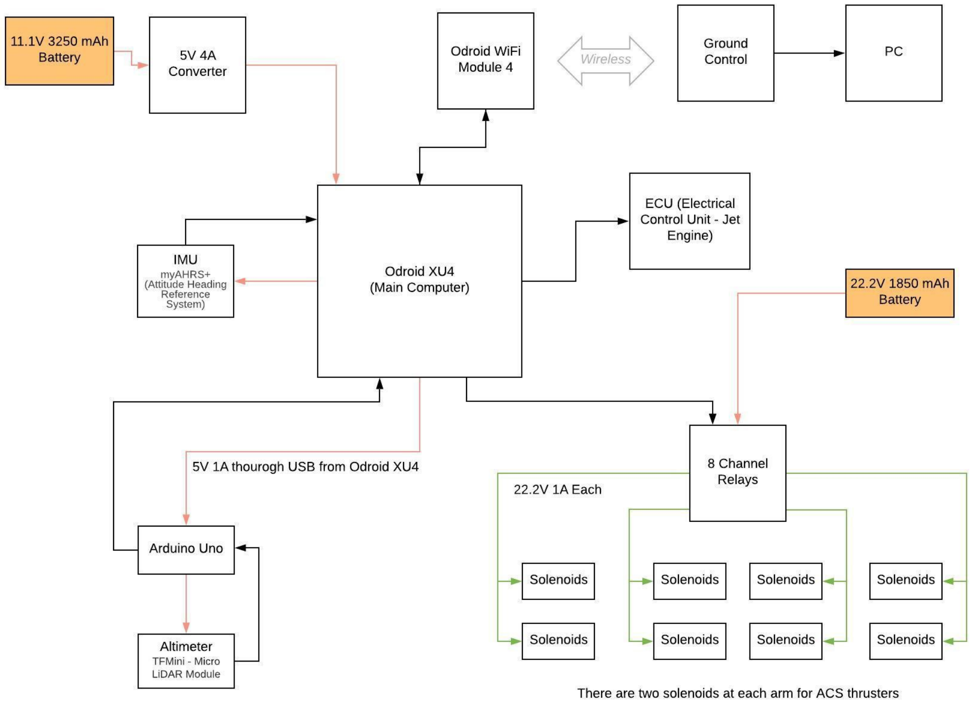

Red lines represent power, **black lines** represents data and green lines represents both data and power.

Figure 2.16: Block Diagram of the Power Control System

Power Spreadsheet	Characteristics					Standby Mode		Flight Mode	
Subsystem	**Voltage**	**Min Amps**	**Max Amps**	**Min Pwr** (W)	**Max Pwr** (W)	**Max Duty** Cycle	**Peak** (W)	**Max Duty** Cycle	**Peak** (W)
ACS									
Thruster Solenoid	22.20	0.90	1.00	19.98	22.20	0%	0.00	50%	11.10
Thruster Solenoid	22.20	0.90	1.00	19.98	22.20	0%	0.00	50%	11.10
Thruster Solenoid	22.20	0.90	1.00	19.98	22.20	0%	0.00	50%	11.10
Thruster Solenoid	22.20	0.90	1.00	19.98	22.20	0%	0.00	50%	11.10
Thruster Solenoid	22.20	0.90	1.00	19.98	22.20	0%	0.00	50%	11.10
Thruster Solenoid	22.20	0.90	1.00	19.98	22.20	0%	0.00	50%	11.10
Thruster Solenoid	22.20	0.90	1.00	19.98	22.20	0%	0.00	50%	11.10
Thruster Solenoid	22.20	0.90	1.00	19.98	22.20	0%	0.00	50%	11.10
Relay	22.20	0.00	0.14	0.02	3.11	1%	0.03	30%	0.93
TOTAL CURRENT/POWER (ACS)			8.14		**180.71**		0.03		89.73
GNC									
Wifi Module 4	5.00	0.40	0.40	5.00	5.00	100%%	5.00	100%	5.00
TOTAL CURRENT/POWER (GNC)			0.40		**5.00**		5.00		5.00
Avionics									
Arduino	5.00	1.00	1.00	5.00	5.00	100%	5.00	100%	5.00
Odroid	5.00	1.00	4.00	5.00	20.00	100%	20.00	100%	20.00
IMU	5.00	0.00	0.20	0.00	1.00	100%	1.00	100%	1.00
Altimeter	5.00	0.00	0.12	0.00	0.12	100%	0.12	100%	0.12
TOTAL CURRENT/POWER (AVIONICS)			5.72		**21.12**		21.12		21.12
	Total Maximum instantaneous current		14.26						

Figure 2.17: Generation-1 Power Budget

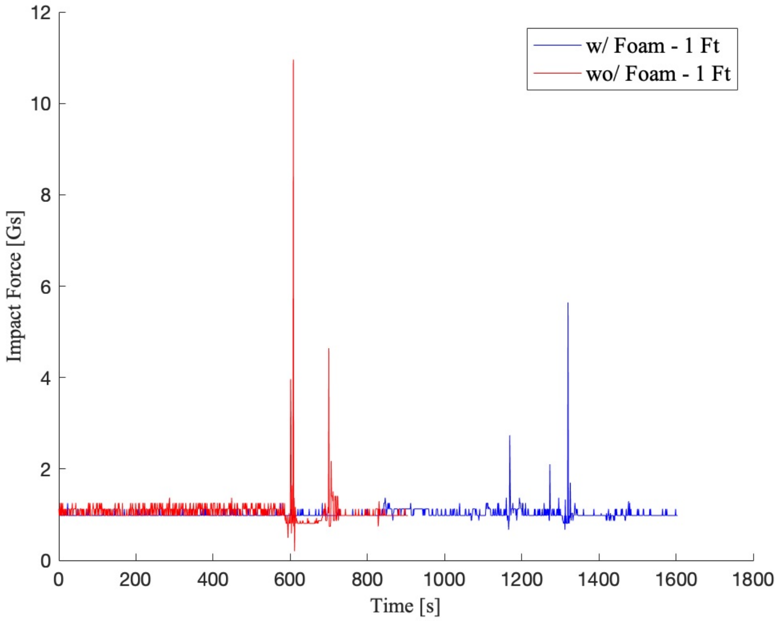

Figure 2.18: $1ft$ drop test results with and without memory foam

the flanges which connects the foam platform to the carbon fiber legs, they are 3D-printed with the ABSPlus-P430, resulting in a reduction of $37g$ of weight compared to the aluminum ones. During 2018, different flanges prototypes were printed and static simulation results are shown in the Appendix A Figure A.1, while real tests have been done screwing the flanges in a wood bench and fixing the carbon fiber leg inside, then adding the weight compatible with the yield stress. Results are shown in Figure A.2 in Appendix A. Regarding the platform, is the same of the Generation-0 one, while the carbon fiber tubes for the legs are unidirectional with an external diameter of $1in$ for this vehicle, resulting in better mechanical properties. Another improvements in this generation vehicle, is made thanks to the Memory Foam which has high damping. The chosen Memory Foam has a deformation of the 25% with $0.6psi$ with a density of $6\frac{lbs}{ft^2}$ and a work temperature range of 50-120F. Different tests have been implemented: the test bench is characterized by a wood bench which guides the weight of $5kg$ to fall down on the foam, shown in Figure A.3 in AppendixA. Different free falls have been analyzed (i.e., $1ft$,$2ft$, $3ft$) and to record data of the shock, we used an accelerometer ADXL377 which is capable to record a $\pm 200g$ scale values every $10ms$. Its implementation on the weight is shown in Figure A.4 in AppendixA. To collect data from ADXL377 an Arduino Uno is used. Figure 2.18 shows results of the accelerometer data collected by a $1ft$ free fall with (blue, maximum impact acceleration of $5.6430gs$) and without (red, maximum impact acceleration of $10.9572gs$) foam. At the end a circular shape of $15cm$ is used for each foot.

The foot design comes from the same procedure done for the flange enforced by a circled base. In order to decrease the foot weight, holes in the horizontal surface are

Figure 2.19: Generation-1 foot

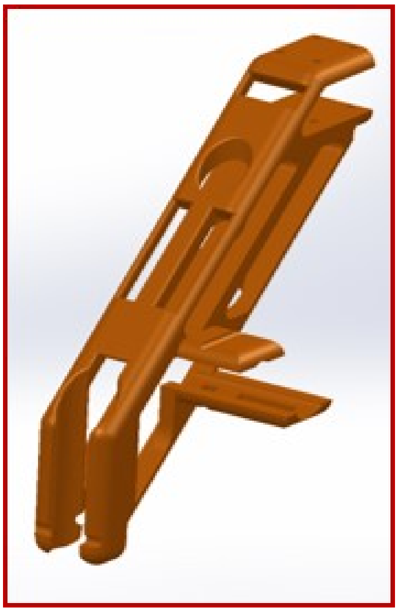

Figure 2.20: Generation-1 arm

made to minimize the foam contact surface. Static simulation results of the whole leg, foot and memory foam are shown in Figure A.5 in Appendix A done in SolidWorks2019.

The ACS design of the new generation is supposed to have 4 lines directed outward the core. Since they are exceeding the platform dimension and a 90-degrees line configuration is needed, a proper structure which can hold them is required. Moreover, it shall resist to the cold-gas thrust and shall ensure thrusters vertical and horizontal positions. The arm design was inspired by drones because the structure shall also be as lighter as possible. Moreover it takes into account the manoeuvrability and the interchangeability for disassembling the ACS. The arm can be seen in Figure 2.20:it is 3D-printed with ABSPlus-P430. Moreover, static simulations consider a static load of $3.09N$ coming from solenoid valves and fixed geometry constraints near the arm platform placement obtaining a maximum Von Mises stress of $35.74psi$ and a maximum displacement of $3.423\times10^{-3}in$. Static simulations results are available in Figure A.6 and Figure A.7 in Appendix A.

2.2.3 Integration

Due to the high presence of different subsystems, a series of Interface Requirements (R-INR) has to be fulfilled. For the legs, arms and ACS integration the requirements are listed in Table 2.4. Problems have been faced in cutting the circular platform shape; furthermore, the core is not fiberglass-epoxy uniformly laminated. The solution adopted to the first problem is using the tracing directly to the platform (Figure 2.24) to precisely locate arms and legs, while for the second one it has been decided to use flattest core sections for flange placement (Figure 2.25). Furthermore, the Generation-1 mass budget is show in the Figure 2.29, having a total mass of 24,10 kg.

ID	Interface Requirements
R-INR-01	Legs shall be symmetrically set-up referring to the platform symmetry axis
R-INR-02	Legs shall ensure full contact between flanges and the platform (Figure 2.21)
R-INR-03	Legs shall properly epoxied into the foot (Figure 2.22)
R-INR-04	Drill holes shall be symmetrical as possible with the 15/64 drill-bit (Figure 2.23)
R-INR-05	Arms shall be symmetrically set-up referring to the platform symmetry axis
R-INR-06	Arms shall fit properly on the platform without creating damages and over-stressing
R-INR-07	Arms shall be placed at 45 degrees from leg axis (Figure 2.26)
R-INR-08	Drill holes should be at appropriate location with 3/16 drill-bit (Figure 2.27)
R-INR-09	The ACS line should fit properly in the arm (Figure 2.28)

Table 2.4: Generation-1 Integration requirements

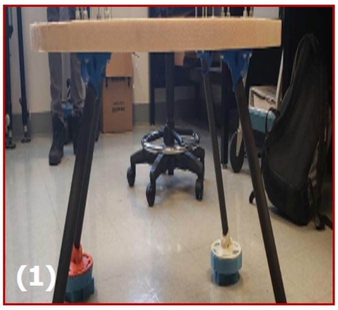

Figure 2.21: Generation-1 Leg Integration (1)

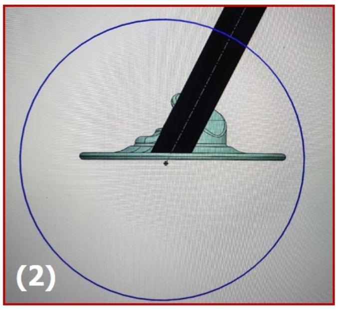

Figure 2.22: Generation-1 Leg Integration (2)

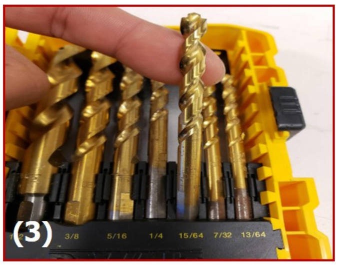

Figure 2.23: Generation-1 Leg Integration (3)

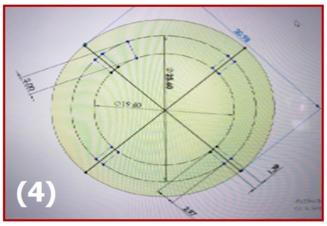

Figure 2.24: Generation-1 Leg Integration (4)

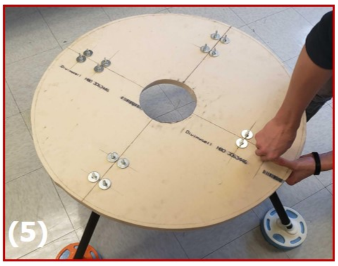

Figure 2.25: Generation-1 Leg Integration (5)

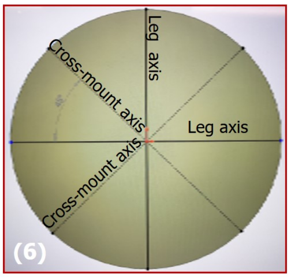

Figure 2.26: Generation-1 Leg Integration (6)

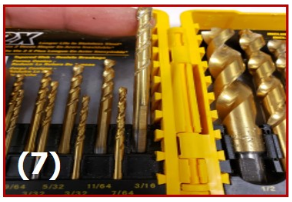

Figure 2.27: Generation-1 Leg Integration (7)

Figure 2.28: Generation-1 Leg Integration (8)

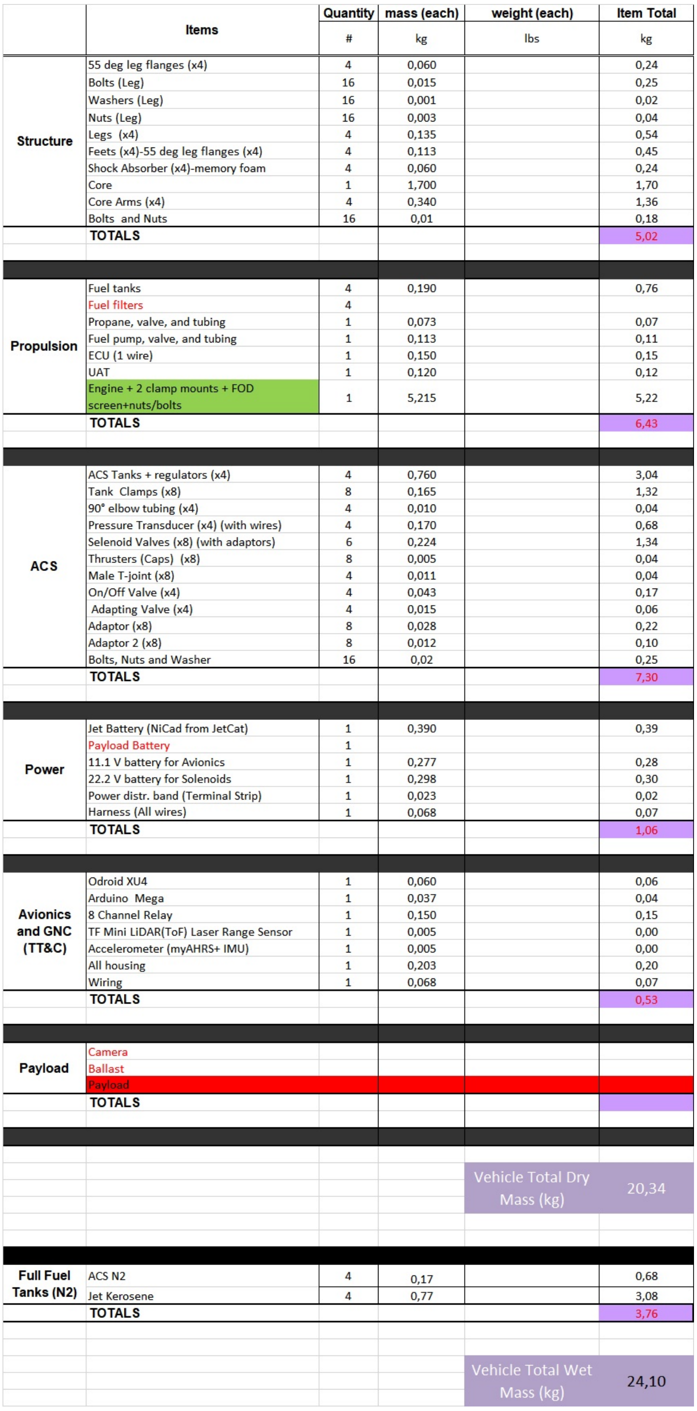

	Items	Quantity	mass (each)	weight (each)	Item Total
		#	kg	lbs	kg
Structure	55 deg leg flanges (x4)	4	0,060		0,24
	Bolts (Leg)	16	0,015		0,25
	Washers (Leg)	16	0,001		0,02
	Nuts (Leg)	16	0,003		0,04
	Legs (x4)	4	0,135		0,54
	Feets (x4)-55 deg leg flanges (x4)	4	0,113		0,45
	Shock Absorber (x4)-memory foam	4	0,060		0,24
	Core	1	1,700		1,70
	Core Arms (x4)	4	0,340		1,36
	Bolts and Nuts	16	0,01		0,18
	TOTALS				5,02
Propulsion	Fuel tanks	4	0,190		0,76
	Fuel filters	4			
	Propane, valve, and tubing	1	0,073		0,07
	Fuel pump, valve, and tubing	1	0,113		0,11
	ECU (1 wire)	1	0,150		0,15
	UAT	1	0,120		0,12
	Engine + 2 clamp mounts + FOD screen+nuts/bolts	1	5,215		5,22
	TOTALS				6,43
ACS	ACS Tanks + regulators (x4)	4	0,760		3,04
	Tank Clamps (x8)	8	0,165		1,32
	90° elbow tubing (x4)	4	0,010		0,04
	Pressure Transducer (x4) (with wires)	4	0,170		0,68
	Selenoid Valves (x8) (with adaptors)	6	0,224		1,34
	Thrusters (Caps) (x8)	8	0,005		0,04
	Male T-joint (x8)	4	0,011		0,04
	On/Off Valve (x4)	4	0,043		0,17
	Adapting Valve (x4)	4	0,015		0,06
	Adaptor (x8)	8	0,028		0,22
	Adaptor 2 (x8)	8	0,012		0,10
	Bolts, Nuts and Washer	16	0,02		0,25
	TOTALS				7,30
Power	Jet Battery (NiCad from JetCat)	1	0,390		0,39
	Payload Battery	1			
	11.1 V battery for Avionics	1	0,277		0,28
	22.2 V battery for Solenoids	1	0,298		0,30
	Power distr. band (Terminal Strip)	1	0,023		0,02
	Harness (All wires)	1	0,068		0,07
	TOTALS				1,06
Avionics and GNC (TT&C)	Odroid XU4	1	0,060		0,06
	Arduino Mega	1	0,037		0,04
	8 Channel Relay	1	0,150		0,15
	TF Mini LiDAR(ToF) Laser Range Sensor	1	0,005		0,00
	Accelerometer (myAHRS+ IMU)	1	0,005		0,00
	All housing	1	0,203		0,20
	Wiring	1	0,068		0,07
	TOTALS				0,53
Payload	Camera				
	Ballast				
	Payload				
	TOTALS				
				Vehicle Total Dry Mass (kg)	20,34
Full Fuel Tanks (N2)	ACS N2	4	0,17		0,68
	Jet Kerosene	4	0,77		3,08
	TOTALS				3,76
				Vehicle Total Wet Mass (kg)	24,10

Figure 2.29: Generation-1 Mass Budget

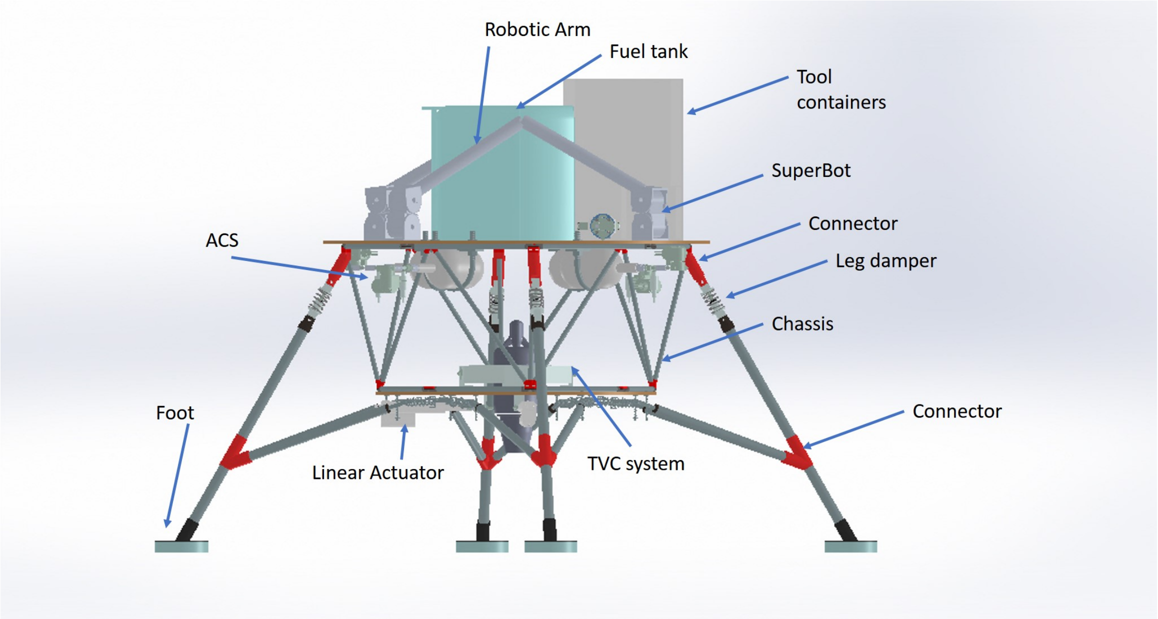

Figure 2.30: Generation-II vehicle

2.3 Generation-II

From September 2019, a new team has been built with the aim of facing new trends in the Moon exploration. After a productive brainstorming, new project requirements have been set as well as system requirements. The main goal is to create a vehicle which serves for more than only one purpose and is permanent and completely autonomous. Nowadays lunar missions have narrowly defined purposes and are only capable of operating in limited areas on the lunar surface and executing specific predetermined tasks. Therefore, the mass sent rarely serves more than a single purpose. The team developed a unique ACS that exploits the interchangeability of a Thrust Vector Control (TVC) of the central jet engine and fixed cold-gas thrusters allowing LEAPFROG to adapt to different thrust values and environmental conditions. A lunar lander with a long mission timeline should be able to recharge the on-board batteries: Generation-II (Figure 2.30) is equipped with a deploy-able on-demand solar panel. It is an Origami Solar Panel (OSP) which extends up to six times its folded configuration. Another element which exploits the vehicle multi-functionality is the on-board robotic arm which is utilized to manipulate different tools: the OSP when needed, otherwise it will first extend its length and it will augment its DOFs to handle a drill, a shovel, a gripper. Unlike other robotic arms which are typically held down with flight locks when not in operation, this arm acts as a secondary structure that ensures the stability of fuel tanks during its non-operative mode. LEAPFROG is versatile and affordable. Since the on-board tools and the final design of the RAMSEs are still under study and they are considered as on-going research projects, it has been decided to realize part of the Generation-II, such its structure, the ACS, the jet engine and the TVC system to test them separately from the multi-functional systems. Therefore, it has been decided not

ID	Project Requirements
R-HLR-01	Shall exploit the multi-functionality
R-HLR-02	Shall be completely built by students by using COTS and USC already developed and tested technologies
R-HLR-03	The overall cost shall be below 20k$
R-HLR-04	Shall be totally reusable
R-HLR-05	Shall simulate Moon landing on Earth environment
R-HLR-06	Shall embark a payload to be tested on-board
R-HLR-07	Shall guarantee the payload safeness

Table 2.5: Generation-II Project Requirements

to buy the most suitable engine (JetCat Pro-550 with a maximum Thrust of $550N$) for high cost reasons, and to purchase the best one only once the mass budget has been set.

2.3.1 Requirements

Project and System requirements are slightly changed for this generation and they are listed in Table 2.5 and Table2.6.

2.3.2 Subsystems

Structure

The first vehicle design phase has been focused on the structure, which has to increase the loaded mass and available space. Therefore, a double-layer configuration is preferred to leave a suitable workspace for the manipulator and keep it far from the engine for thermal reasons and from the ACS for not complicating its design or creating interference between the subsystems. Moreover, as stated by R-DSR-05, it is better to have more space available for a payload. The two layers are connected through an internal chassis (Figure 2.31 and Figure 2.32): the two axes shown are in inertia's principal plane axis.

The total height of the structure is 86.6 cm, the full width is about 178 cm, while the whole mass is $8kg$.

Initially, the chassis was made of two circular beams in each plane connected through different trusses, but due to the high cost of realization, the octagonal shape

ID	**Systems Requirements**
R-DSR-01	The vehicle shall hover, translate laterally and maintain rotational stability
R-DSR-02	The vehicle should be completely autonomous for a long-time mission
R-DSR-03	The thrust to weight ratio shall be grater than 1.2
R-DSR-04	The vehicle structure shall withstand a $3m$ drop test without any components deformation or failure
R-DSR-05	The vehicle shall increase the payload capacity from the Generation-1
R-DSR-06	The vehicle shall enable a re-configurable structure
R-DSR-07	The gimbal shall be as light as possible to avoid extra mass on the vehicle
R-DSR-08	The gimbal shall have enough resistance in order to withstand the thrust given by the engine
R-DSR-09	For the gimbal design COTS materials shall be used,in order to keep the cost sufficiently low
R-DSR-10	The gimbal shall be realized in the SERC laboratories
R-FNR-01	The propulsion system and ACS shall ensure a 6 DOFs vehicle motion
R-FNR-02	The vehicle shall be capable to land and take-off multiple times through the same firing
R-OPR-01	The vehicle shall maintains in-line safety and abort commands for all failure modes

Table 2.6: Generation-II Systems Requirements

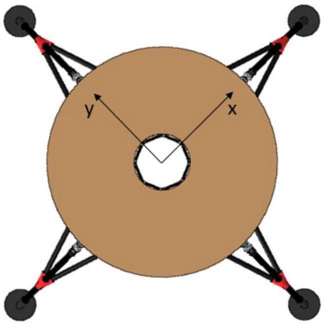

Figure 2.31: Generation-II structure front view

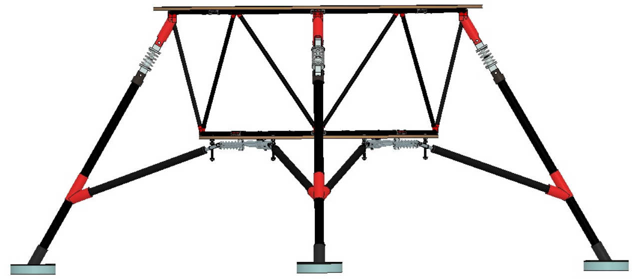

Figure 2.32: Generation-II structure side view

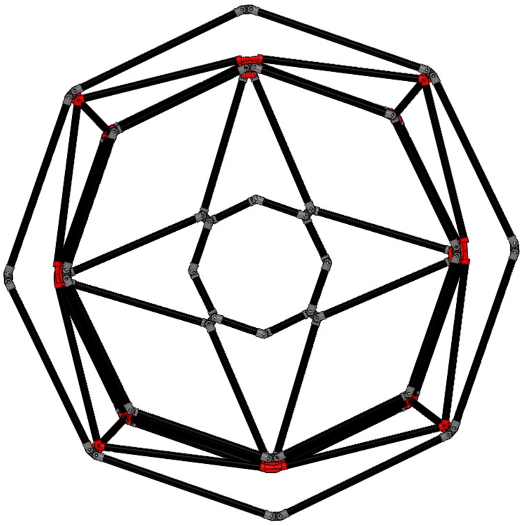

Figure 2.33: Generation-II chassis top view

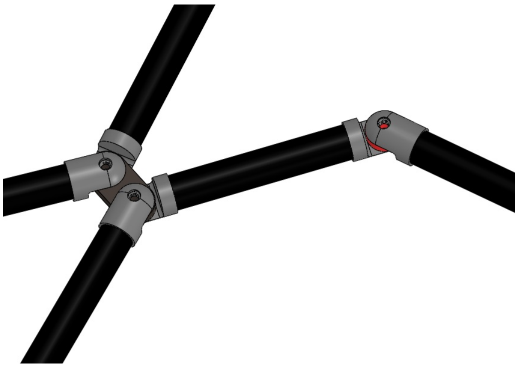

Figure 2.34: Generation-II chassis connectors detail

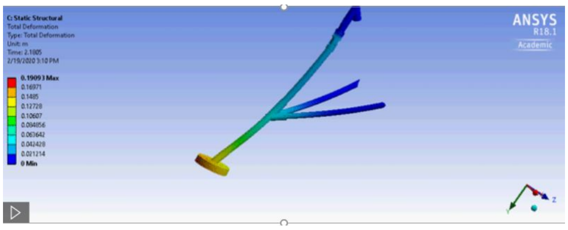

Figure 2.35: Generation-II structural elements modeled in NX and Ansys for stability and dynamics

is used. Since trusses are made of 2X2 Twill Weave carbon fiber, with an internal diameter of $0.5in$, suitable connectors are both purchased from DragonPlate company or printed in the laboratory with ABSPlus-P430 because of the particular trusses inclination: red parts in Figure 2.33 are those connectors realized in SERC. The overall chassis is realized by epoxying carbon fiber tubes, connectors and Black Oxide Stainless Steel threads.

The four-leg configuration is also applied in this new prototype. Still, new elements are added due to the two layers' presence and to augment the damping capabilities after each landing. Therefore, each leg is composed of two $0.875in$ (internal diameter) filament wound - unsanded beams connected though a 3D-printed connector to the $1.075in$ main beam which has the same pattern of the previous ones. A bike shock absorber is added between the connector with the chassis and the leg to have a better damping response during landings.

A simulation of a $3m$ free fall totally on one leg of the vehicle (Figure 2.35) shows a reasonable maximum deformation with this leg configuration. The connectors attached to the chassis are modeled as fixed boundary conditions. The reason behind the shock absorber use is the team wants to design the feet to remove the memory foam. Further studies between the interaction of the Moon soil mechanics and this foot configuration have to be done. This particular geometry is chosen to distribute the load evenly among the chassis, avoiding a full concentration in a single point. Furthermore, the legs' specific inclination is due to stability reasons and avoiding possible issues that could be encountered due to the engine's presence. The motor is placed in correspondence to the lower layer of the chassis, and the high temperature of the exhaust gases could affect the carbon fiber. A high inclination keeps the legs as far as possible from the engine. As mentioned before, the foot is still the same as the previous generation; therefore, they are made of a 3D-printed part connected to the memory foam.

The two platforms connected on the upper and lower layer of the chassis are the storage area for subsystems equipped on the prototype. Both of them are characterized by a circular shape and a circular hole in the middle. The holes are like that because the lower disc will have the engine going through it while the upper surface one ensures that enough air comes to the engine itself. The material used for realizing the platforms is an H-100 polyvinyl chloride (PVC) material stiffened with an epoxy and fiberglass lamination, with the same procedure used for the realization of the platforms mounted on previous prototypes. The choice for this material is due to its high strength to weight ratio The attachment to the chassis is performed through particular rounded mounting brackets.

There are different elements on the top surface (Figure 2.36 and Figure 2.37): the tank, the RAMSEs which acts as a secondary structure during the lander operative mode, holding the tank in the vicinity of its fourth rotational joint and the tools it has to manipulate. The tank is completely attached to the containers to guarantee the symmetry of the top platform center of mass and the stability during the lander motion. In this Generation-II, a proper design of the boxes still has to be done because tools provided in Figure 2.36 are there to show their placement once their design is complete, and understand where the grabbing point is for the RAMSEs end-effector.

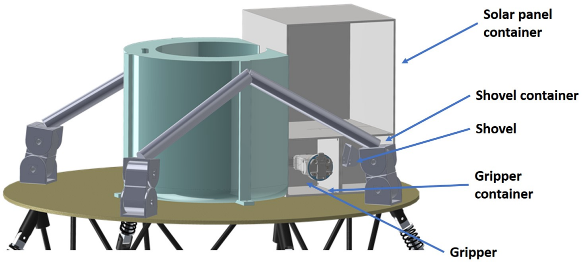

Figure 2.36: Detail of tool boxes

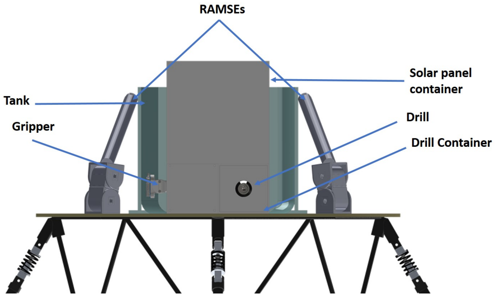

Figure 2.37: Side detail of tool boxes

Therefore, once tools geometry and mass are ready, suitable containers have to be designed. Moreover, it will be shown the OSP box has to have a smaller height to avoid interference with the RAMSEs motion. All the packages are here screwdriven together to prevent relative movement during the lander motion.

Jet Propulsion and Thrust Vector Control Systems

Also in this generation, the main engine is a kerosene powered jet one and is the same of the Generation-1 vehicle, the JetCat P-300. This engine has a single compressor stage, a combustion chamber and a single turbine stage. JetCat Company provides it with its own telemetry and an embedded ECU, which manages fuel pumps, valves and the engine electronic system. There is also an integrated starter for the initial firing. The propellant used to feed the engine, is stored in the upper platform tank: its design is inspired by its version in the previous generation but, this time, the tank is only one and has a little bit more than a semi-circular shape with a toroidal base. Its volume is of 2.72 L The design of the Thrust Vector Control System (TVC) has been done as a master thesis research from LEAPFROG one member [43]: the TVC system is mainly in lander spacecrafts for keeping the thrust vector parallel to the velocity of the spacecraft itself during landing maneuvers, in order to slow down and pursue a final soft landing. The engine cannot be customized, consequently is not possible to realize a gimbaled nozzle and the remained options are to deflect the exhaust gases or the mechanical manipulation of the engine, which is the team choice. A simple gimbal joint cannot be used with this engine since the upper part must be free to allow the air entering therefore an external gimbal ring is used. This is a gyroscopic joint composed by a set of concentric rings which can rotate one each other, along different directions. This joint, connected around a body, allows the body itself to tilt in any wanted direction. The final design of the gimbal ring provides three concentric rings where the inner one is directly connected to the engine and the outer one is attached to the chassis. The connection between the inner ring and the engine is obtained through particular clamps (available in Appendix A) that comes from the same engine company. Thanks to the three ring configuration there is one degree of freedom with the relative rotation of the inner ring with respect the middle ring and another degree of freedom with the relative rotation of the middle ring with respect the outer one.

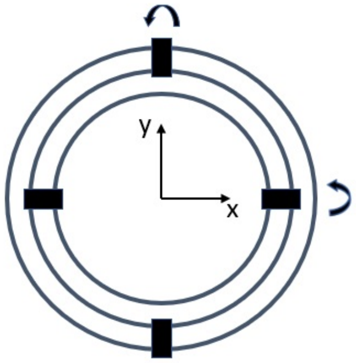

Figure 2.38: Generation-II conceptual sketch of the gimbal rings

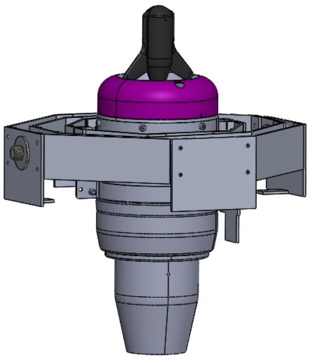

Figure 2.39: TVC Rest condition

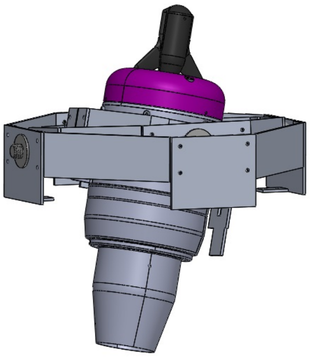

Figure 2.40: TVC Displacement condition

The rotations are allowed by pins that interconnect rings and have the role of the axis of rotation. From Figure 2.38 the gimbal's axis of rotation are perfectly aligned with the principal axis of inertia of the vehicle (x and y in the Figure). The choice is related to a simpler actuation procedure since, in case of pure pitch or pure roll motion, the control torque can be provided by rotating only one of the rings so, activating only one linear actuator.

Likewise the previous generation, other interface requirements were stated during the design process (Table 2.6): particularly, for the gimbal joint design one must refer to R-DSR-07, R-INR-08, R-INR-09 and R-INR-10. The material chosen is a 3 *mm* thick aluminum 6061-T6. This material is widely used, also for aerospace applications, for its good machinability, medium to high strength and light weight, all of that at an affordable price. The inter-connecting pins are made of stainless steel screwed shaft where a couple of bushings are placed in order to facilitate the rotation. The distance between rings is kept through the usage of spacers. Bushings and spacers are made in stainless steel too. Concerning the geometry, the first and most intuitive idea was the realization of simple rounded shape rings to connect with pins. However, this geometry has some issues in terms of attachment to the structure and in terms of manufacturing. A round shape, in fact, requires a very precise bending of the aluminum sheet, hard to achieve with the available machines. Moreover, just because the gimbal ring is made out from aluminum sheets, a full body ring has not been available. For this reason, the final decision has been to build the gimbal joint by assembling together different aluminum plates, easy to realize with the available equipment. The final shape recalls the octagonal geometry of the lower layer of the chassis in order to get an easier attachments between the two parts (Figure 2.39 and Figure 2.39). In addiction, the inner ring of the joint also hosts two vertical plates that run along the sides of the engine and that are used as a connection point for the actuators. In order to save money, actuators chosen are remaining ones available at SERC from a different project. This

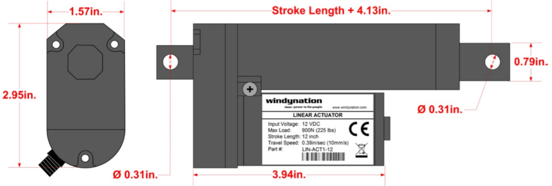

Figure 2.41: Windynation linear actuator [6]

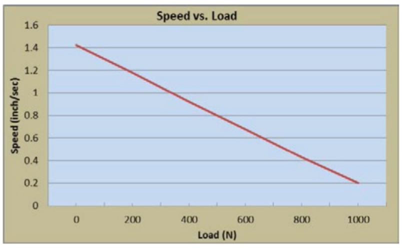

Figure 2.42: Actuators speed vs load [6]

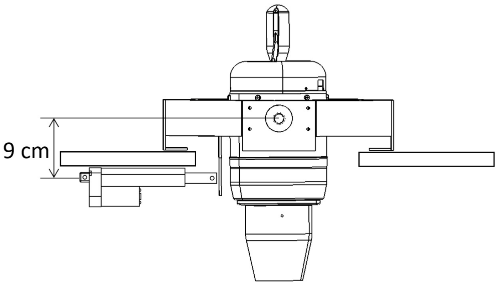

Figure 2.43: Actuators installation scheme

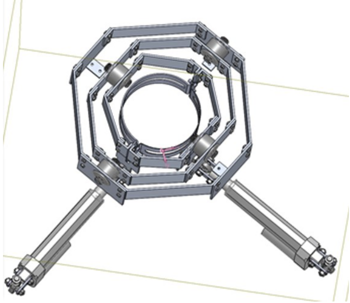

Figure 2.44: Detailed TVC design

has been challenged the design, because actuators' work has to be optimized in order to get the best performance out of them. They are industrial linear electro-mechanical actuators from Windynation company (Windynation LIN-ACT1-04 in Figure 2.41). They have a duty cycle of 25%, which means to have a 75% of non working condition. Therefore, a full TVC-based control system is hard to have: the duty cycle problem could be avoided with hydraulic actuators. The good point is the actuators have only to face the engine inertia since the engine is totally sustained by the gimbal ring so the speed of actuation is considerable high (Figure2.42), around $30\frac{mm}{s}$. A further improvement is achieved minimizing as much as possible the distance between the gimbal point (i.e. the point around which the rotation of the engine occurs) and the point in which the single actuator acts on the engine itself which is set as $9cm$ (Figure 2.43).

Considering the interference with the chassis, the engine angular motion is limited by the *Gimbal offset angle* δ which is the angle between the vertical direction and the current thrust direction: $0<\delta<5$. Therefore, considering the angular actuation speed previously specified, a fast actuation can be obtained in the whole work range, since the entire angular displacement 10° is covered in less than one second.

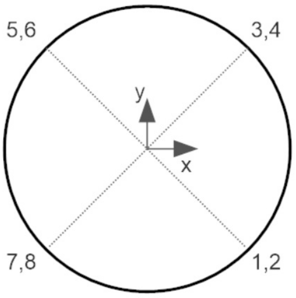

Figure 2.45: ACS thrusters placement

Attitude Control System

The ACS is composed by 8 thrusters and it is inspired by the previous one generation. They are distributed along the upper platform circumference but in its bottom side as shown in Figure 2.45. The two axis depicted represent the in-plane principal axes of inertia (the z axis is perpendicular and coming out the plane). The eight thrusters are placed such that 4 of them (number 2,4,6,8) are used for yaw control and the other 4 (number 1,3,5,7) for roll/pitch control. The reason of the 45° offset between the thrusters position and the principal axis of inertia is due to the fact that the latter run through the legs of the prototype and placing thrusters above them will result in disturbances due to the interaction between the cold-gas and legs. Clearly, not having thrusters aligned with principal axes of inertia, the rotation angles cannot be controlled with a single thruster but a combination of them is required. In particular, the firing logic is the following:

- positive yawing moment → 2 and 6 are firing
- negative yawing moment → 4 and 8 are firing
- positive rolling moment → 1 and 3 are firing
- negative rolling moment → 5 and 7 are firing
- positive pitching moment → 1 and 7 are firing
- negative pitching moment → 3 and 5 are firing

The system architecture is basically the same of the previous generation and the only difference is the new type of solenoid valves which are more compact and avoids complex inclined lines.

Power Control and GNC Systems

Nowadays only a sub-part of the full power control system is ready, therefore a complete Power-Budget is still not available. The Figure 2.46 shows the electronics needed for the lander operative mode, that is when it takes off and lands somewhere.

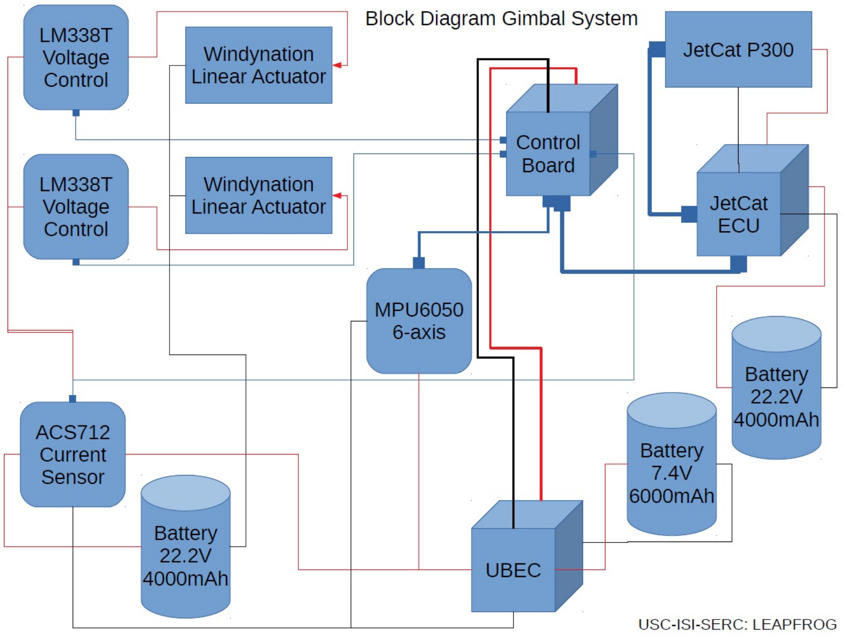

Figure 2.46: Thrust vectoring system embedded electronics

The red and black cables represent an electric connection in which, the first type represents the positive pole and the second the negative one. Blue cables, instead, represent a data connection between the different blocks. The central core of the electronics system is represented by the control board, an Odroid CPU that exchanges information with LEAPFROG'S main CPU and IMU sensor. When the main CPU commands a variation of thrust vector amount, the control board feeds the information to the engine ECU that manages the engine performance. The power needed by the JetCat ECU and by the control board is furnished by a couple of LiPo batteries. In the case of the control board, the power coming from the battery is first processed by the UBEC block, a voltage regulator that feeds to the CPU a constant power with the proper values of voltage and current intensity. In the case, in which the main LEAPFROG'S CPU commands, an attitude adjustment maneuver, the control board communicates with the transistors that manage the on-off switching of the actuators. The transistors are identified by the 2 blocks LM338T Voltage control. Those components, according to the signal received by the control board, change the sign of the voltage given to the actuators, triggering the forward motion or the backward motion of the latter. The power needed by the actuators is furnished by a third LiPo battery. A current sensor is placed in the circuit in order to know the amount of current that is actually flowing. The battery used to power the actuators affects their performance and can reduce their speed while the stored energy reduces and becomes a small amount. The last block sketched in the block diagram is a 6-axis IMU sensor. This extra IMU is placed on the inner ring of the gimbal joint and is used to have a feedback on the tilted position of the engine.

Chapter 3

RAMSEs

During the initial brainstorming for the Generation-II development a series of requirements has been defined for each subsystem, to better finalize its design process. Indeed, Table 3.1 summarizes the RAMSEs requirements.

3.1 System Requirements

ID	Name	Requirement Statement
R-HLR-01.01	Ground activities	The RAMSEs should be capable to perform different activities on the ground, like drilling, take samples and digging
R-HLR-01.02	Battery charge	The RAMSEs should be capable to take the solar panel and deploy it when the lander is in the non-operative mode
R-HLR-02	Secondary structure	The system, when is in the non-operative mode, should be capable to sustain tanks during lander flight and maneuver modes
R-INR-01	Lander structure	The RAMSEs should be fixed to the upper platform
R-INR-02	Tools	The RAMSEs should reach all tools from the upper platform
R-INR-03	Soil	The RAMSEs should be capable to reach the soil to perform activities

R-INR-04	Panel deployment	The RAMSEs should deploy the solar panel on the upper platform without interacting with other subsystems
R-ENR-01	Vibrations	The RAMSEs should sustain the level of vibrations which comes from the lander take-off, hovering and landing phases
R-ENR-02	Axial acceleration	The RAMSEs should be capable to withstand the axial acceleration of 2g
R-PHR-01	Mass	The RAMSEs should not exceed the total mass of $10kg$
R-PHR-02.01	Links length	Every link should be of the same length and the maximum RAMSEs total length should not exceed $504mm$
R-PHR-02.02	Links mass	Every link should have a maximum mass of $3kg$
R-CFR-01	Control	The RAMSEs should have its own controller
R-CFR-02	SuperBot	The RAMSEs should have at least two SuperBot units, one should be the first joint, the last would be the end-effector
R-DSR-01.01	Low-cost materials	The RAMSEs should be easily realized in USC laboratories
R-DSR-01.02	Links material	The RAMSEs links should be printed in laboratories with ABS-P430 material
R-DSR-02	Chassis link	The RAMSEs base should be directly attached to the chassis for the proper distribution of loads.
R-DSR-03	Position	The RAMSEs should be tilted of 45° referring to the center of the upper lander platform reference system
R-DSR-04	Tank attachment	The RAMSEs should have symmetric attachments to the tank during lander flight, take-off, and hovering

R-PAR-01	Reconfiguration	In the case of joints malfunctions, the RAMSEs should be capable to replace them autonomously

3.2 System trade-off design

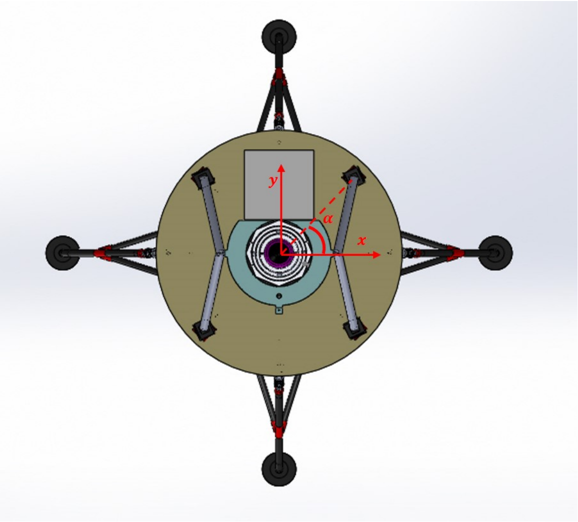

Figure 3.1: RAMSEs platform arrangement

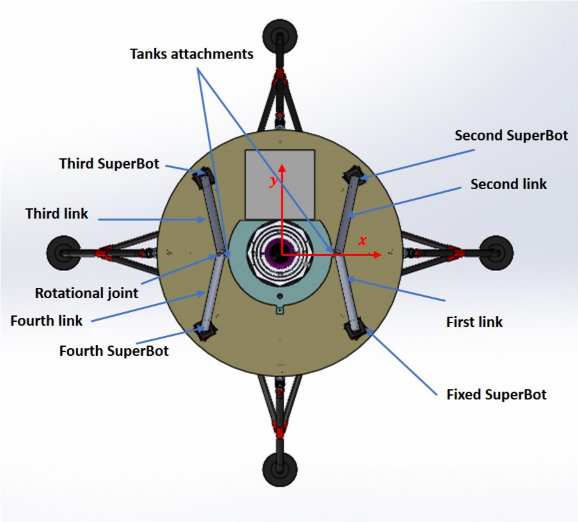

Figure 3.2: RAMSEs CAD description

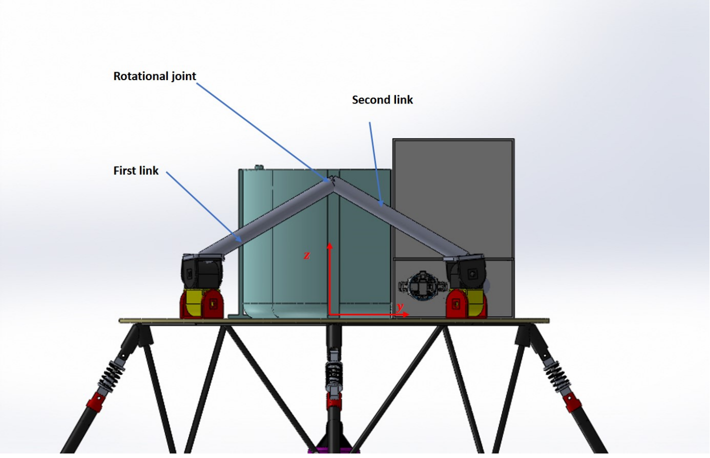

Figure 3.3: RAMSEs CAD description zy plane

In Figure 3.1 the RAMSEs arrangement is shown: the robot is made of two different manipulators with 7 DOFs each. The main one, which is permanently attached at its base, is the right one, referring to the inertial frame on the upper platform, in red in the previous figure. This is used alone for manipulating the OSP since its extended length should be enough to reach a fixed point just upper the tank, and should not be

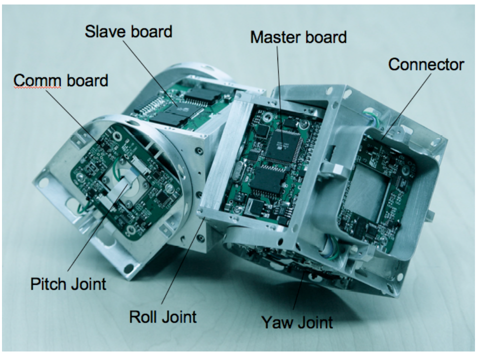

Figure 3.4: SuperBot Module Design

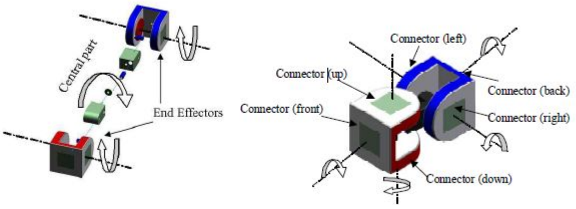

Figure 3.5: SuperBot module scheme and DOFs

too long to reach the soil as if it has to perform soil activities. Indeed, in this case, it has to extend its length of the double due to the lander height and the second robotic arm will detach its end-effector from the platform to link itself with the main robotic arm end-effector. This movement is perfectly symmetric to the axis origin. When the RAMSEs has to perform soil activities, its DOFs are 14. Each manipulator is made of:

- 2 SuperBot units with 3 rotational joints each
- 2 basic trusses (*links*)
- one rotational joint between the two links

The fixed base is the first SuperBot one in Figure 3.2 tilted of $\alpha = 45°$as well as all SuperBot modules; the end-effector of the first arm is the second SuperBot one. The configuration is symmetric for the other arm as mentioned before. Links are simply modelled as full tubes of $400mm$ length with a weight of $1kg$ to satisfy mass requirements. After this research, tubes can be modelled with a most suitable shape considering to add mounting points for sustaining the tank during the lander flight mode. The two links are connected in the CAD with an hinge, since the most appropriate rotational actuator will be chosen a postetiori by considering this research results. Moreover, this joint position limits are set as $0 \div 180°$ like the widely available COTS actuators.

3.2.1 SuperBot

Self-reconfiguration is a highly appreciate characteristic for permanent or long-term missions, since leads to augment systems functionality and maintenance: in case tasks or environment are not well known the system can meet easily changeable operational demands.

For this reason, SuperBot is a self-reconfigurable system and is the most suitable robot for the Generation-II aims [44]. SuperBot is a $1kg$ with a 3 DOFs robot made up of two interconnected aluminium alloy cubes of 84x84x84 mm (Figure 3.4). Each module has three main parts: two end-effectors and a rotating central part. It has

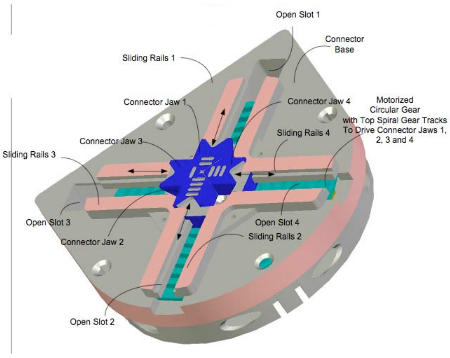

Figure 3.6: The SINGO connection mechanism

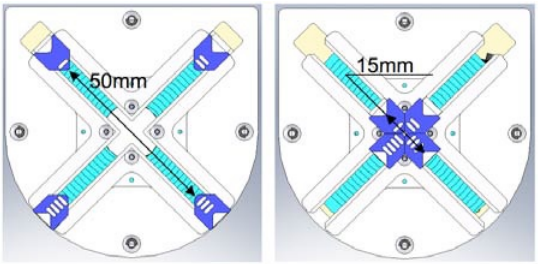

Figure 3.7: The SINGO connector dimensions

three rotational joints in total which corresponds to 180°yaw, 180°pitch and 270°roll (Figure 3.5). This allows a single module to bend and twist, providing flexibility for the multimode locomotion. There are six connectors on the module, one on each side of the end-effectors and they can connect to another module. The drive train of each joint consists in a MicroMo® DC electric motor, a planetary gearbox and an external gearbox: the gear ratio of the first one is 1:86 with an efficiency of 70%, while the the second one is 1:5. The maximum admissible torque is $6.38Nm$, therefore one unit is capable to lift three neighboring modules. SuperBot has a modular hardware architecture: each module's on-board hardware is responsible for controlling the actuators, connectors, sensors, handling the power management, communicating with neighboring modules, making autonomous decisions and distributing control for high-level behaviours. Each cube has a controller: one is called *master controller* and the other *slave controller*. They are both connected with power lines and a bidirectional $400kb/s$ I2C bus, which is a two wire bus and is selected to provide enough bandwidth between cubes. Each controller is based on a 16 MHz ATmega128 micro-controller. Regarding the master controller, a wireless receiver is considered for remote on/off, motor disabling, for stopping modules when the control program is running and receiving commands. The end-effector angular position is detected by a potentiometer coupled to its shaft and is connected to an A/D line of the Atemga128. A SPI communication bus is used to have enough bandwidth for three dock faces. This is also interfaced with a 3D accelerometer. Moreover a JTAG port is used for debugging purposes. The communication interface has four infrared receiver and a transmitter, which signal is sent to a buffer: its output is connected to an A/D channel of the corresponding controller; therefore, the controller can measure the intensity of the input signal. Moreover, receivers can read the analogue signal produced by a reflection of the module's own transmitter LED. The stage amplifier is used to shape a digital signal received from another module during the communication process. Therefore modules can communicate from one meter. SuperBot reconfiguration capability has been studied for many years also for the space environment [45]; different modules connected each other can be used as a manipulator with an high interchangeability in case one of the units will have a damage. For this reason, one of the RAMSEs requirement has been settled for having at least one unit of SuperBot. Moreover, in case soil activities performed by RAMSEs will require higher torque compared to that one available nowadays. Since the R-PHR-01 is requiring a low mass, no more than ten SuperBot units can be used, five arranged symmetrically with respect to y axes of the inertial frame. Therefore, the best option is to use a double trusses configuration between two SuperBot units, adding another rotational joint among links.

For this research, SuperBot is modelled with only one end-effector where a Single Single-End-Operative and Gender-less Connector SINGO is placed [46]. The connector is made of four jaws which can be opened and closed, working in a vice or outwards. In operation, the jaws can move towards the center to engage another connector or away to disengage (Figure 3.6). The base has four open slots to expose motorized circular gears which has concentric tracks that are engaged to the bottom of the jaws. As the circular gear rotates, it drives the jaws along their respective sliding rails: they move simultaneously since only one gear is present. the mechanism is driven by a micro motor. SINGO benefits of being:

- a gender-less structure
- single side operated, hence can connect or release itself even if the other party is damaged
- thin, efficient, with a mechanical strong profile
- self-aligned in both orientation and displacement during connection and engaging process
- integrated with sensors and controllers

The outline of the connector is $64mm$ in diameter and $14mm$ thick. When the four jaws are completely open, the max distance between jaws is $50mm$. When they are closed at the center, the minimal distance across the jaws is $15mm$ (Figure 3.7). Since SINGO add another DOF at one SuperBot unit, its transnational joint is not considered in the RAMSEs kinematics; however the code is equipped to add it in the future. This is because its real CAD is not available, therefore its physics is not modelled carefully.

3.3 System Architecture

In Figure 3.8 RAMSEs architecture is shown. The robot physics is simulated trough Simscape, an extension of Simulink which helps to develop control systems and test system-level performance. In the future, this part will be exchanged with the real hardware. On the other hand, for the controller Simulink environment is used: starting from points that the end-effector should follow, called *waypoints* there is a supervisory logic which calculates where the end-effector should arrive at, then the inverse kinematics is calculated, to provide joints positions in space and with a closed loop, the forward trajectory is computed to find the end-effector placement.

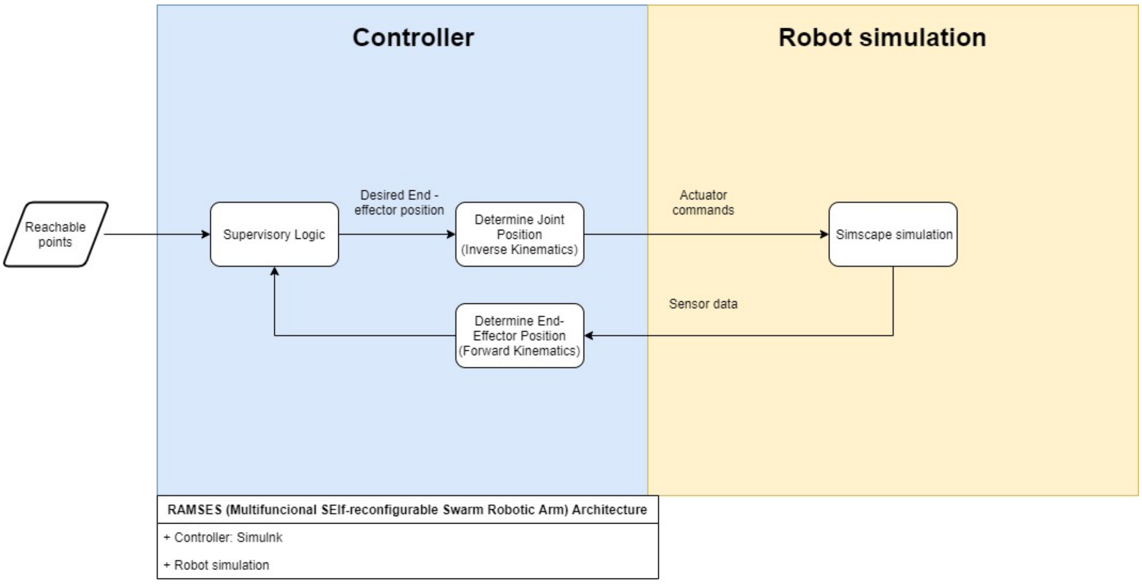

Figure 3.8: RAMSEs architecture

3.3.1 Modelling the kinematics

The RAMSEs is a robotic manipulator, since it has the base fixed on the platform. Here is presented the *kinematics* of manipulators. there are two complementary tasks in kinematics [47]:

- *Forward kinematics*: with a sequence of commands, the final position of the manipulator is computed
- *Inverse kinematics*: with a desired position of the end-effector, computes the sequence of commands for reaching that location

Forward kinematics is easy to compute because the calculation of the change in position that results from moving each joint involves simple trigonometry. If there is more than one link, the final position is calculated by performing the calculations for one joint after another. On the other hand, inverse kinematics could bring to a solution, multiple solution or no solution at all.Kinematic computations are performed in terms of coordinate frames. A frame is attached to each joint of the manipulator and motion is described as transformations from one frame to another by rotations and translations. For computing the inverse kinematics, the *workspace* of the arm is strictly important: it is the 3D space that the manipulator can reach with all its joints and it is dependant by the joint limitations and the link extension. A manipulator is made of at least three rotational joints therefore, for computing the kinematics, rotation matrices are needed: the most used are *Euler angles* and *quaternions*. Euler angles are those that provides three individual rotations around three axes. For three arbitrary zyx Euler angle rotations: ψ around the z-axis, then θ around the y-axis and finally ϕ around

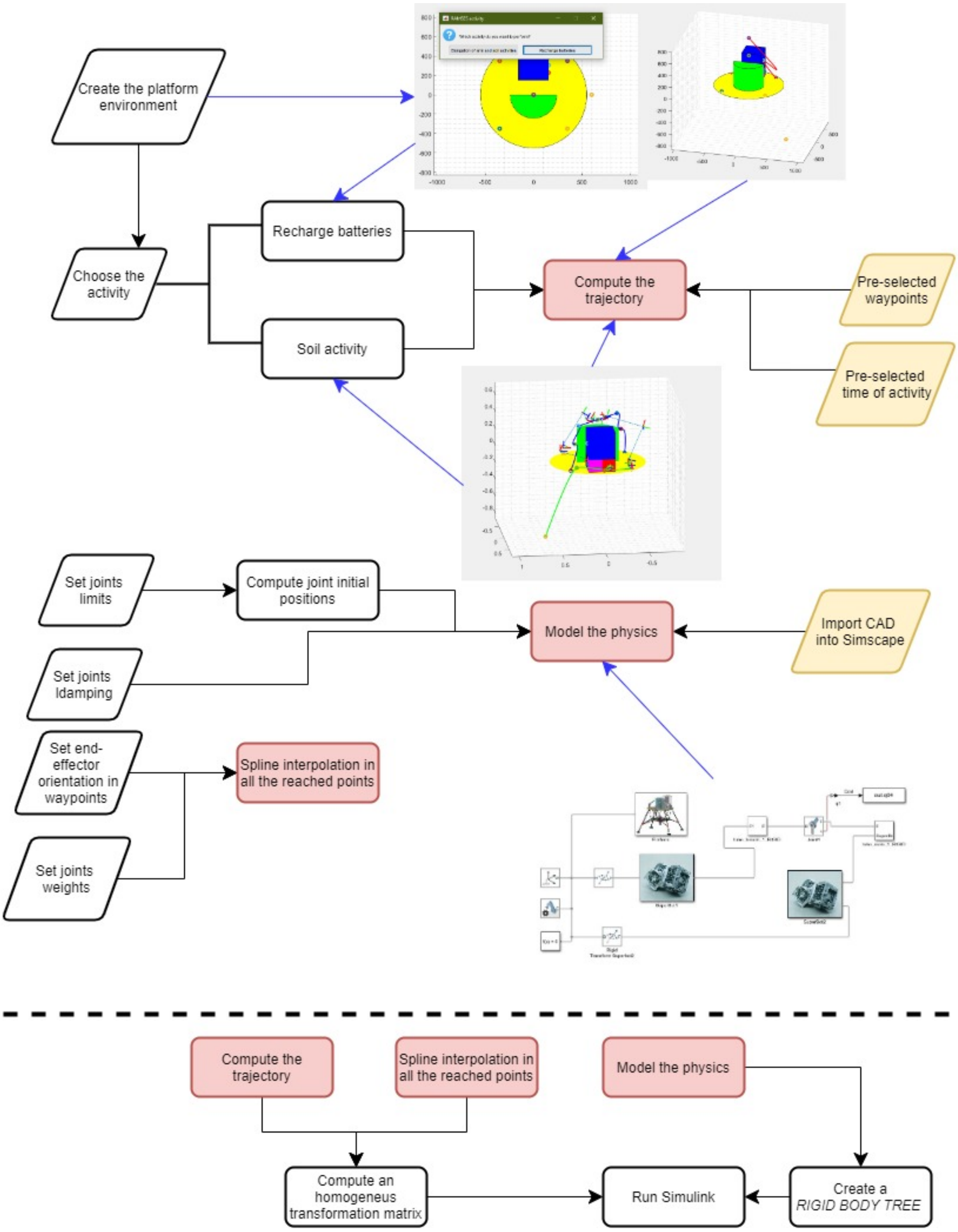

Figure 3.9: RAMSEs code architecture

the x-axis the rotation matrix is:

$$\mathbf{R} = \mathbf{R}_{z(\psi)}\mathbf{R}_{y(\theta)}\mathbf{R}_{x(\phi)} \tag{3.1}$$

Is useful to note that Euler angles are moving axes transforms that is, each rotation is around the new position of the axis after the previous rotation. It is also possible to define to define fixed axes rotations in which subsequent rotations are around the original axes of the coordinate system. Euler angles are inefficient to compute and suffer from computational instabilities which can be overcome with quaternions, wich are a generalization of complex numbers. In 3D a vector can be expressed as a *pure quaternion* with a null real component

$$p = 0 + x\mathbf{i} + y\mathbf{j} + z\mathbf{k} \tag{3.2}$$

Given an axis and an angle, there exists a quaternion q that rotates the vector around the axis by this angle using the formula qpq^{-1}. This computation is more efficient and robust than the equivalent computation with Euler angles which can suffer from singularities.

3.3.2 Matlab and Simulink© environments

In Figure 3.9 the code architecture is shown. It is based on the interface between Matlab, Simscape and Simulink. It is mainly divided into three parts:

1. Trajectory computation
2. Modelling of the RAMSEs physics
3. Simulink simulation

In the first phase, the code is asking which activity the user wants to perform. It is characterized by a visualization process to see which type of trajectory the manipulator has to follow. Firstly, there is the creation of the platform environment in a 3D-plot, then a pre-set of four points and the time dedicated for the whole activity are used to compute the trajectory with a cubic polynomial method. The chosen time for all activities is $150s$. In the second part, the LEAPFROG CAD is imported from SolidWorks into Simscape environment and by considering:

- joints limits
- the joints damping set at 0.2

the initial joint position is computed as a vector, where each row correspond to a revolute joint inclination in terms of angle. Moreover a matrix with the end-effector positions in space and orientations is created. The orientation of the end-effector pose is computed a priori with a spline interpolation. This is computed by considering four orientations in terms of angles in the pre-set waypoints. This is not the best way to do the analysis because is possible the end effector can reach all the points but not achieving the desired pose orientation: this problem does not occur in this code. Later, this matrix is converted into an homogeneous transformation matrix.

Before running the Simulink simulation, another step is done. The forward and inverse kinematics Simulink blocks need the creation of a rigid body called *Rigid Body*

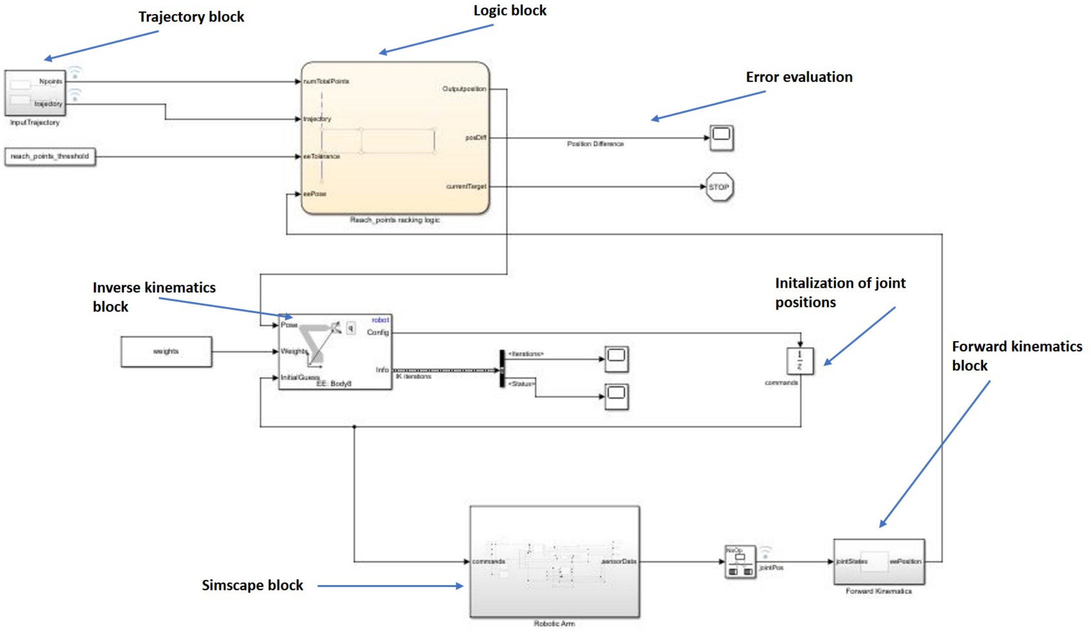

Figure 3.10: RAMSEs Simulink controller

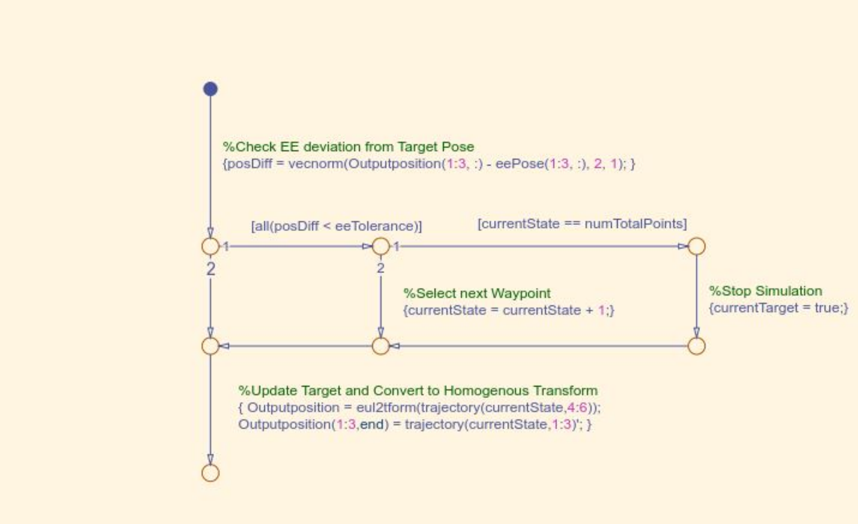
%Check EE deviation from Target Pose
{posDiff = vecnorm(Outputposition(1:3, :) - eePose(1:3, :), 2, 1); }

[all(posDiff < eeTolerance)]

[currentState == numTotalPoints]

%Select next Waypoint
{currentState = currentState + 1;}

%Stop Simulation
{currentTarget = true;}

%Update Target and Convert to Homogenous Transform
{ Outputposition = eul2tform(trajectory(currentState,4:6));
Outputposition(1:3,end) = trajectory(currentState,1:3)'; }

Figure 3.11: Simulink supervisory logic

Tree: it is basically a Matlab structure with all the robot information, such its inertia, its number of bodies, the gravity vector where the robot operates, the number of reference frames which correspond to the revolute joints reference of rotation. This is the reference frame with respect the selected joint is rotating. These reference frames should be computed considering the platform inertial frame.

Figure 3.10 illustrates the Simulink block diagram: from the top left, there is the trajectory matrix and a threshold computed a priori enter in the logic block. Is useful to note that the threshold is computed considering the maximum distance between two points from the interpolated points; they change depending on the activity chosen, since the trajectory is traded. The error evaluation depends upon the norm of the trajectory and the actual position of the end-effector and it considers also the desired orientation error. The simulation stops if the threshold is overcome. The logic operating is explained afterwards. The output position which is a 4x4 matrix enters in the pose port of the inverse kinematics block. Moreover, it is required to define a [1x6] vector of relative weights on the orientation and position error for the inverse kinematics solver. The first three elements of the vector correspond to the weights on the error in orientation for the desired pose. The last three elements of the vector correspond to the weights on the error in the xyz position for the desired pose. In the code weights is the following vector:

$$weights = [0.25\ 0.25\ 0.25\ 1\ 1\ 1]$$

The inverse kinematics block needs the initial joint position vector, which comes from the aforementioned Simscape physics modelling. The inverse kinematic solver is the Levenberg-Marquardt which results the best with a more than 6DOFs systems, because avoids redundancy. The initial pose vector is needed also for the Simscape block, where all the robot physics is modelled: here Simulink/Simscape converters are needed for the joints inputs (angular positions). After this block there is the forward kinematics one which computes the end-effector pose. This is a closed loop controller with an error evaluation.

In Figure 3.11 the supervisory logic is shown. By evaluating the norm between the desired position and the actual one, it can select the next waypoint to follow or can stop the simulation if the error is higher than the threshold. At every evaluation, the simulation state is updated.

Is important to note that the overall solver is the *ode45* with an automatic maximum step size.

3.4 Results

Here only two opposite situations are modelled: the manipulation of the OSP and the drill one. The first because is the only one which requires only half of the robotic arm. In Figure 3.12, Figure 3.13 and Figure 3.14 the sequence of the RAMSEs trajectory following is shown. The first is when the manipulator is still in its initial configuration, in the second one the extraction of the solar panel has already occurred, while in the third there is its deployment on the top of the platform. In Figure 3.15 each joints' total torque is provided for the whole manipulation time. Note that the additional torque provided by the panel has to be taken into account when the real prototype will be designed. Finally, in Figure 3.16 joints angular velocities are shown. Note that oscillations strictly depend upon the joint damping value, by the waypoints are created, because is useful to remember their trajectory computation depends upon the simulation time. In Figure 3.17, the error coming from the supervisory logic is computed for each iteration. The OSP dual situation is the drill manipulation. Here the RAMSEs is

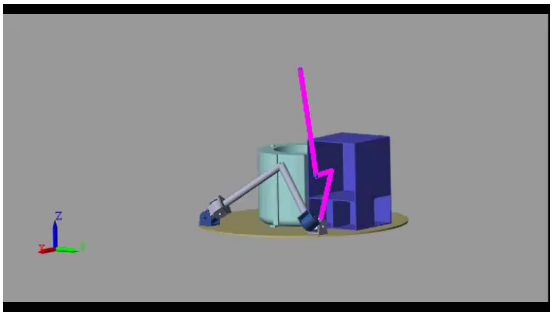

Figure 3.12: The RAMSEs trajectory following simulation when it handles the OSP

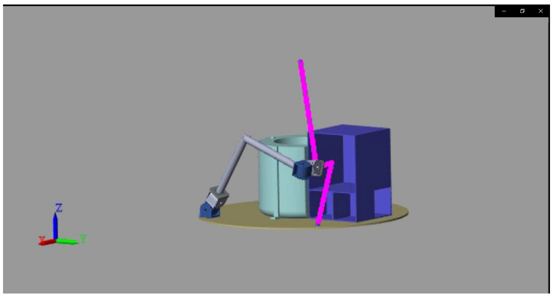

Figure 3.13: The RAMSEs trajectory following simulation when it handles the OSP

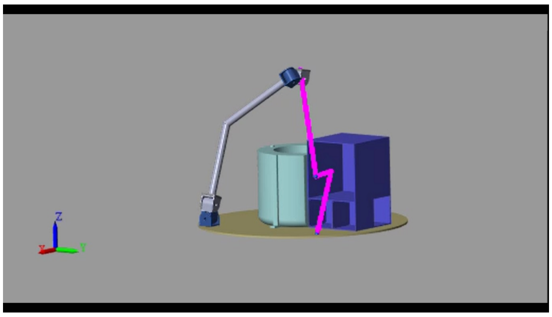

Figure 3.14: The RAMSEs trajectory following simulation when it handles the OSP

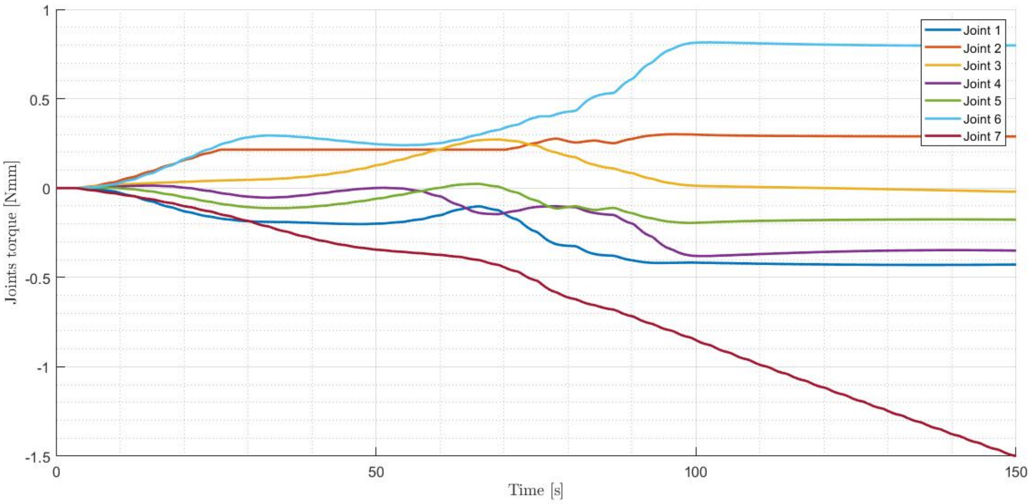

Figure 3.15: RAMSEs OSP manipulation joints torques

working with all the components, achieving 14 DOFs. Since the gripper point for the drill is the more distant with respect to the other tools, it represents the worse case

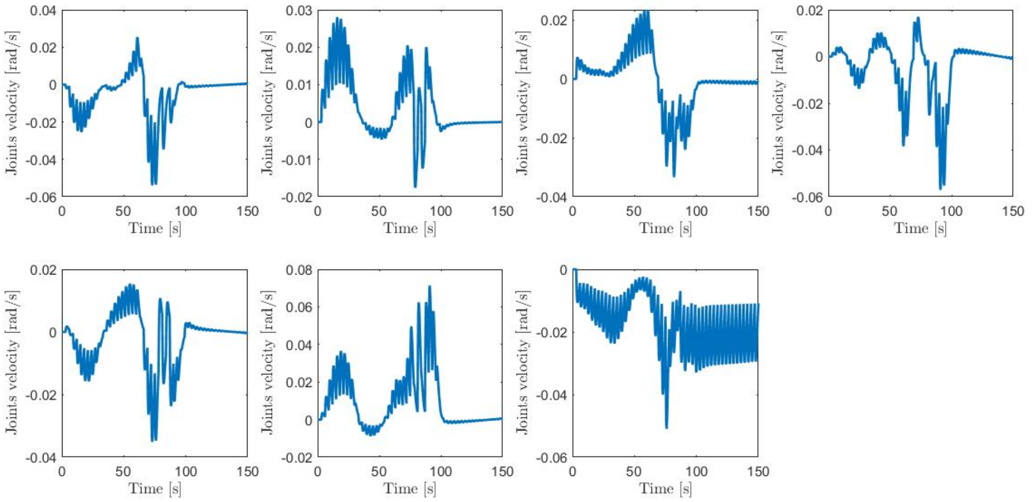

Figure 3.16: RAMSEs OSP manipulation joints velocities

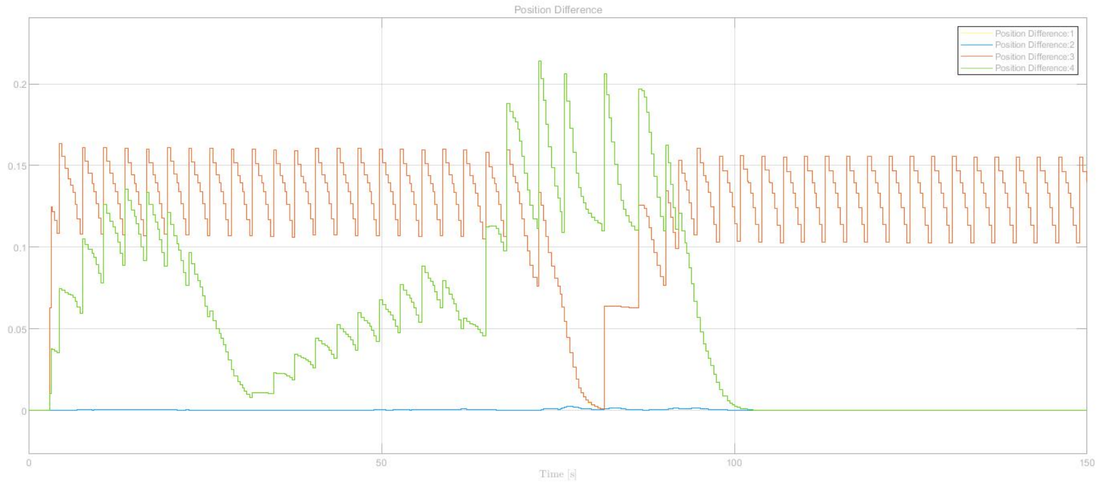

Figure 3.17: RAMSEs OSP error in performing end-effector position

scenario by the RAMSEs workspace. In Figure 3.18, Figure 3.19, Figure 3.20 the sequence of the RAMSEs movement is illustrated. Is important to note that is achieving all the prescribed points and it reaches the ground with the correct orientation. The only one drawback is that there is a little interference with the OSP box: but this does not represent a big issue since a suitable contained must be designed. Therefore, this represent a requirement to follow for the OSP box design.

In Figure 3.21 joints torques are shown. A big step can be seen around 80s: this because there is an higher error in performing the end-effector desired pose (Figure 3.23). Remember that this depends upon the mandatory orientation the manipulator has, which has to be better designed in this case scenario: a simple spline interpolation results in not the best option as results show. Finally the joints angular velocities are

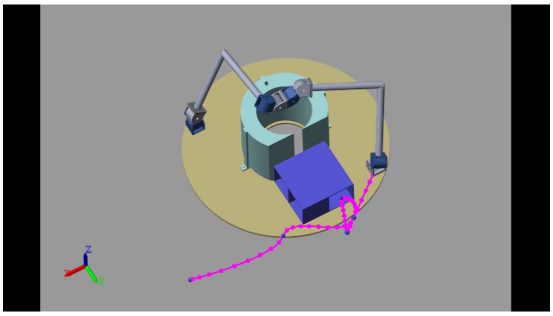

Figure 3.18: The RAMSEs trajectory following simulation when it handles the drill

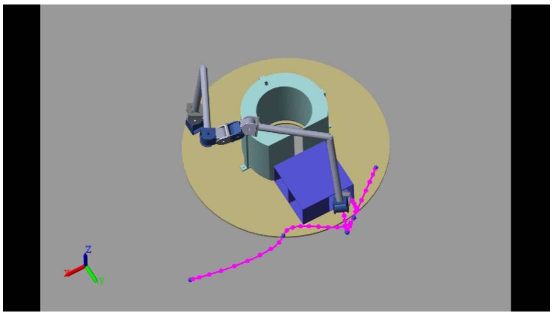

Figure 3.19: The RAMSEs trajectory following simulation when it handles the drill

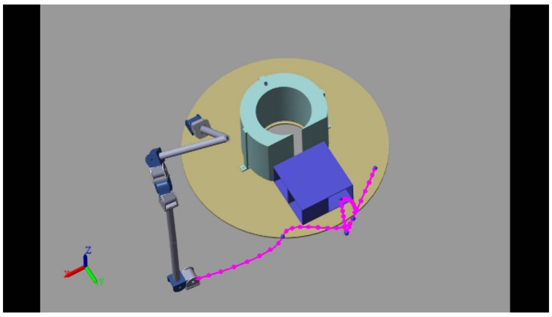

Figure 3.20: The RAMSEs trajectory following simulation when it handles the drill

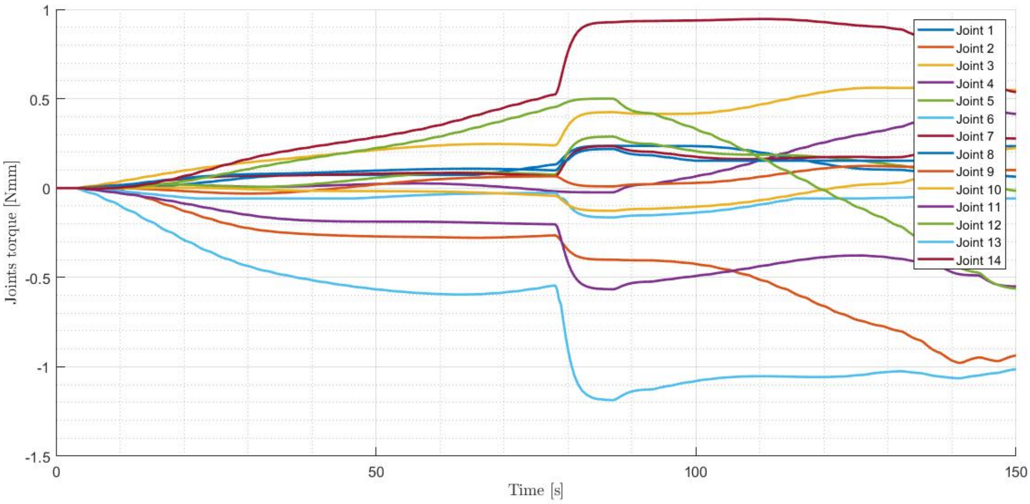

Figure 3.21: RAMSEs drill manipulation joints torques

shown in Figure 3.22. Here the same considerations for the OSP manipulation are valid.

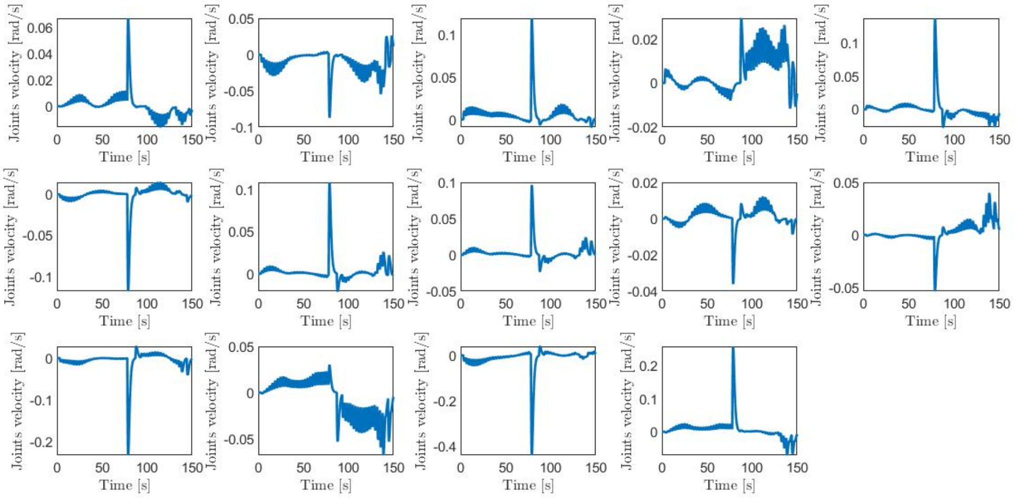

Figure 3.22: RAMSEs drill manipulation joints velocities

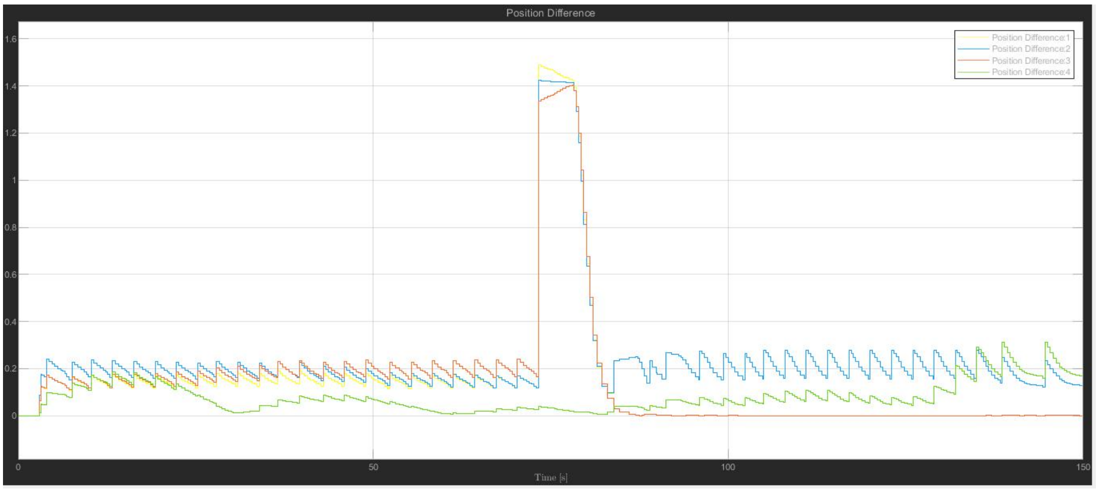

Figure 3.23: RAMSEs drill error in performing end-effector position and orientation

Chapter 4

Origami Solar Panel Design

Origami comes from the Japanese language and it means *the paper folding art* from *oru* to fold and *kami* paper. There are various types of folds, but in this thesis, only two of them will be considered in the design:

- *The valley - blue lines*: thanks to it, the observer is looking at a hollow
- *The mount - red lines*: thanks to it, the observer is looking at an edge

In the last decades, origami has been a subject of interest both for mathematicians and engineers.The former being mostly interested in the geometrical aspects (i.e., foldability of origami patterns and deployable structures),whereas engineers find that traditional geometry and paper model folding can be readily parameterized and utilised within new systems and devices development. In engineering applications, most applications are of rigid type compared to the paper; therefore, the rigid origami represents a physic subset that allows continuous motion between folded stated thanks to predetermined folding creases avoiding the twisting and stretching of the faces. Indeed, modern materials such as plastic, metal, or carbon fiber-sheets patterns can be readily manufactured, producing strong enough designs for large-scale applications.

4.1 Origami structures overview

When a membrane is biaxially folded, in-plane deformations occur and their intensity also depends on the type of one-dimensional or two-dimensional folding processes. Moreover, stress and fracture caused by folding must also be taken into account: they are more concentrated at the node where more than two folds cross each other (Figure 4.1, Orthogonal Folding). Mainly, maximum tensile stress is produced on the fold's outer surface (a), perpendicularly to it: the stress is higher if the thickness is larger due to its proportionality and smaller if the curvature is reducing. When a second fold (b) is made perpendicularly to the previous one, additional tensile stress is produced on the outer surface of the point of intersection (c), causing breaks. The solution is the so-called isometric transformation, given thanks to a plane regularly folded into smaller planes. Additionally, space structures must satisfy the following conditions:

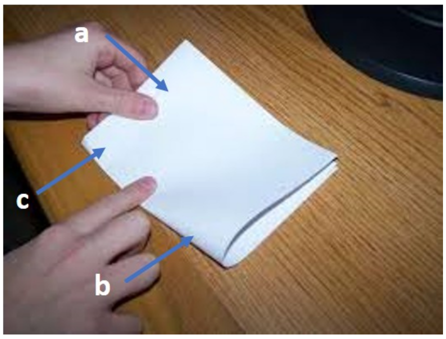

Figure 4.1: Deformations in a sheet node

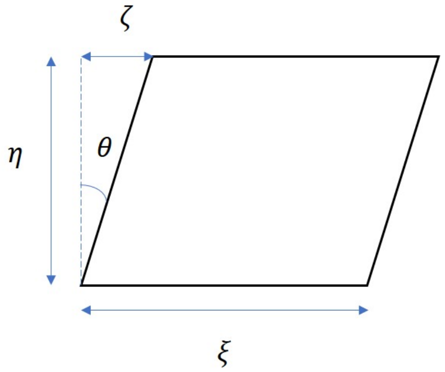

Figure 4.2: Parallelogram element whose tessellation composes fold lines of two-dimensional folding by DDC surface

- Isometric condition must be held unchanged during the process
- Fold line is to be two-dimensional tessellation of a plane
- Folding/Deployment process must be complete into a fundamental region
- Deploying process is to be a simple, continuous movement.

Given these requirements, plane folding is treated as an analytical problem described by partial equations [48]. The Developable Double Corrugation (DDC) solves the problems mentioned above since this surface is obtained by the contraction of a plane in two orthogonal directions (Figure 4.2). The result is a DDC surface consisting of several congruent parallelograms adjacent to each other. If an ideal paper of negligible thickness is assumed and folded up infinitesimally closely, it is folded up to a point: this is congruent to transforming a plane into a point. Moreover, contractions are in two mutually perpendicular directions and are dependent contrarily to the orthogonal folding. Whenever a deformation occurs in a region, by making the fold angle θ sharper, the adjacent fundamental region undergoes an identical deformation, which will produce a domino effect to the nearer region. The paper behaves as if it has a built-in linkage mechanism to fold or deploy. This helps reduce the stress, as mentioned earlier, by a significant margin.

The design of a suitable region pattern is challenging and different studies on topology optimization are undertaken [49]. The most used process is the assignment of different folds or *lines* in a *ground structure* by using folding angles as a design variable; then a 3D geometry of the folded sheet can be computed using the origami mathematics. A topology optimization method is then used to find an optimal combination of folding angles, which results in a folding pattern with desired, target geometric properties.

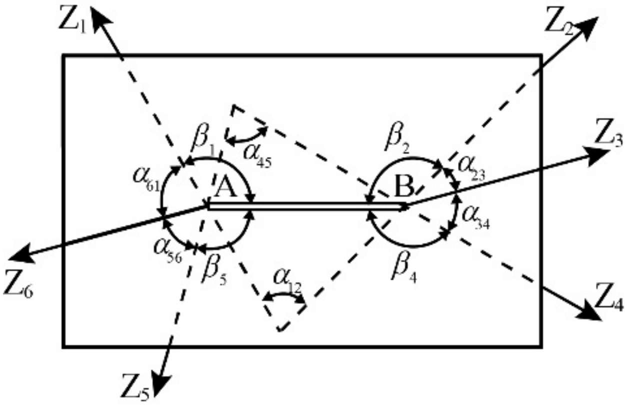

Figure 4.3: The zero-thickness kirigami pattern

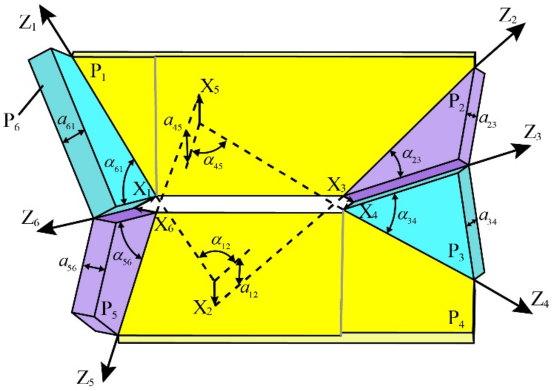

Figure 4.4: Thick kirigami pattern

4.1.1 Addressed issues

In the space sector, it is impossible to produce negligible thickness structures and until now, everything has been considered an origami with a quasi-zero width. Different methods have been proposed over time to address the thickness issue, for example, the axis-shift method [50], the offset panel technique [51], the spatial mechanism approach [52], the doubling creases method [53] and the utilization of complaint mechanism [54]: however, they have limitations including the surface trimming requirement that causes a non perfect flat ground structure, or widened and flexible creases. Moreover, there is the requirement of a ground surface in space applications without any gaps between the fundamental regions due to line hinges: this is the perfect example for a solar panel. In this context, the *kirigami* can avoid such restrictions.

The kirigami is a variant of an origami where a hole or a cut between two fundamental regions is present. In Figure 4.3 and Figure 4.4 two different kirigami with a rectangular-shaped hole are proposed: the first has no thickness while the second does. In the first case, the fold lines have directions that merge in two points, creating the angles α_{45} and α_{12} while in the second figure, there is not this phenomenon and other hinges are placed either on the top or on the bottom surface of facets. If the thick kirigami will be folded it is a $6R$ Waldron hybrid spatial linkage where R are rotational joints with axis as $Z_1 - Z_6$, obtaining the kinematic equivalence of the zero-thickness panel as shown in the demonstration in [55], therefore the thick panel folds exactly as the paper-like sheet. The weak point is the mount or valley assignments that are settled a priori to the physical models' construction and can not switch on each other.

This has been occurring since the self-folding robot era [56]. These objects are capable to switch from a mount to a valley from the same folding line thanks to their ability to be self-reconfigurable and versatile. A key limitation is the deformation or flexibility of hinges as well as the torque peak. Robotic systems with an insufficient torque could lead to transformation failures and inaccurate movements, but torque minimization algorithm analyzes this problem, minimizing robot inertia [57]. Many

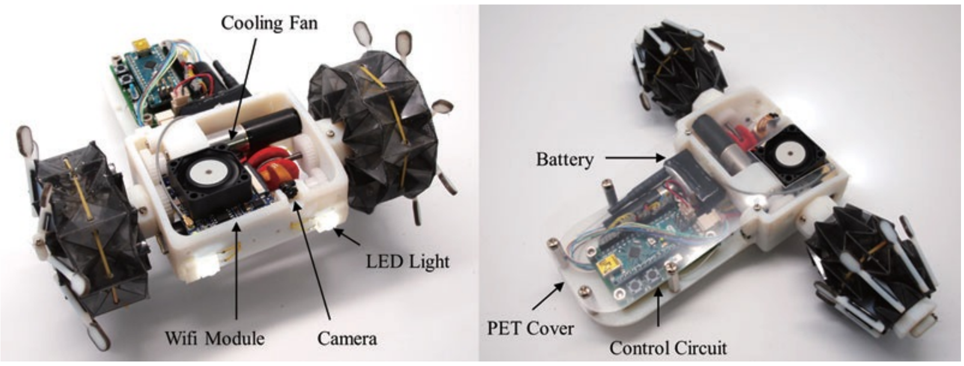

Figure 4.5: Variable-diameter wheel drive robot [7]

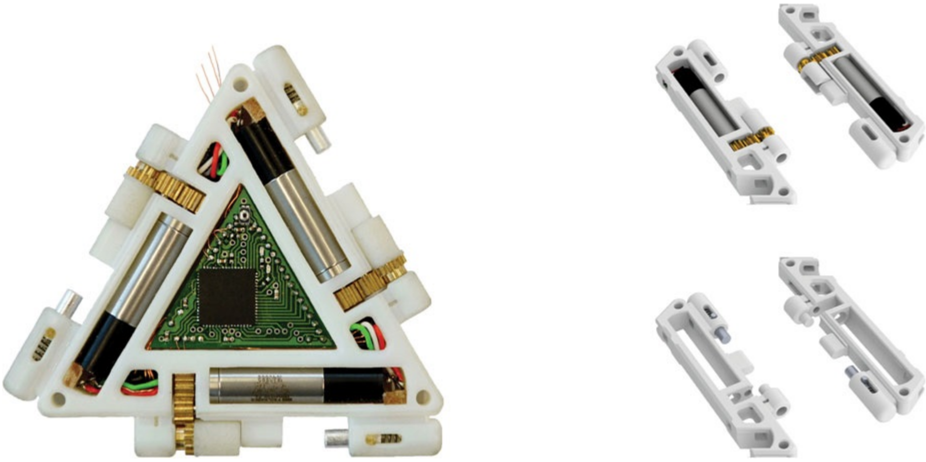

Figure 4.6: Mori prototype [8]

types of origami-inspired robot have been designed and realized [58]. Robots are assembled conventionally with a multiple low-level steps, while in nature there are system which achieve complex shapes thanks also to the folding process (i.e., such proteins, flowers etc.). Being inspired by nature, the design and fabrication of origami robots exploits top-down, parallel transformation approaches to achieve elegant designs and complex functionalities. This is achievable also thanks to not only smart type of actuation and fabrication, but also to smart and soft materials. Moreover, they can be easily realized thanks to the 3D-printing prototypes techniques which can exploit complex geometries with high availability. However, they are limited to one or two materials and they cannot be integrated with active components. Printable robots deals with this limitation taking advantage of available planar fabrication methods and electromechanical laminates that are subsequently folded into functional 3-D machines employing origami-inspired techniques [59]. An example is the variable-diameter wheel drive robot [7] which is able to pass over high steps as well as narrow gaps thanks to the soft-robotics design approach avoiding complex mechanichal parts and complex assembly process (Figure 4.5).

The high inspirational technology for the purposes of this thesis is the *MORI: a*

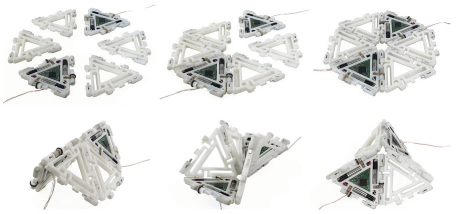

Figure 4.7: Different Mori configurations [8]

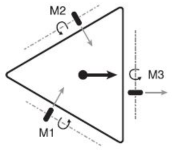

Figure 4.8: Mori gears rotation axis [8]

modular origami robot [8] a 3D-printed modular robot able to reconfigure itself which combines a quasi-two dimensional lattice type configuration [60] and the origami-based structure. The ground structure is built by a series of triangles: the use of equilateral triangles reduces complexity and augments degrees of reconfigurability (Figure 4.7). Moreover, it has on-board control, actuation and sensor integration and its main structure is 3-D printed (Figure 4.6). As a low profile is desirable in origami robots to allow for a maximum folding angle, component selection focuses on minimizing the overall thickness of the robot. The actuation is provided by a stepper motor fixed parallel to the engagement axis on which, a planetary gear-head is settled to reduce the step size. Subsequently, a series of spur gears are installed to translate the actuation to the engagement axis. A u-shaped pivot is attached to the last gear, forming the active part of the actuation system. The engagement mechanism is manual and done by a spring. Modularity, mobility and versatility characteristics are then analyzed in the aforementioned article [8].

4.2 Requirements

The OSP requirements are stated in Table 4.1. They are for both for the Power Distribution and Control Unit, as well as for the structure,but only the preliminary design for the structural part is here by proposed.

4.3 Structure preliminary design

Since the OSP has to be realized in SERC laboratories, as stated in Table 4.1, the advantages of using the reconfigurable soft-robotics cannot be exploited due to the technology's high-difficult implementation and hardware. Since the OSP structure contains the solar cells, the electronics, the power-management and the mechanical deployment hardware, a considerable width must be taken into account. Therefore, the already mentioned theory regarding thick panels is considered to do the ground structure trade-off analysis.

By exploiting the symmetry properties of an origami structure [55], the following

ID	Name	Requirement Statement
R-HLR-01	Power	The OSP shall provide enough power to fully charge on-board batteries
R-HLR-02	RAMSEs	The structure should be grabbed by the RAMSEs
R-HLR-03	Realization	The system should be fully built in SERC laboratories
R-DSR-01	DOFs	The structure should avoid torque and stress transmission on solar panels
R-DSR-02	COTS	The system should be built by using COTS
R-FNR-01	Unfolding	The deployment should be mechanical

Table 4.1: OSP Systems Requirements

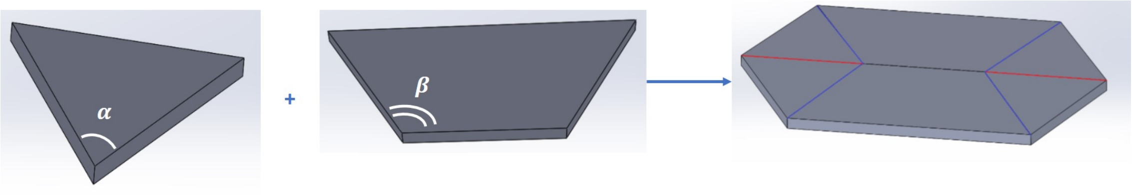

Figure 4.9: First OSP proposal

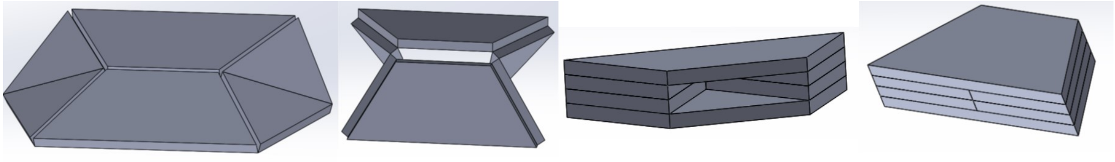

Figure 4.10: First OSP proposal folding procedure

relation of folding angles must be satisfied:

$$n\alpha + m\beta = 360^\circ \tag{4.1}$$

where n and m are the number of congruent adjacent regions. Three uncomplicated patterns have been analyzed thanks to panels with a simple geometry of a fixed thickness t with the software SolidWorks-2019 shown in Figure 4.9, Figure4.11 and Figure 4.13: the mounts are represented in red and are placed on the top surface edge; contrarily, the valleys are in blue and on the bottom edge. A summary Table 4.2 lists all the technical properties of the three configurations. In Figure 4.10, Figure4.12 and

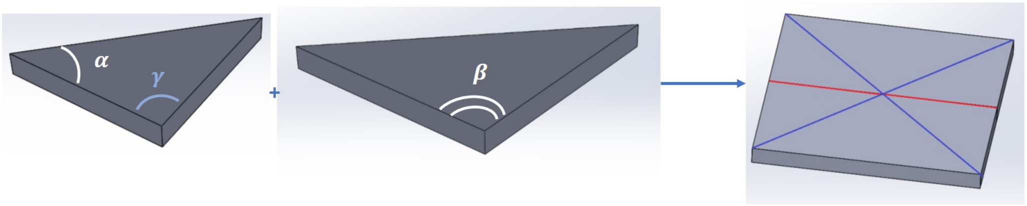

Figure 4.11: Second OSP proposal

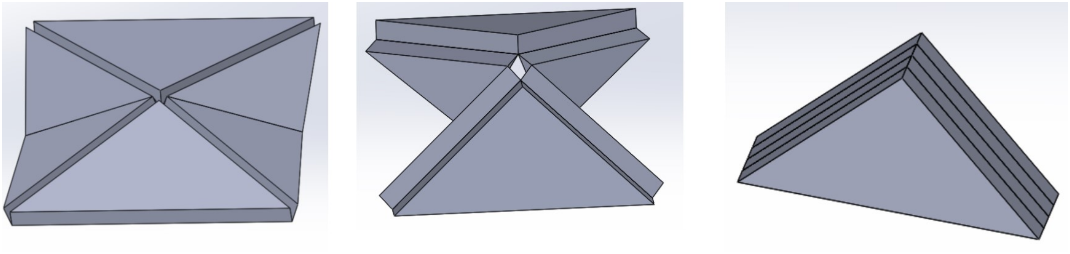

Figure 4.12: Second OSP proposal folding procedure

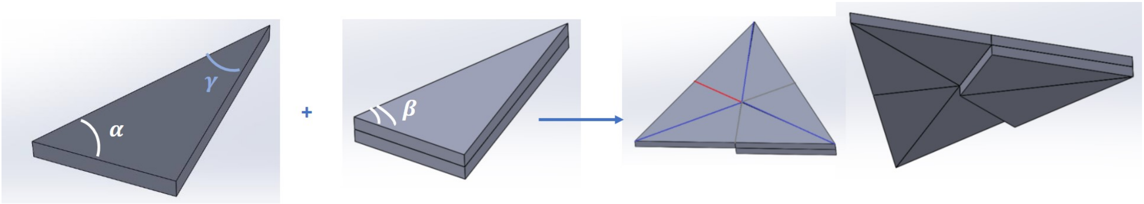

Figure 4.13: Third OSP proposal

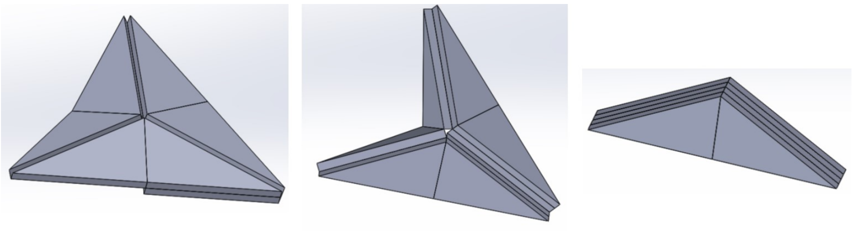

Figure 4.14: Third OSP proposal folding procedure

Figure 4.14 proposals' folding process is then shown.
Is important to note that:

- The hinge line (mount or valley independently) is coincident with the conjunction edge of two adjacent regions and along this line they always remain attached to each other
- Mounts and valleys are not interchangeable
- Mounts or valleys cannot become inactive lines (with any rotation)

Therefore, all proposals have only one DOF and only one actuator is needed for the folding and deployment procedures. The selected configuration is the **second** one

Proposal	**Type**	α [°]	n	β [°]	m	γ [°]	**Panels Shape**
First	Kirigami	60	2	120	2	60	Equilateral triangle and isosceles trapezoid
Second	Origami	45	4	90	2	45	Isosceles triangle and double size isosceles triangle
Third	Origami	60	4	60	2	30	Right triangle and double *t* right triangle

Table 4.2: OSP Proposals Properties

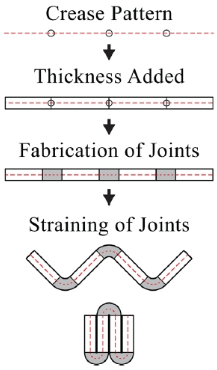

Figure 4.15: In-plane hinge lines and possible joints

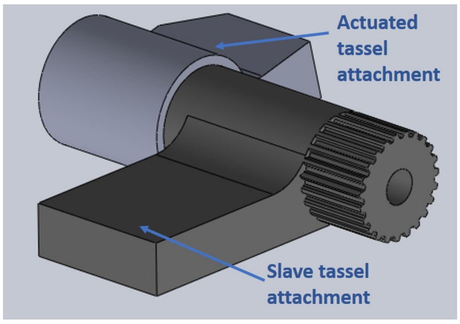

Figure 4.16: OSP Main hinge proposal

(Figure 4.11 and Figure 4.12) for symmetry reasons and its center of mass position which is significant to be considered since RAMSEs handles this panel. To find the OSP final and correct dimensions, the starting point is the hardware choice, like the solar cells type, its efficiency by the power viewpoint, and the type of actuator and its dimensions for the folding/unfolding viewpoint. For the correct actuation, it is essential to consider that a rotary actuator is the best choice since this is not causing the mutual displacement between two adjacent regions, as could occur with the linear actuator; moreover, regions are rotating one over the other. To design a suitable structure, the power distribution from solar cells and the Electric Power Unit (EPU) has to be considered; hence, holes for wiring between all regions have to be present. Moreover, the solar cells region has to be flat: the OSP is held by the RAMSEs and is capable of orientating the panel anytime perpendicularly to the Sun rays direction, achieving the highest radiation. Therefore, any gimbal actuator is needed for the robotic arm interface.

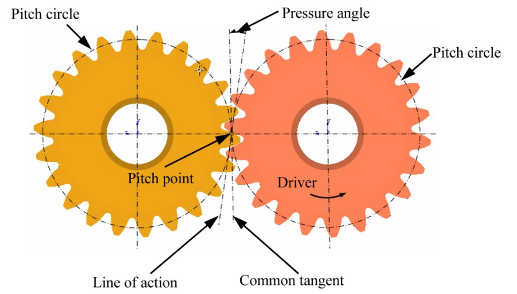

Figure 4.17: Gear teeth representation

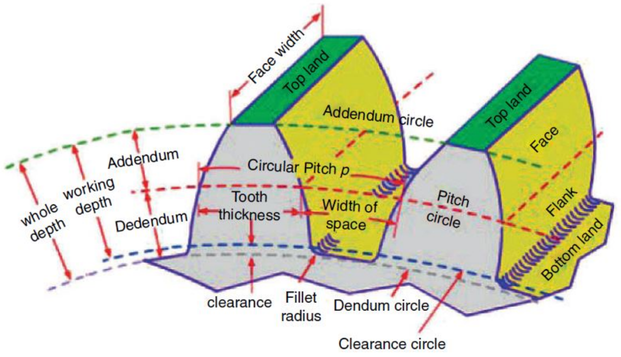

Figure 4.18: Pair of mating gears

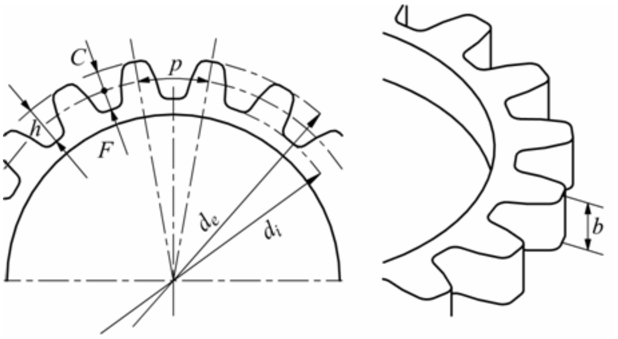

Figure 4.19: Gear parameters

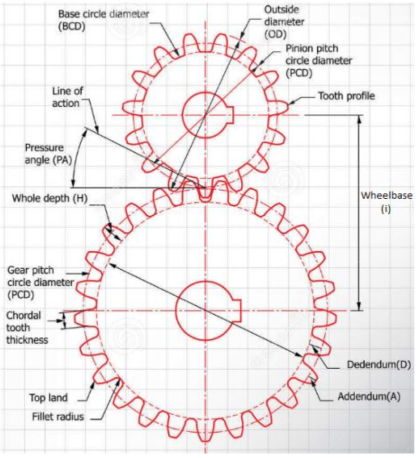

Figure 4.20: Gear parameters

The challenging part to design is the rotation transmission from the rotary actuator axes to the hinge line. For this objective, *MORI* origami blends the main inspiration and its drawbacks are deeply analyzed to satisfy all the requirements. *MORI* has the hinge lines lying down in the triangle middle plane causing a non compact folded shape like the OSP chosen configuration must reach. This could be solved by straining joints (Figure 4.15)transferring the rotation with gears: the first solution is not the best in terms of flexibility, causing a concentration of tensile stress when the panel is fully deployed giving a result that is not perfectly flat. Therefore, the most suitable choice for this project is the gears use as the *MORI*. To solve the *MORI* in-plane rotation problem, a hinge, which connects two regions (*Tassels*) with a gear at the end is here proposed, as it could be easily printed and fixed to its tassel (Figure 4.16). This hinge is made of two different coaxial bodies: one is attached to the actuated tassel and the other one to the adjacent tassel; note that the rotation axes coincides with the valley line. Therefore the tassel shape has to consider these hinge dimensions to bypass interference. Last part of the design is the gears number and dimensions, but before introducing all the calculation needed, a brief introduction of the design process is presented. Gear properties and definitions are listed in the Glossary 1 and shown in

Figure 4.17, Figure 4.18, Figure 4.19 and Figure 4.20. Here below basic gear relations are described:

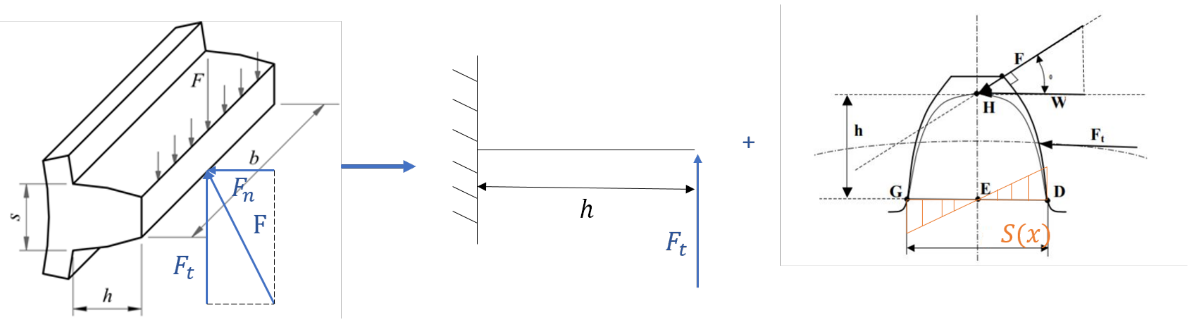

Figure 4.21: Lewis Method sketch

- Pressure angle (θ): is defined a priori, here considered as 20°
- Transmission ratio: the modulus between two gears is equal. Then

$$\tau = \frac{d_{p2}}{d_{p1}} = \frac{z_2}{z_1}$$

- Number of teeth: to avoid interference and to guarantee a perfect meshing

$$z = \frac{2(\sqrt{sin^2\theta\tau(\tau+2)+1}+1)}{sin^2\theta(\tau+2)}$$

- Primitive diameter: is that one of the circumpherence where there is the teeth contact

$$d_p = \frac{zm_n}{cos\beta_g}$$

  where β_g is zero for a spur gear and m_n is the modulus.

- Resultant torque on the slave gear C_2

$$C_r = C_1 \cdot \tau$$

- Clearance diameter: important for the evolving profile gear which is that one here proposed

$$d_b = d_p cos\theta$$

- Addendum diameter: limits the top tooth

$$d_a = d_p + h_a = d_p + m_n$$

- Dendum diameter: limits the bottom tooth

$$d_f = d_p - 1.25m_n$$

- Tooth width: depends upon the arbitrary gear slenderness λ

$$b = \lambda m_n$$

- Chosen evolving profile parametric equation:

$$\begin{cases} x = 3(cost + tsint) \\ y = 3(sint - tcost) \end{cases}$$

  where the parameters are $t_1 = 0$ and $t_2 = 0.2\pi$

For this OSP only spur gears are considered. This design is done taking into account a static sizing and a flexural solicitation [61] thanks to the *Lewis Method*. The tooth is considered as a fixed beam on the base circle diameter with a total force F acting on it. Lewis hypothesis are:

- The worse case scenario is to have in contact only two teeth from the driven and slave gears
- The only one force considered is the tangential component T_f of the force
- Any compression contribution F_n is considered

The maximum normal stress is constant and its value is:

$$\sigma_{max} = \frac{6F_t x}{bS(x)^2} = const \tag{4.2}$$

Hence

$$S(x)^2 = y^2 = \frac{F_t x}{6\sigma_{max} b} \tag{4.3}$$

The area with the maximum solicitation is the G-D from Figure 4.21 and:

$$\sigma_{lewis} = \frac{F_t}{bm_n} y_{lewis} \tag{4.4}$$

where y_{lewis} is a tabulated value which depends upon the number of teeth and the pressure angle. The modulus can be computed as:

$$m_n = \sqrt[3]{\frac{2C_1 cos\beta_g y_{lewis}}{\sigma_{amm}\lambda z}} \tag{4.5}$$

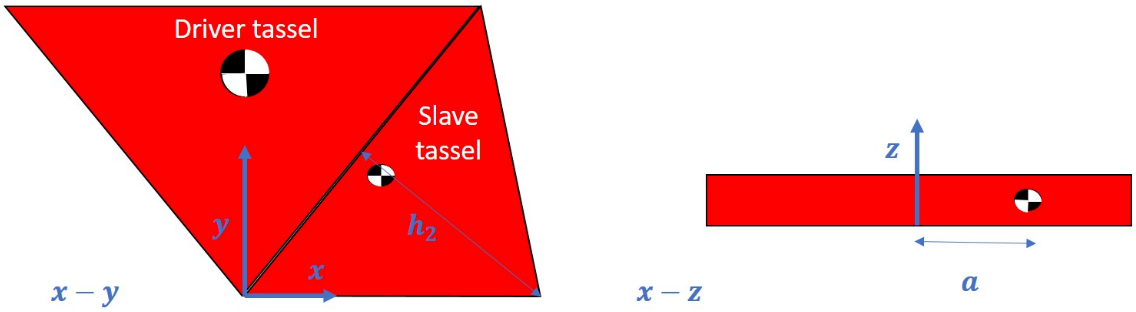

Figure 4.22: Resistant toque geometric scheme

where σ_{amm} is the maximum admissible flexural strenght of the chosen material and the following relation must be satisfied:

$$\sigma_{lewis} \leq \sigma_{amm} \tag{4.6}$$

Tassels mass and geometry are important to define the total number of gears needed to counteract the weight coming from the slave tassels and to fulfill a complete panel deployment. In this way, it is possible to find the resistant torque which is related to the gears transmission ratio. If, with only two wheels, the number of teeth, then the gear dimension, is too high causing an increase of the solar panel width, the gears total number will be augmented.

To validate the gears design, the last gear exit torque should be greater than the resistant due to the weight. To consider the worst case scenario, the total slave tassels weight is considered in the adjacent tassel from the driver one: in this way the arm is greater than the real. The arm is computed from the hinge line, since it has to coincide with the last gear rotation axes.

$$a = \frac{h_2}{3} \tag{4.7}$$

Moreover, some inputs are required, such the stepper motor torque (T), its tree radius (r_{tree}) as well as some guesses, which could be modified a posteriori, for instance the pressure angle (θ), the tassels total mass, geometric characteristics and the transmission ratio of the first gear.

4.4 Origami Solar Panel architecture

In Figure 4.23 the whole OSP architecture is presented: a net separation between mechanical movement management and the Power Distribution Control Unit is proposed in order to prevent a high combination of failure modes.

The tassels are the red rectangles, which have solar panels inside, and they are connected together through hinges and gears. The system has 1 DOF and only a stepper motor is needed: to better control it a sensor as well as a controller and a motor driver required. Note that the EPU is powering the controller and the motor driver. Gears are needed only between the active tassel and the adjacent one, while others can only be connected through simple hinges.

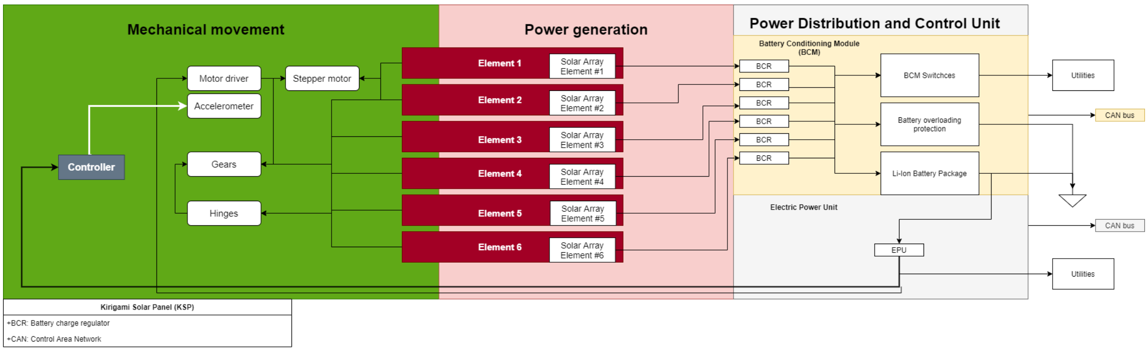

Figure 4.23: OSP System Architecture

4.5 Test-bed description

To prove this design a littler test-bed is here proposed: the chosen hardware is listed here below.

- Stepper motor: PG20L-D20-HHC0 from NMB-MAT with technical properties listed in Appendix A
- Motor driver: The DRV8835 Dual Motor Driver Carrier can deliver 1.2 A per channel continuously (1.5 A peak) to a pair of DC motors, and it supports two possible control interfaces for added flexibility of use IN/IN and PHASE/ENABLE. With an operating voltage range from 0 V to 11 V and built-in protection against reverse-voltage, under-voltage, over-current, and over-temperature, this driver is a great solution for powering up to two small, low-voltage motors. The carrier board has the form factor of a 14-pin DIP package, which makes it easy to use with standard solder less breadboards and $0.1in$ perfboards (Figure A.8)
- Controller: Arduino Mega (Figure A.9) with the following characteristics
    1. The operating voltage of this micro-controller is 5V
    2. The recommended Input Voltage will range from 7V to 12V
    3. The input voltage will range from 6V to 20V
    4. The digital input/output pins are 54 where 15 of these pins will supply PWM o/p
    5. Analog Input Pins are 16
    6. DC Current for each input/output pin is 40 mA
    7. DC Current used for 3.3V Pin is 50 mA

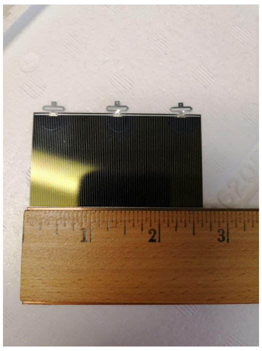

Figure 4.24: OSP solar cells

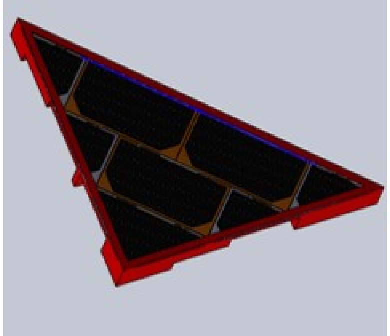

Figure 4.25: Actuated tassel

Figure 4.26: First gear

8. Flash Memory like 256 KB where 8 KB of flash memory is used with the help of bootloader
9. The static random access memory (SRAM) is 8 KB
10. The electrically erasable programmable read-only memory (EEPROM) is 4 KB
11. The clock (CLK) speed is 16 MHz
12. The USB host chip used in this is MAX3421E
13. The length of this board is 101.52 mm, the width is 53.3 mm, the weight is 36 g

- Uxcell Single-Sided Copper Clad Laminate PCB Circuit Board for the solar panel integration on the structure
- Low efficiency solar cells (Figure 4.24)
- Stratasys ABSplus-P430 Cartridge White (56.3 ci/923 cc) for the tassels print
- P400-SC Soluble Concentrate for the support printing material
- Red MAKERBOT PLA for the hinges, pins and gears prints

The OSP design starts considering material properties, the torque and dimensions of the chosen stepper motor and the tassels geometry. By following the gear procedure explained before, three gears are needed to transfer the rotation up to the hinge line and to counteract the resistant torque coming from the panel inertia. The first gear is directly attached to the stepper motor (Figure 4.26), the second gear rotates with respect to a pin, fixed inside the driven tassel (Figure 4.27) and transfers the rotation to the third gear, called *Main Hinge*. This has a geared hinge attached to the slave tassel and another fixed coaxial body attached to the driven tassel. The pitch circles of the first two gears are on the same z plane height, while the third is tilted of 30 °to making the rotation axis coincident to the valley.

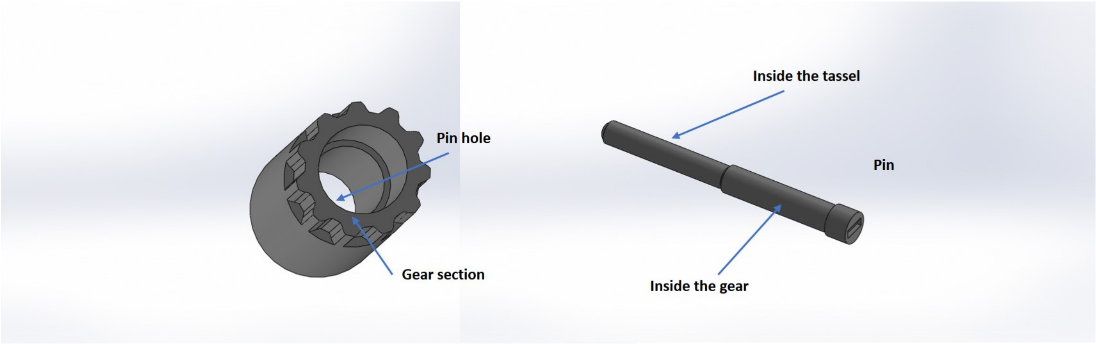

Figure 4.27: Second gear and pin

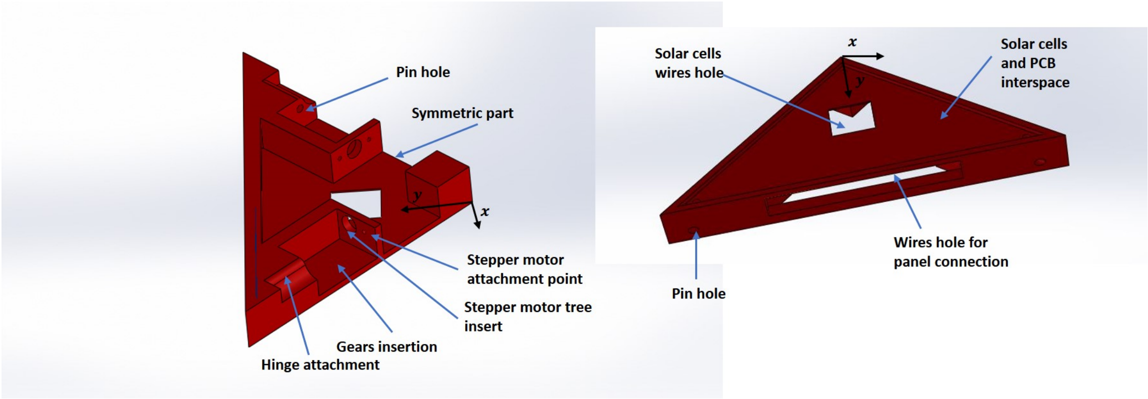

Figure 4.28: Actuated tassel characteristics

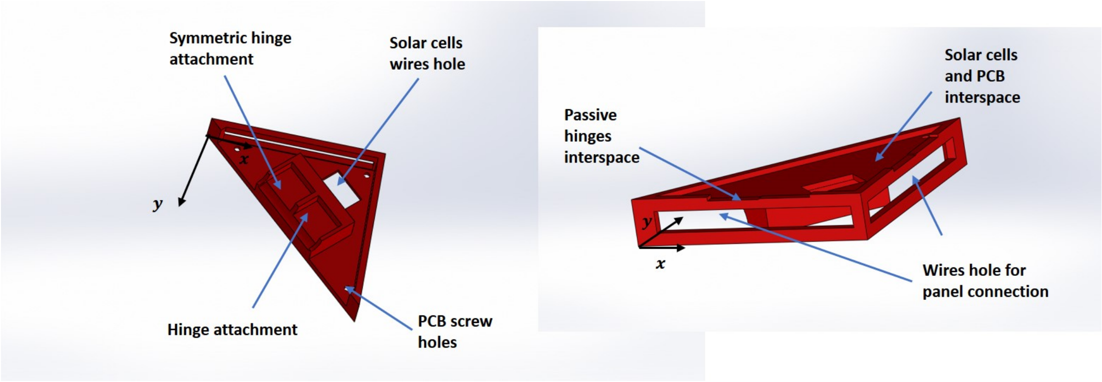

Figure 4.29: Slave tassel characteristics

The driven tassel satisfies all requirements and permits an easy assembling of all the elements since it has holes for the stepper motor tree, its screws to fix it, the gears locus, the main hinge fastening and for the wiring from the solar panel location to other tassels (Figure 4.28). The slave tassel indeed has the main hinge attachment region as well as solar cell dedicated holes (Figure 4.29). The OSP driven and slave adjacent assembly is shown in Figure 4.30. Other tassels are connected to each other

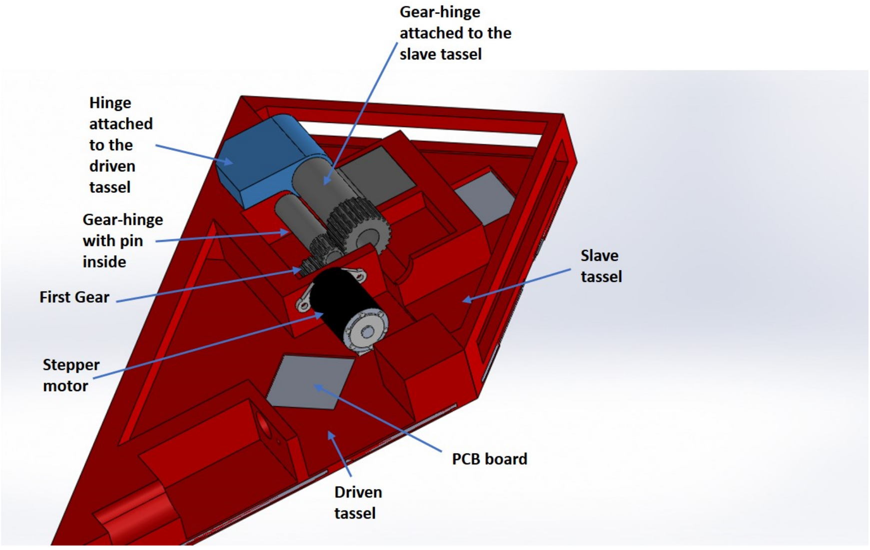

Figure 4.30: OSP driven and slave adjacent tassels

only by main hinges in the valleys and smaller simple hinges on the mounts which has a dedicated space to avoid interference in the folded configuration (Figure 4.31 and Figure 4.32).

Hinges and gears are printed with the MakerBot Replicator PABH65 printer with PLA material, an infill density of 21% and five number of shells: this will help to provide a cleaner print especially due to the small size of gear teeth and to gain an high accuracy ($\pm 0.2mm$), escaping gears interference (Figure 4.33). Indeed tassels are printed with the Dimension Elite, BST1200es printer with ABS-P430 material, which guarantees a better accuracy compared to the PLA printing, since tassels have full of details of ($\pm 0.05mm$) accuracy. All components are then screwed together instead of being epoxed as personally requested by the co-advisor (Figure 4.36), with the exception of the mounts smaller hinges which are just fixed with a nylon pin (Figure 4.35). Lastly, only the pin is epoxed inside the tassel. In Figure 4.37 the OSP test-bed assembly can be seen, with the stepper motor fixed. Due to Covid-19, the research was curtailed one month before the planned date. Therefore the test-bed could not be integrated with the electronics and only a manual test was done, which anyway proofs the concept and the design. The overall mass is 1.5 kg.

Tables which summarize panels dimensions and costs are here reported:

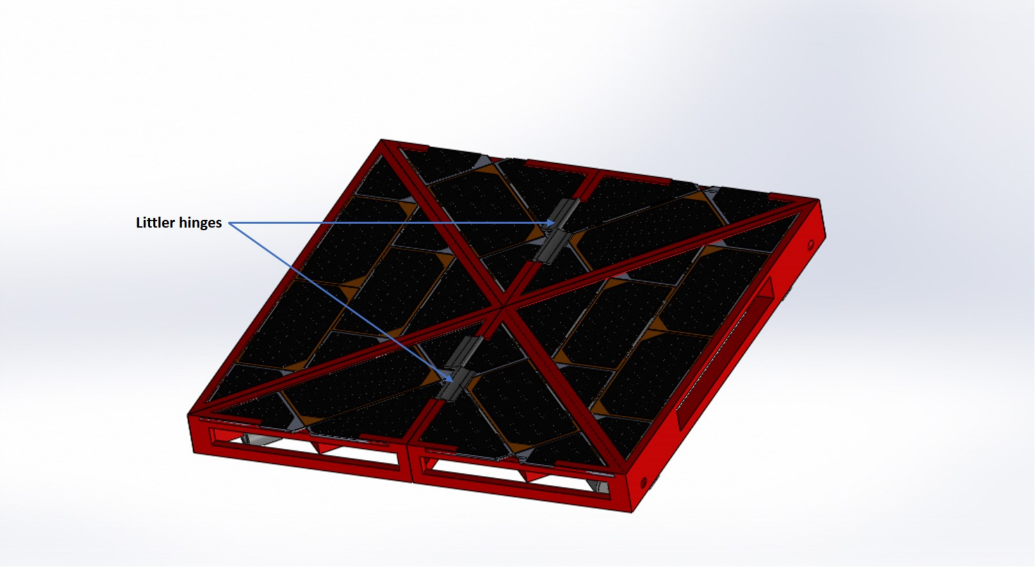

Figure 4.31: OSP fully assembled

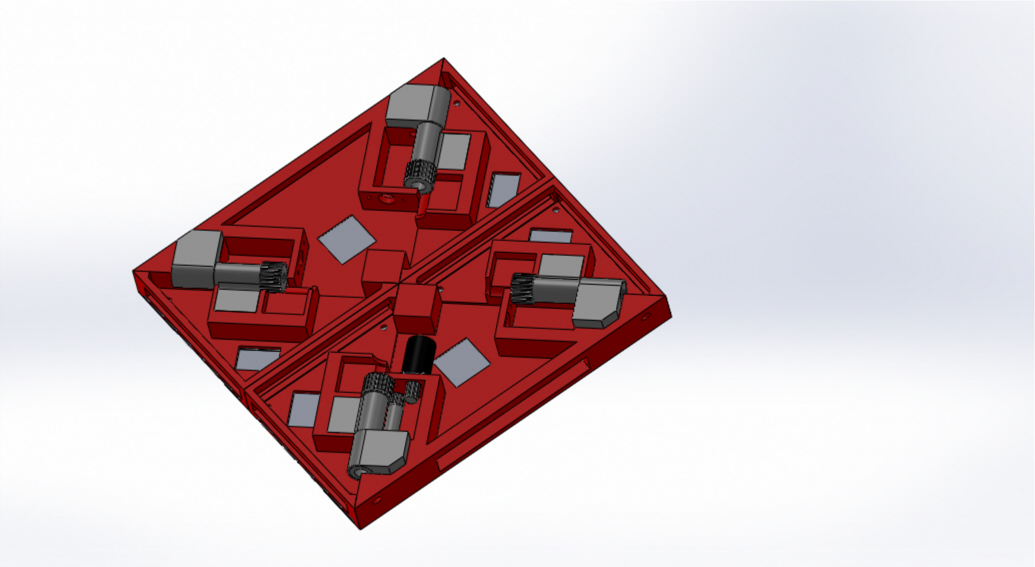

Figure 4.32: OSP bottom fully assembled

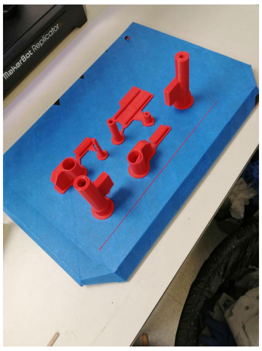

Figure 4.33: Hinges and gears just after the print session

Figure 4.34: Big tassels just after the print session

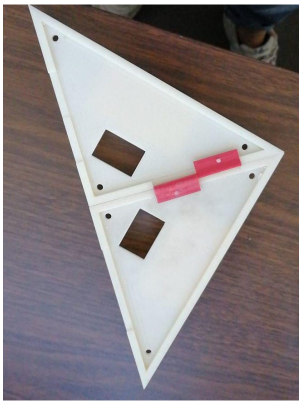

Figure 4.35: Smaller hinges with nylon pin

Figure 4.36: Hinges are screwed in tassel

Name	**Cost [$]**
Motor driver	3.89
Controller	24.7
Stepper Motor	36.25
ABS-P430	30
PLA	5
Total	99.84

Table 4.3: OSP Test-bed realization cost

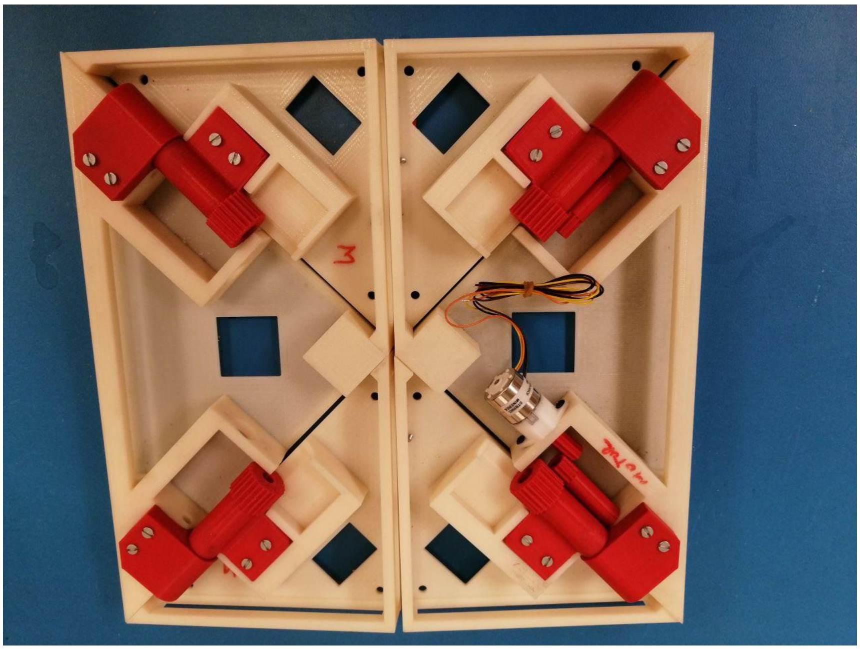

Figure 4.37: OSP test-bed assembly

$\sigma_{fs}\,[MPa]$	52	$T\,[Nmm]$	362.86	λ	10	$r_{tree}\,[mm]$	2
$\beta\,[\text{deg}]$	0	$\theta\,[\text{deg}]$	20	$M_{max1}\,[kg]$	5	$M_{max2}\,[kg]$	2.5
$L_1\,[mm]$	190	$L_2\,[mm]$	134.35	$h_2\,[mm]$	95	$a\,[mm]$	31.66
$C_r\,[Nmm]$	776.63	τ	2.14	z_1	10	y_{lewis}	4.98
m_n	0.89	$b\,[mm]$	8.85	$d_{p1}\,[mm]$	8.85	$d_{b1}\,[mm]$	8.32
$d_{a1}\,[mm]$	9.74	$d_f\,[mm]$	7.75	z_2	11	$d_{p2}\,[mm]$	9.74
$d_{b2}\,[mm]$	9.15	$d_{a2}\,[mm]$	10.63	d_{f2}	8.63	$C_2\,[Nmm]$	375.37
z_3	23	$d_{p3}\,[mm]$	20.37	$d_{b3}\,[mm]$	19.14	$d_{a3}\,[mm]$	21.25
$d_{f3}\,[mm]$	19.26	τ_2	1.1	τ_3	2.09	$C_3\,[Nmm]$	834.58

Table 4.4: OSP Proposals Properties

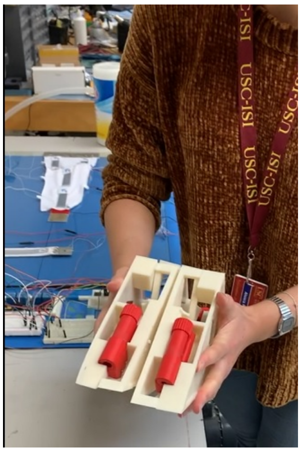

Figure 4.38: Manual test (Folded configuration)

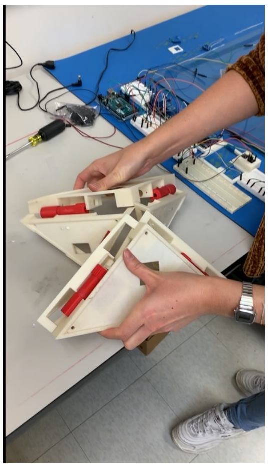

Figure 4.39: Manual Test

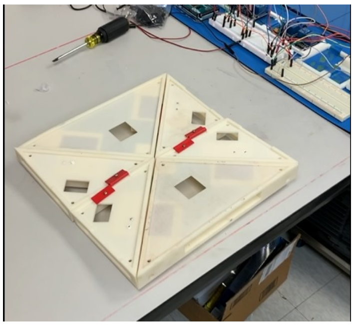

Figure 4.40: Manual Test (Deployed configuration)

Conclusions

This thesis is the result of six months worth of work at the USC in the SERC. It started with the LEAPFROG Generation-II structural design and continued with the RAMSEs preliminary design and its solar panel test-bed realization. The latter should be tested with its electronics, but due to Covid-19 only a manual test was performed which however showed that the panel can be deployed and folded without interference. Therefore, the next step of the work should be the OSP hardware test with its solar cells integrated. The mechanical movement test should be done with the solar cells surface oriented upwards, like the manual test. Moreover, a suitable grabbing interface for SINGO jaws has to be modelled when its CAD is available.

The RAMSEs preliminary design shows it is capable of reaching all the tool locations and its workspace is vast enough to reach the soil and manage all the tools, as well as to take the solar panel and deploy it on top of the LEAPFROG platform with half of its total length. Many improvements on the code can be done:

- adding the translational joint DOF for the end-effector
- performing a better orientation of the end-effector within the manipulation time, instead of using a simple; interpolation between the four waypoints orientation angles;
- link length is settled here a priori, but an optimal length study for finding the smallest one which has enough workspace to manipulate all the tools could be achieved.

Moreover, links should be correctly designed, considering results from this research. Here they are treated just with full trusses for studying their inertia contribution and fulfilling requirements.

Appendix A

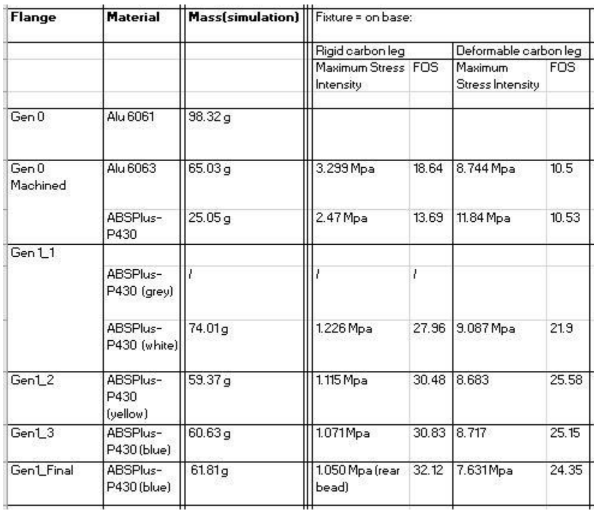

Flange	Material	Mass(simulation)	Fixture = on base:			
			Rigid carbon leg		Deformable carbon leg	
			Maximum Stress Intensity	FOS	Maximum Stress Intensity	FOS
Gen 0	Alu 6061	98.32 g				
Gen 0 Machined	Alu 6063	65.03 g	3.299 Mpa	18.64	8.744 Mpa	10.5
	ABSPlus-P430	25.05 g	2.47 Mpa	13.69	11.84 Mpa	10.53
Gen 1_1						
	ABSPlus-P430 (grey)	/	/	/		
	ABSPlus-P430 (white)	74.01 g	1.226 Mpa	27.96	9.087 Mpa	21.9
Gen1_2	ABSPlus-P430 (yellow)	59.37 g	1.115 Mpa	30.48	8.683	25.58
Gen1_3	ABSPlus-P430 (blue)	60.63 g	1.071 Mpa	30.83	8.717	25.15
Gen1_Final	ABSPlus-P430 (blue)	61.81 g	1.050 Mpa (rear bead)	32.12	7.631 Mpa	24.35

Figure A.1: Generation-1 Flanges Static tests

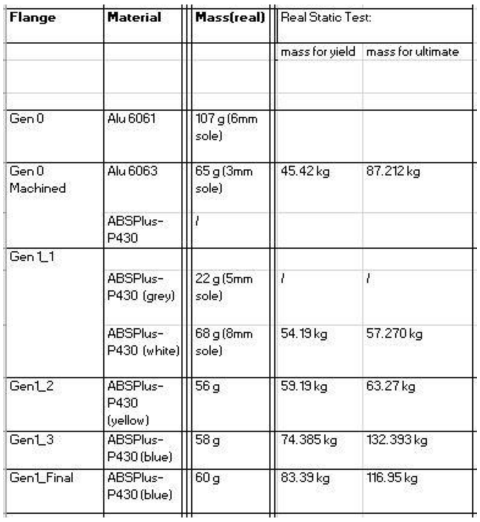

Flange	Material	Mass(real)	Real Static Test:	
			mass for yield	mass for ultimate
Gen 0	Alu 6061	107 g (6mm sole)		
Gen 0 Machined	Alu 6063	65 g (3mm sole)	45.42 kg	87.212 kg
	ABSPlus-P430	/		
Gen 1_1				
	ABSPlus-P430 (grey)	22 g (5mm sole)	/	/
	ABSPlus-P430 (white)	68 g (8mm sole)	54.19 kg	57.270 kg
Gen1_2	ABSPlus-P430 (yellow)	56 g	59.19 kg	63.27 kg
Gen1_3	ABSPlus-P430 (blue)	58 g	74.385 kg	132.393 kg
Gen1_Final	ABSPlus-P430 (blue)	60 g	83.39 kg	116.95 kg

Figure A.2: Generation-1 Flanges real tests

JetCat P-200

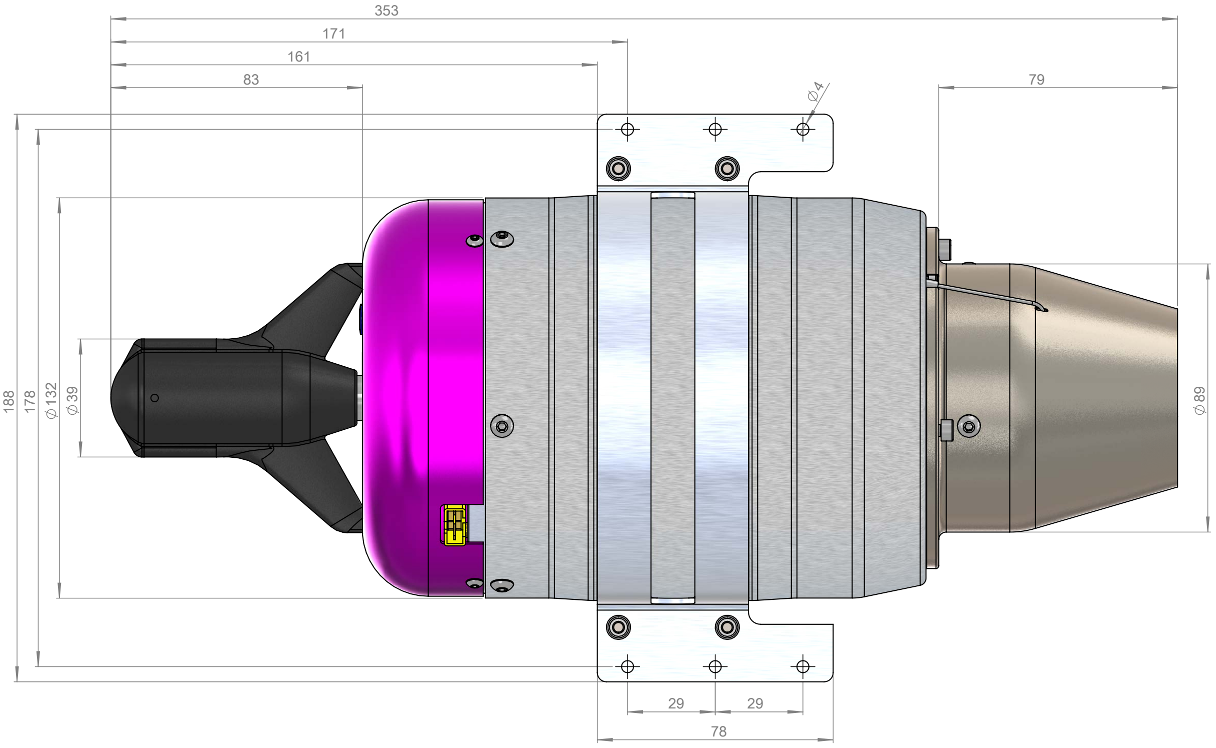

JetCat P-300

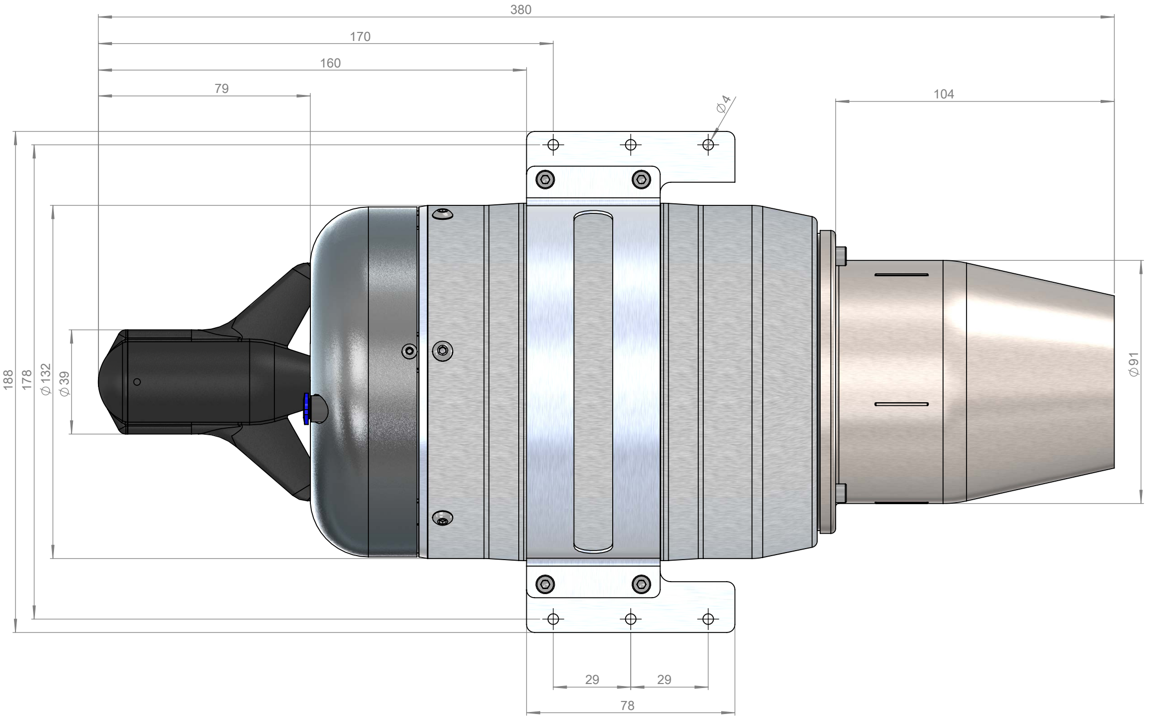

Standard PG Step Motors

PG20L-D20-HHC0

Model Specifications

Model:	PG20L-D20-HHC0
Step Angle:	0.198 °
Drive Voltage:	DC 10.0 V
Shaft Length:	10mm
Wire Length:	300mm fly leads (no connector)
Wire Holder:	90 deg. Left
Gear Ratio:	1/91
Electrical:	10V, 350mA
	Bipolar Constant Current
	10 ohms, MS70A

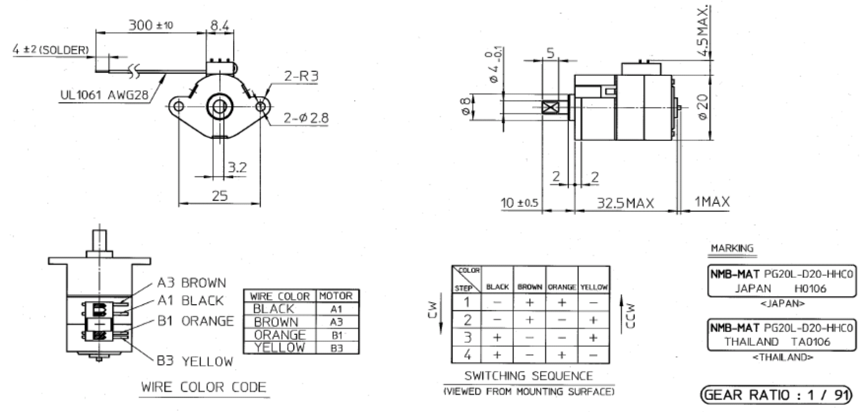

WIRE COLOR	MOTOR
BLACK	A1
BROWN	A3
ORANGE	B1
YELLOW	B3

STEP \ COLOR	BLACK	BROWN	ORANGE	YELLOW
1	−	+	+	−
2	−	+	−	+
3	+	−	−	+
4	+	−	+	−

PG20L-D20-HHC0

DYNAMIC TORQUE CHARACTERISTICS (No. 63550)

(ALL VALUES ARE GAINED BY MEASUREMENT AND NOT SPECIFICATIONS VALUES)

Model : PG20L-D20-HHC0
Drive Mode : BIPOLAR CHOPPER
Drive Voltage : 10.0 V
Method : 2-2P
Drive IC : UDN2916B-V
Surge/Current : / 350 mA / Phase (Peak)
Coil Resistance : 10.0 Ω
Magnet Material : MS70A
Stator Material : SUY/SPC(Ni)
Note : GEAR RATIO 1/91

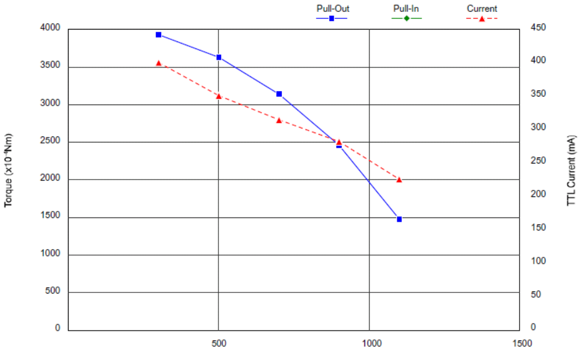

*pps = Hz

Frequency (pps)	300	500	700	900	1100
■ Pull-Out $(x10^{-4}Nm)$	3922.8	3628.6	3138.2	2451.8	1471.0
◆ Pull-In $(x10^{-4}Nm)$					
▲ Current (mA)	400	351	314	282	226

Figure A.3: Generation-1 Drop test bench

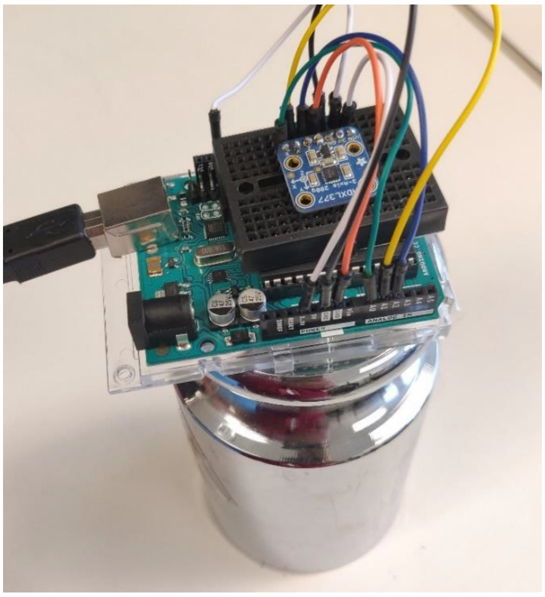

Figure A.4: Accelerometer connected to an ARDUINO UNO fixed on a weight of 5 kg

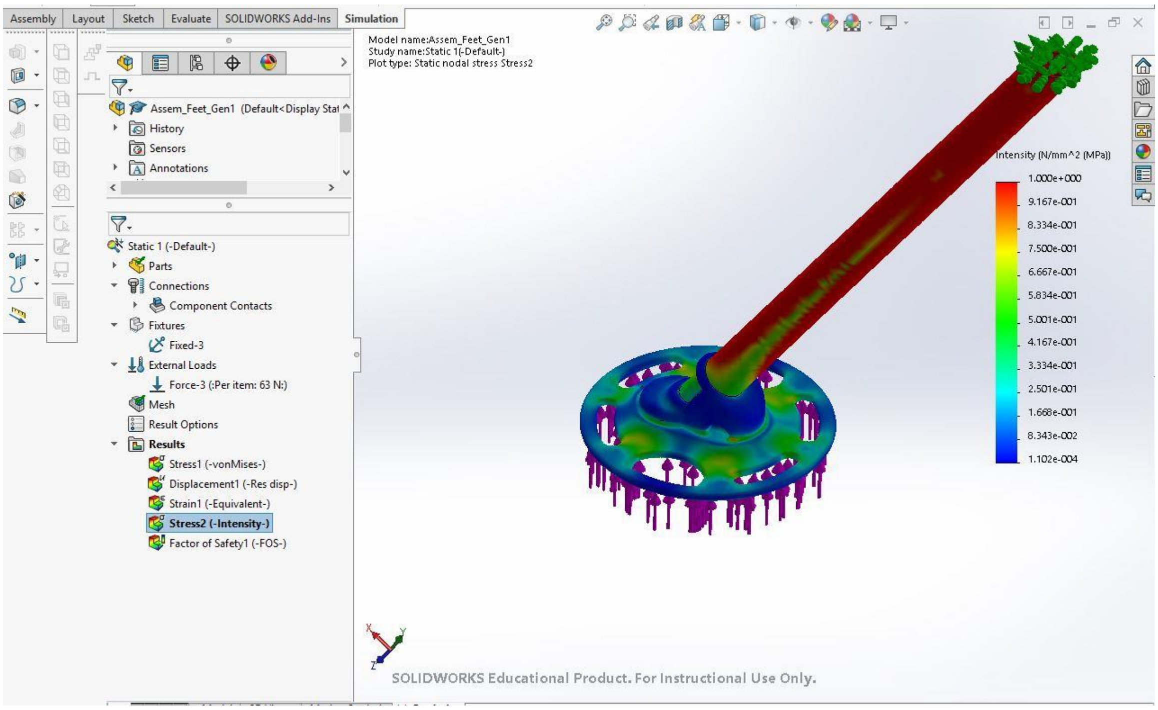

Model name:Assem_Feet_Gen1
Study name:Static 1(-Default-)
Plot type: Static nodal stress Stress2

Figure A.5: Generation-1 Leg static simulation of a $3ft$ free fall

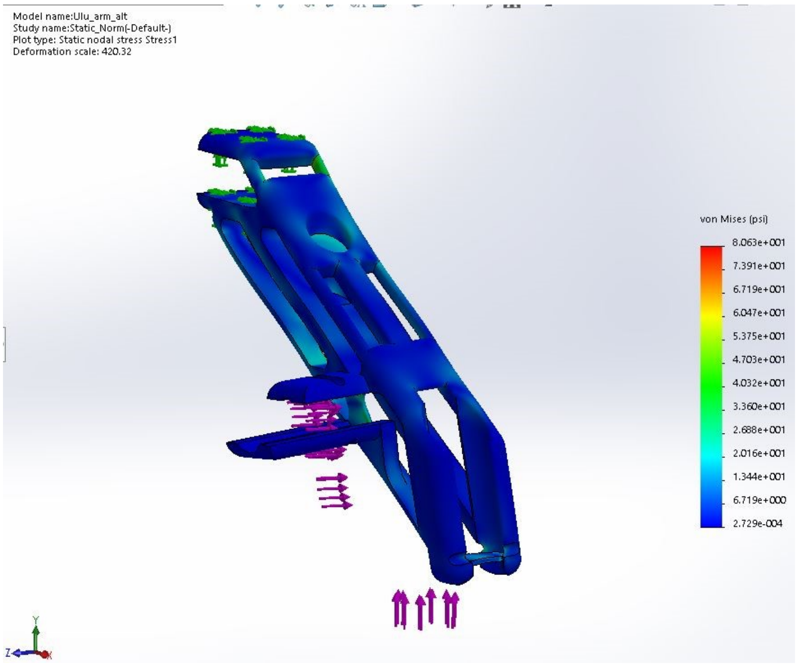

Figure A.6: Generation-1 Arm Von-Mises Stresses

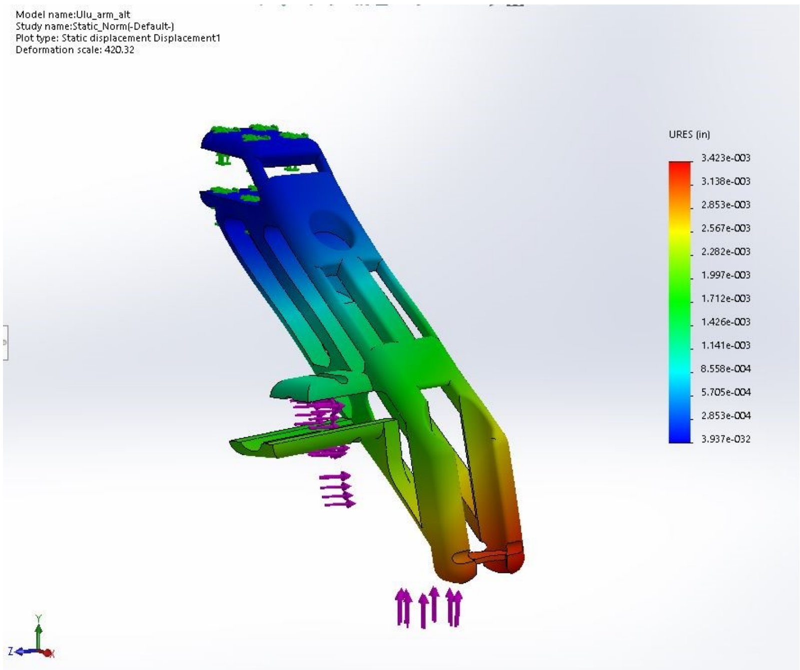

Figure A.7: Generation-1 Arm Displacements

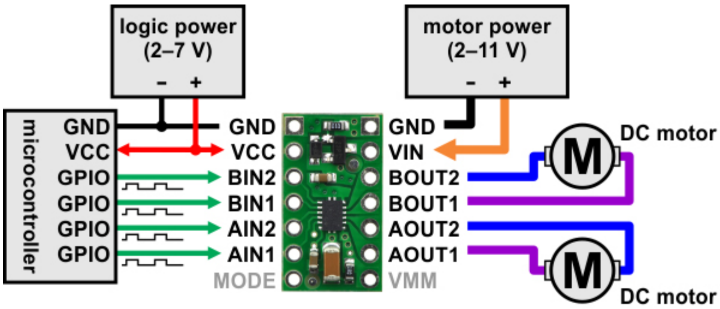

Figure A.8: OSP Test-bed motor driver

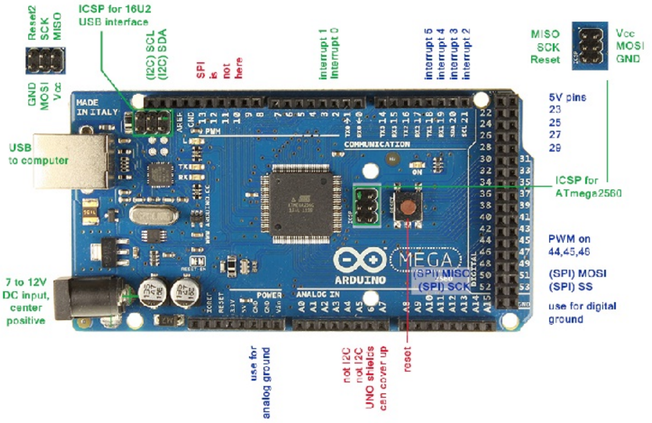

Figure A.9: OSP Test-bed motor driver

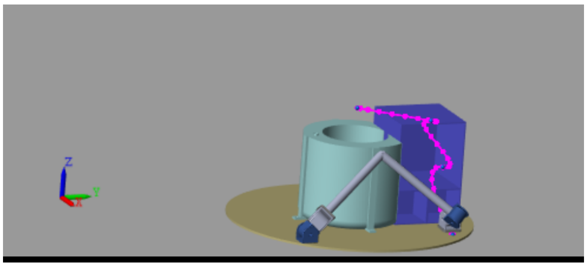

Figure A.10: The RAMSEs trajectory following simulation when he has to conjunct with the opposite part

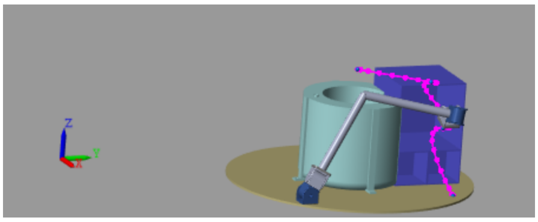

Figure A.11: The RAMSEs trajectory following simulation when he has to conjunct with the opposite part

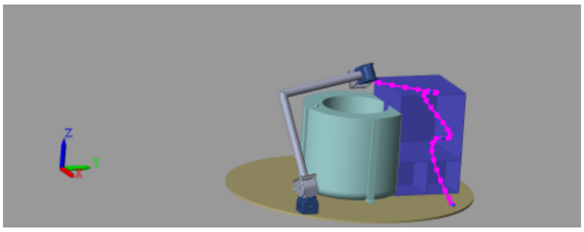

Figure A.12: The RAMSEs trajectory following simulation when he has to conjunct with the opposite part

Bibliography

[1] NASA. Nasa space science data coordinated archive. `https://nssdc.gsfc.nasa.gov/nmc/spacecraft/display.action?id=1959-014A`, june 2020.

[2] NASA. Nasa space science data coordinated archive. `https://nssdc.gsfc.nasa.gov/nmc/spacecraft/display.action?id=1966-045A`, june 2020.

[3] NASA. Nasa space science data coordinated archive. `https://nssdc.gsfc.nasa.gov/nmc/spacecraft/display.action?id=1966-116A`, june 2020.

[4] D. Barnhart, K. Bryant, C. Knight, J. Christmas, C. Coombs Phillips Laboratory, Edwards, D. Scott, and D. Hertzberg, editors. *IAA-95-IAA.11.1.04 Lunar Applications For Payload Delivery & Surface Analysis Using MicroSpacecraft*, volume 46 of *95*. 46th International Astronautical Congress, IAA-95-IAA.11.1.04, 10 1995.

[5] ASI. Smart-1. `https://www.asi.it/esplorazione/sistema-solare/smart-1/`, jun 2020.

[6] Windynation. Actuators user manual. `https://www.windynation.com/cm/Actuator%20Manual_R3.pdf`.

[7] Dae-Young Lee, Sa-Reum Kim, Ji-Suk Kim, Jae-Jun Park, and Kyu-Jin Cho. Origami wheel transformer: A variable-diameter wheel drive robot using an origami structure. *Soft Robotics*, 4, 05 2017.

[8] C. H. Belke and J. Paik. Mori: A modular origami robot. *IEEE/ASME Transactions on Mechatronics*, 22(5):2153–2164, 2017.

[9] R. J. Parks. Surveyor-I Mission Report. Part-I: Mission Description and Performance. Technical Report NASA-CR-77795, JPL-TR-32-1023, Jet Propulsion Lab., California Inst. of Tech., Pasadena, CA, United States, `https://ntrs.nasa.gov/search.jsp?R=19660026658`, 8 1966.

[10] Leonard D. Jaffe. Lunar surface exploration by surveyor spacecraft: Introduction. *Journal of Geophysical Research (1896-1977)*, 72(2):773–778, 1967.

[11] Cherkasov I. I., A. L. Kemurdzhian, L.l. Mikhailov, V. Mikheev, A. A. Morozov, A. A. Musatov, I. A. Savenko, M. I. Smorodinov, and V. V. Shvarev. Determination of the density and mechanical strength of the surface layer of the lunar crust at the landing site of luna 13 automatic lunar landing station, 7 1967.

[12] Launius, Roger D., Hunley, and J. D. An annotated bibliography of the Apollo program. Technical report, NASA-TM-109852, NAS 1.15:109852, `https://ntrs.nasa.gov/archive/nasa/casi.ntrs.nasa.gov/19940030162.pdf`, 7 1994.

[13] S. P. Weiss. Apollo experience report: Lunar module structural subsystem. Technical Report 73N18901, NASA Johnson Space Center; Houston, TX, United States, `https://ntrs.nasa.gov/archive/nasa/casi.ntrs.nasa.gov/19730010174.pdf`, 3 1973.

[14] P. D. Smith. Apollo experience report:spacecraft structure subsystem. Technical Report 74N34339, NASA Johnson Space Center; Houston, TX, United States, `https://ntrs.nasa.gov/archive/nasa/casi.ntrs.nasa.gov/19740026226.pdf`, 10 1974.

[15] Fisher A. E. Hammock W. R., Jr. Currie E. C. Apollo experience report: Descent propulsion system. Technical Report 73N19877, NASA Johnson Space Center; Houston, TX, United States, `https://ntrs.nasa.gov/archive/nasa/casi.ntrs.nasa.gov/19730011150.pdf`, 3 1973.

[16] Hecht, Sarbello, Fauer, Hebel, Dowse, Rabinowitz, Stonehouse, Beuregard, and Fleisig. *Apollo 11 Eagle Grumman LM-5 Construction Log*. Grumman, 1 edition, October 1968. Handwritten Construction and Testing Log Book.

[17] Davidson L. J. Dietz R. H., Rhoades D. E. Apollo experience report: Lunar module communications system. Technical Report 72N30905, NASA Johnson Space Center; Houston, TX, United States, `https://ntrs.nasa.gov/archive/nasa/casi.ntrs.nasa.gov/19720023255.pdf`, 9 1972.

[18] Weiss S. P. Pigg O. E. Apollo experience report: Spacecraft structural windows. Technical Report 73N31770, NASA Johnson Space Center; Houston, TX, United States, `https://ntrs.nasa.gov/archive/nasa/casi.ntrs.nasa.gov/19730023038.pdf`, 9 1973.

[19] Philip A. Helmke and Larry A. Haskin. Rare earths and other trace elements in luna 16 soil. *Earth and Planetary Science Letters*, 13(2):441 – 443, 1972.

[20] A. P. Vinogradov. Preliminary data on lunar surface material returned by Luna 16 automatic station. Technical Report 75N11815, Kanner (Leo) Associates; Redwood City, CA, United States, 10 1974.

[21] Simon Kassel. Lunokhod-1 soviet lunar surface vehicle. Technical report, RAND CORP SANTA MONICA CA, 1971.

[22] Stewart Nozette, P Rustan, LP Pleasance, JF Kordas, IT Lewis, HS Park, RE Priest, DM Horan, P Regeon, CL Lichtenberg, et al. The clementine mission to the moon: Scientific overview. *Science*, 266(5192):1835–1839, 1994.

[23] GD Racca, A Marini, L Stagnaro, J Van Dooren, L Di Napoli, BH Foing, R Lumb, J Volp, J Brinkmann, R Grünagel, et al. Smart-1 mission description and development status. *Planetary and space science*, 50(14-15):1323–1337, 2002.

[24] Y Ashok Kumar. The moon impact probe on chandrayaan-1. *Current Science (00113891)*, 96(4), 2009.

[25] Wing-Huen Ip, Jun Yan, Chun-Lai Li, and Zi-Yuan Ouyang. Preface: The Chang'e-3 lander and rover mission to the moon. *Research in Astronomy and Astrophysics*, 14(12):1511–1513, dec 2014.

[26] J. N. Goswami and M. Annadurai. Chandrayaan-2 Mission. In *Lunar and Planetary Science Conference*, Lunar and Planetary Science Conference, page 2042, March 2011.

[27] NASA. Artemis. `https://www.nasa.gov/specials/artemis/`, nov 2019.

[28] ESA. Exploration of the moon. `https://exploration.esa.int/web/moon/-/59102-about-prospect`, sep 2019.

[29] Blue Origin. Blue moon lander. `https://www.blueorigin.com/blue-moon`, nov 2019.

[30] BOEING. Boeing in space. `https://www.boeing.com/space/`, nov 2019.

[31] ISRO. Chandrayaan2. `https://www.isro.gov.in/chandrayaan2-home-0`, nov 2019.

[32] Astrobotic. Peregrine lander. `https://www.astrobotic.com/`, nov 2019.

[33] Nicholas Turner, Bill Goodwine, and Mihir Sen. A review of origami applications in mechanical engineering. *Proceedings of the Institution of Mechanical Engineers, Part C: Journal of Mechanical Engineering Science*, 230(14):2345–2362, 2016.

[34] NASA. Star shade. `https://exoplanets.nasa.gov/resources/1015/flower-power-nasa-reveals-spring-starshade-animation/`, nov 2019.

[35] NASA. Raincube. `https://www.jpl.nasa.gov/news/news.php?feature=6672`, nov 2019.

[36] NASA. Puffer. `https://www.jpl.nasa.gov/news/news.php?feature=6782`, nov 2019.

[37] NASA. Solar power, origami-style. `https://www.nasa.gov/jpl/news/origami-style-solar-power-20140814`, nov 2019.

[38] Morgan L. Hendry, Kristina Rojdev, Jason Cheng, Omer Faghfoor, Alvin Garcia, Paul Giuliano, Lucy Hoag, Cassandra Raskin, Michael Rudolph, and Omair Rahman, editors. *LEAPFROG: Lunar Entry and Approach Platform For Research On Ground*, 2764, DOI:10.2514/6.2007-2764, February 2007. AIAA, `http://arc.aiaa.org`.

[39] Benoît Meyer. Flight structure development for lunar lander simulator. Master's thesis, French Air Force Academy Engineering Degree, June 2019.

[40] NASA. Ntrs - nasa technical reports server llrv. `https://ntrs.nasa.gov/api/citations/19660010420/downloads/19660010420.pdf`, june 2020.

[41] Barnhart D., editor. *Scientific Mission Augmentation with KKV Technology*, 6. Philips Lab, Edwards A.F.B., February 1996.

[42] JetCat. JetCat P-200 Technical Specifications. `https://www.jetcat.de/jetcat/Bedienungsanleitung/Strahlturbinen_DE_JetCat_RX_%20120218.pdf`, june 2020.

[43] David Bernacchia. Design of thrust vectoring attitude control system for lunar lander flying testbed. Master's thesis, ALMA MATER STUDIORUM UNIVERSITA' DI BOLOGNA, March 2020.

[44] B. Salemi, M. Moll, and W. Shen. Superbot: A deployable, multi-functional, and modular self-reconfigurable robotic system. In *2006 IEEE/RSJ International Conference on Intelligent Robots and Systems*, pages 3636–3641, 2006.

[45] Wei-min Shen, Behnam Salemi, and Mark Moll. Modular, multifunctional and reconfigurable superbot for space applications, 09 2006.

[46] W. Shen, R. Kovac, and M. Rubenstein. Singo: A single-end-operative and genderless connector for self-reconfiguration, self-assembly and self-healing. In *2009 IEEE International Conference on Robotics and Automation*, pages 4253–4258, 2009.

[47] Mordechai Ben-Ari, Francesco Mondada, Ben-Ari, and Mordechai. *Elements of Robotics*, volume 1 of *1*. Springer, `10.1007/978-3-319-62533-1`, 3 edition, 11 2017.

[48] Koryo MIURA. Method of packaging and deployment of large membranes in space. *The Institute of Space and Astronautical Science report*, 618:1–9, dec 1985.

[49] Kazuko Fuchi and Alejandro R. Diaz. Origami Design by Topology Optimization. *Journal of Mechanical Design*, 135(11), 09 2013. 111003.

[50] P. Wang-Iverson, R. Lang, and M. Yim. Rigid-foldable thick origami, in origami 5. In *Fifth International Meeting of Origami Science, Mathematics, and Education*, pages 253–264, 09 2011.

[51] Bryce Edmondson, Robert Lang, Michael Morgan, Spencer Magleby, and Larry Howell. Thick rigidly foldable structures realized by an offset panel technique, 01 2015.

[52] Yan Chen, Rui Peng, and Zhong You. Origami of thick panels. *Science*, 349(6246):396–400, 2015.

[53] Jason S. Ku and Erik D. Demaine. Folding Flat Crease Patterns With Thick Materials. *Journal of Mechanisms and Robotics*, 8(3), 03 2016. 031003.

[54] Nathan Pehrson, Spencer Magleby, Robert Lang, and Larry Howell. Introduction of monolithic origami with thick-sheet materials, 09 2016.

[55] Cheng Wang, Junlan Li, and Zhong You. A kirigami-inspired foldable model for thick panels, 09 2018.

[56] Byoungkwon An, Nadia Benbernou, Erik D. Demaine, and Daniela Rus. Planning to fold multiple objects from a single self-folding sheet. *Robotica*, 29(1):87–102, 2011.

[57] M. Yao, H. Cui, X. Xiao, C. H. Belke, and J. Paik. Towards peak torque minimization for modular self-folding robots. In *2018 IEEE/RSJ International Conference on Intelligent Robots and Systems (IROS)*, pages 7975–7982, 2018.

[58] Daniela Rus and Michael T Tolley. Design, fabrication and control of origami robots. *Nature Reviews Materials*, 3(6):101–112, 2018.

[59] Cagdas D Onal, Michael T Tolley, Robert J Wood, and Daniela Rus. Origami-inspired printed robots. *IEEE/ASME transactions on mechatronics*, 20(5):2214–2221, 2014.

[60] M. Yim, W. Shen, B. Salemi, D. Rus, M. Moll, H. Lipson, E. Klavins, and G. S. Chirikjian. Modular self-reconfigurable robot systems [grand challenges of robotics]. *IEEE Robotics Automation Magazine*, 14(1):43–52, 2007.

[61] Philip Carbone. Progettazione e modellazione parametrica di riduttori meccanici. Master's thesis, POLITECNICO DI TORINO, Corso di Laurea Magistrale in Ingegneria Aerospaziale, 7 2018.